LBNL Deliverable to the Tricarb Carbon Sequestration Partnership:

Final Report

on

Experimental and Numerical Modeling Activities for the Newark Basin

Lawrence Berkeley National Laboratory

Sumit Mukhopadhyay

Nicolas Spycher

Nick Pester

Giuseppe Saldi

John Beyer

Jim Houseworth

Kevin Knauss

September 4, 2014

EXECUTIVE SUMMARY

This report presents findings for hydrological and chemical characteristics and processes relevant to large-scale geologic CO_2 sequestration in the Newark Basin of southern New York and northern New Jersey. This work has been conducted in collaboration with the Tri-Carb Consortium for Carbon Sequestration—comprising Sandia Technologies, LLC; Conrad Geoscience; and Schlumberger Carbon Services.

Geologic CO_2 sequestration operations in the Newark Basin would involve injection of pressurized CO_2 (in a supercritical state) into one of the deep sandstone formations present in this basin. To help assessing the feasibility of such deep injection, laboratory experiments and numerical modeling analyses have been carried out to characterize the dissolution and reaction of CO_2 with formation brine and minerals, and resulting effects on injection rate, pressure, effective storage volume, and CO_2 migration within a sandstone formation at depth (~1,500 m) within the Newark Basin.

A sandstone horizon encountered in a deep exploratory borehole (Tandem Lot Well #1), tentatively identified as belonging to the Passaic Formation, was characterized to assess its potential for CO_2 storage. This included developing a base-case hydrological property set as well as ranges for some of the hydrological properties of this formation, and the development of numerical models to assess CO_2 migration and reaction within the targeted formation. Some of the data required for the hydrological and reactive transport modeling have been developed through laboratory analyses of core samples and shallow fluid samples recovered during the drilling of the deep exploratory well. Deep formation fluid samples were not found, and for this reason the composition of the deep brine had to be reconstructed by geochemical modeling, using shallow water chemistry data and other available information. CO_2-brine-rock interaction experiments conducted in the laboratory were also conducted to provide data on aqueous composition of the equilibrated CO_2-brine-rock system, and to investigate the effects of CO_2 dissolution on fluid-mineral reactions.

Mineral saturation indices computed using data from the CO_2-brine-rock experiments suggest that feldspars (plagioclase, albite-K-spar system) should be destabilized by the drop in pH associated with CO_2 dissolution in the formation water, favoring the formation of minerals such as kaolinite, muscovite, and paragonite. Such geochemical modeling using experimental results also helped assess the likely minerals controlling the release of major dissolved constituents, such as for example chlorite and anhydrite releasing Mg and Ca, respectively). The trend with time of trace metal concentrations measured in reacted solutions during the experiments also suggested the possible growth of secondary mineral (e.g., clay minerals).

The experimental and modeling analyses suggest that mineral precipitation and dissolution reactions (within the target formation) are not expected to lead to significant changes to the underground hydrologic system over time frames (~30 years) typically relevant for CO_2 injection operations. Hydrological modeling using a radially symmetric two-dimensional model shows that injection of 1 MMt/yr over 30 years results in a maximum pressure rise of 8 MPa for a base-case permeability of 50 mD. The CO_2 plume migration was modeled using a three-dimensional domain for both a horizontal and tilted formation, with the storage formation tilted by an angle of 8° with the horizontal. In the case of a

horizontal formation, CO_2 injected at a rate of 1 MMt/yr is predicted to migrate horizontally about 2,000 m (on either side of the injection well), with about 12% of the total injected CO_2 dissolving into the formation brine after 30 years of injection. Continuing the simulation for another 70 years without injection (i.e., after a total simulated time period of 100 years), the plume is predicted to migrate to about 3,000 m from the injection well, with the dissolution of about 17% of all injected CO_2 into the formation brine. In the case of a tilted formation, after 30 years of injection, the same CO_2 injection scenario yields a CO_2 plume extending to about 3000 m up-dip, and an amount of dissolved CO_2 similar to that predicted for the horizontal case. However, once CO_2 is no longer injected, the plume is predicted to continue migrating up-dip by buoyancy, to about 8,000 m from the injection well after 100 years, resulting in the dissolution of 64% of all the injected CO_2. A series of sensitivity simulations was also performed by changing the values of key input parameters. The objective of the sensitivity analysis was to bracket the range of plume migration distance, fraction of injected CO_2 dissolving into the aqueous phase, and buildup of pressure near the injection point.

The interactions between CO_2, brine, and formation minerals were simulated using geochemical and reactive transport models, to evaluate changes in formation water chemistry, mineral precipitation and dissolution reactions, and any potential resulting effects on formation permeability. The main rock minerals considered were quartz, plagioclase, and potassium feldspar, but several other minor minerals were included in the model, including Fe-chlorite and anhydrite. Reactive transport simulations were conducted using the same two-dimensional radially symmetric model as that developed for the hydrological simulations. A two-dimensional cross-sectional model oriented along the dip of the formation was also developed to investigate the effects of a sloping stratigraphy. These models predict that the pH within the two-phase CO_2-brine plume drops to about 5, and remains at this level during the simulated 30-year injection peroiod. The carbonic acid from the dissolution of CO_2 into the formation brine is predicted to dissolve primarily plagioclase (resulting in the precipitation of chalcedony and dawsonite), and of Fe-chlorite (resulting in the precipitation of ankerite and kaolinite). The overall amount of mineral reaction (including dissolution and precipitation) was found to be relatively small, leading to an overall decrease in (absolute) porosity of ~0.3%.

Given their importance in controlling the plume characteristics and fate of the injected CO_2, it is recommended that more reliable site-specific data with regards to formation permeability (including its heterogeneity), relative permeability, and capillary characteristic be collected and incorporated in any future model revisions. The modeling results also indicate that the effects of formation dip on plume migration and interactions with the aquifer brine are important to include in any evaluations of long-term (> 50 years) CO_2 sequestration. Further hydrological model improvements that could be considered for future analyses are: (1) inclusion of the thermal effects, (2) accounting for capillary hysteresis, (3) characterizing and incorporating permeability heterogeneity, including fractures, and (4) accounting for the effects of salt precipitation on permeability.

On the geochemistry side, one of the most uncertain aspects of this study is the lack of measured deep-brine compositions, as well as uncertainties in mineral-reaction rates, most particularly for precipitating secondary phases. Should any further drilling be considered, the acquisition of deep brine samples within the Newark Basin would provide important additional constraints on reactive transport modeling simulations. Additional laboratory experiments tailored to better understand the precipitation mechanisms

and rates of secondary phases could also significantly constrain modeling results. Further reactive transport modeling efforts that could be considered include: (1) analyses of model sensitivity to initial brine compositions and mineral reaction rates, focusing on short-term (~30 year) near-well processes affecting injection, (2) assessing interactions with cap-rock minerals, (3) assessing CO_2 mineralization rates over longer time periods (centuries and longer).

Table of Contents

List of Tables

List of Figures

List of Acronyms

2D	Two-dimensional
3D	Three-dimensional
DSA	Deep Saline Aquifer
E-W	East-West
GCS	Geologic Carbon Storage
IFT	Interfacial Tension
IPCC	Intergovernmental Panel on Climate Change
LBNL	Lawrence Berkeley National Laboratory
MRCSP	Midwest Regional Carbon Sequestration Partnership
MSL	Mean Sea Level
MMt	Million Metric Tons
NBCP	Newark Basin Coring Project
NCS	Net Confining Stress
NJGS	New Jersey Geological Survey
NYSDEC	New York State Department of Conservation
NYSTA	New York State Thruway Authority
RCDOH	Rockland County Department of Health
TD	Total Depth
USDW	Underground Sources of Drinking Water
USEPA	United States Environmental Protection Agency
XRD	X-Ray Diffraction

1. INTRODUCTION

The connection that has been identified between atmospheric emissions of CO_2 and global climate change has led to intensive investigations into ways to mitigate the rate of CO_2 buildup in the atmosphere. One mitigation strategy is geologic carbon sequestration (GCS), a process by which CO_2 is captured from anthropogenic sources and injected into subsurface geologic formations to prevent CO_2 emissions from entering the atmosphere.

In GCS, CO_2 is injected into storage formations through wells that are sufficiently deep (generally 800 m or more) such that the CO_2 is in a supercritical state. Injection as a supercritical fluid is preferred over a gas-phase injection because the increased mass density of supercritical CO_2 means that the required storage volume is reduced. Supercritical CO_2 is much denser than air but still less dense than formation brine and has a lower viscosity than brine. The buoyancy of the CO_2 relative to brine leads to a tendency for the CO_2 to override the brine and move along the caprock that seals the upper boundary of the aquifer.

CO_2 can be trapped in the subsurface through several mechanisms. The most rapid trapping mechanism is caused by structural and stratigraphic trapping of otherwise mobile CO_2 by heterogeneities in the geologic system. Another physical trapping mechanism that operates over intermediate time scales is the trapping of CO_2 by capillary forces when brine displaces CO_2. This displacement process leads to the breakup of large regions of continuous and mobile CO_2 into smaller, discontinuous, and immobile residual clusters or ganglia. The mutual solubility of brine and CO_2 can result in the trapping of CO_2 as a dissolved phase in the aquifer brine, which also occurs over intermediate time scales. Over even longer time scales, CO_2 can be trapped by geochemical processes through the mineralization of the CO_2 in the form of carbonate minerals.

The injection of CO_2 also perturbs the existing geochemical environment of the saline aquifer. Changes occur in the brine geochemistry that can lead to complex mineral precipitation and dissolution reactions. These geochemical effects can feed back into the hydrologic behavior of the CO_2 through changes in porosity, permeability, and capillary properties of the storage formation and sealing caprock.

This report summarizes a broad research effort over the last three years concerning the potential for CO_2 sequestration into deep saline aquifers (DSA) of southern New York and northern New Jersey. Numerous industrial sources of CO_2 are located in the area, so the characterization of a large nearby geologic sink is expected to accelerate the development and implementation of carbon capture and GCS. The project was initiated in response to DOE solicitation FOA-0000033. The Tri-Carb Consortium for Carbon Sequestration—comprising Sandia Technologies, LLC; Conrad Geoscience; and Schlumberger Carbon Services—was formed to address the technical evaluation and research-investigation of the subsurface geology in the Newark Basin in the states of New York and New Jersey.

For this study, Lawrence Berkeley National Laboratory (LBNL) collaborated with the Tri-Carb Consortium and research team by serving on the Project Advisory Committee and undertaking research on various aspects of the geologic storage assessment. The report focuses on the behavior of CO_2 injection, migration, trapping, and geochemical interactions that may be expected from the sequestration of CO_2 in deep saline aquifers of the Newark Basin.

1.1 Objectives

LBNL geochemists have conducted experimental and numerical model simulations of the interactions of CO_2 with reservoir rocks and brine of the Newark Basin collected from a new deep exploration well (New York State Thruway Authority or NYSTA Tandem Lot Well #1) to assess chemical interactions associated with the transport of CO_2 in the deep subsurface at this location. This work contributes to a preliminary assessment of the suitability of the Newark Basin for CO_2 storage. To this end, experimental and modeling studies were designed to examine the interaction of supercritical CO_2 with reservoir rocks and fluids. The goals of this study were to:

- Assess the evolution of the injected CO_2 plume, including its shape and migration distance
- Assess the evolution of likely buildup in pressure resulting from planned injecion
- Assess the fate of the injected CO_2, including its partitioning between different phases
- Assess the rate of dissolution of CO_2 in brine in the formation
- Assess the rate of mineralization in the formation and its effect on injection rate and storage

Experiments were carried out in the lab by reacting formation core samples with supercritical CO_2 at site-specific conditions of temperature and pressure, and by performing simulations to determine the rate of dissolution of CO_2 into brine and effects on vertical mixing, migration, and storage in the host rock.

1.2 Newark Basin Stratigraphy and CO_2 storage potential

The New Jersey Geological Survey (NJGS), in conjunction with Rutgers University, performed a preliminary characterization of geological sequestration potential in the state of New Jersey and adjacent offshore region including the continental shelf and slope in support of the Midwest Regional Carbon Sequestration Partnership, MRCSP (NJGS, 2011). Because the geology of New Jersey and its offshore region is diverse, encompassing the Coastal Plain, offshore continental shelf and continental slope, Piedmont (Newark Basin), and Highlands, Valley and Ridge, each of these geologic settings was evaluated in terms of its suitability for GCS.

Based on its preliminary characterization, NJGS concluded that the main geologic sequestration options in New Jersey are the numerous deep sandstone formations found in the New Jersey Coastal Plain and adjacent continental shelf and slope. These formations are thick, with burial depths >800 m, which is a necessary criterion for storage of CO_2 at pressure and temperature conditions conducive to a supercritical state. Additionally, these formations are capped by thick low-permeability confining beds required to isolate CO_2 in the sequestration target formation.

According to NJGS (NJGS, 2011), the Potomac Formation (Late Cretaceous) of the Atlantic Coastal Plain present the most likely target for CO_2 sequestration in this area. This unit is very sandy but discontinuous, is hydrologically isolated from shallow fresh water aquifers, and has the capability to store and absorb significant volumes of CO_2. The range of total CO_2 storage in the Potomac sand units was estimated by NJGS to be 57 - 283 million metric tons (MMt).

The same NJGS characterization study (NJGS, 2011) identified the Stockton Formation (Upper Triassic), the basal sedimentary unit of the Newark Basin, as another potential target formation for long-term CO_2

sequestration. Even though hydrologic parameters and lateral continuity of target lithologies in the Stockton Formation are far from conclusive because of lack of deep borehole data, it exceeds 800 m depth in about 2/3 of the area of the basin, with a thickness varying from 150 to 1,400 m based on cross-sectional analysis. The Stockton Formation is also overlain by thick low-permeability rock (see below for more details), making it an attractive target for GCS. According to Olsen et al. (1996), the beginning of the rifting of Pangea during the Triassic and Early Jurassic resulted in the formation of an extensive series of rift basins along the contiguous boundaries of the North American, African, and Eurasian plates. In eastern North America, these rifts, filled with thousands of meters of continental sediments and igneous rocks, are termed the *Newark Supergroup.* Covering over 7,000 km^2, the Newark Basin is the largest of the exposed Newark Supergroup basins (Figure 1.1). It is about 190 km long and maximally 50 km wide. The basin is connected in the southwest to the Gettysburg Basin of Pennsylvania and Maryland by a narrow neck, and the latter is separated by a very small strip of basement from the Culpeper Basin of Maryland and Virginia. The basin provides a complete but relatively poorly exposed section spanning nearly the entire Late Triassic and part of the Early Jurassic (Cornet, 1977).

Even though the Stockton Formation makes up the basal formation over most of the Newark Basin, not much is known about how lithologies and porosities in the Stockton Formation vary in the subsurface throughout the basin (NJGS, 2011). What was known prior to drilling new well NYSTA Tandem Lot Well #1 came from two deep oil exploration wells in Pennsylvania, and two deep cores in New Jersey (Olsen et al., 1996), outcrop samples, and shallow core from near the outcrop area. The following description is generally excerpted from Olsen et al. (1996).

A National Science Foundation–funded project to continuously core the Triassic-Jurassic Newark rift basin of New York, New Jersey, and Pennsylvania was carried out during 1990–1993. The over 6,770 m of continuous core spanning 30 million years recovered by this drilling program, called the Newark Basin Coring Project (NBCP), provides the longest continuous record of a continental rift and lacustrine sequence available anywhere. The NBCP involved coring from seven sites, namely Princeton, Nursery, Titusville, Rutgers, Somerset, Weston, and Martinsville (Olsen et al., 1996). The Stockton Formation occurs in the Princeton # 1 core from 254.2 m to 1126.8 m (TD [total depth]) and the Nursery # 1 core from 968.7 m to 1008.6 m (TD). In these occurrences, most of the Stockton Formation consists of 5- to 10-m-thick fining-upward cycles of buff, white, and gray arkose or pebbly arkose, grading upward into brown heavily bioturbated mudstone. In general, small-scale sedimentary structures are difficult to see in the sandstones, presumably due to bioturbation. Carbonate nodules are abundant in many mudstones, and interclast conglomerates are abundant within the sandstones. Most of the thicker sandstone and pebbly sandstone sequences are gray or white, and are interbedded with minor amounts of gray mudstone.

In general, the Stockton Formation in the cores is lithologically very similar to the outcrops of the type section. The boundary between the upper Stockton and lower Lockatong Formations is at the base of the lowest prominent black or gray shale sequence in the lower part of the Wilburtha Member. Comparison of the Princeton # 1 core and the type section in outcrop suggests a correlation in which two different, but stratigraphically close, gray and black units mark the base of the Lockatong Formation, and thus the boundary between the two formations changes slightly laterally. The thickness of sedimentary cycles in the basal Lockatong Formation in its type area (as seen at Byram, New Jersey) is 177% of that in the correlative portion of the Princeton # 1 core. If the Stockton Formation in outcrop is similarly expanded

relative to that in the Princeton # 1 core, there would be a close match between the position of major sand and conglomerate-rich parts of the section. This proportional relationship between core and outcrop suggests that the members of the Stockton Formation identified by McLaughlin (1945) can be identified in the Princeton core. Overall, the Stockton Formation tends to fine upward, with the uppermost 102 m of Stockton Formation in the Princeton # 1 core being dominated by red mudstone, as is true for the outcrop sections.

A typical (generalized) stratigraphy of the Newark Basin is shown in Figure 1.1. The Stockton Formation is overlain by the Lockatong Formation, which has a thickness of approximately 1,000 m. The deep lake and mudflat shales of the Lockatong Formation provide the primary caprock seal. Further, the Passaic Formation, which is situated above the Lockatong Formation and can be as thick as 3,000 m with its Playa Lake and mudbank shales, can act as secondary caprock seal. According to NJGS (NJGS, 2011), the Stockton Formation has a widely variable depth and thickness. It is deepest and thickest beneath the Watchung Mountain locality in New Jersey, where formation depth may exceed 6,000 m below mean sea level (MSL) and formation thickness may exceed 1,350 m. Depths west of Flemington generally are less than 3,000 m below MSL, and most are less than 2,500 m. The Stockton Formation is also relatively shallow and thin in the Pennsylvania part of the basin compared to areas farther northeast. In addition, the Stockton Formation has a variable dip (~8-14°), with the dip in the southeastern parts of the basin in Pennsylvania being smaller than in areas farther northeast in New Jersey and New York. Finally, the NJGS estimated that the Stockton Formation provided a pore volume between 179 km^3 (assuming porosities of 5%) and 358 km^3 (assuming porosities of 10%) at depths of 800 m below the MSL. As expected, most (~78%) of this estimated pore volume is available in the eastern part of the Newark Basin.

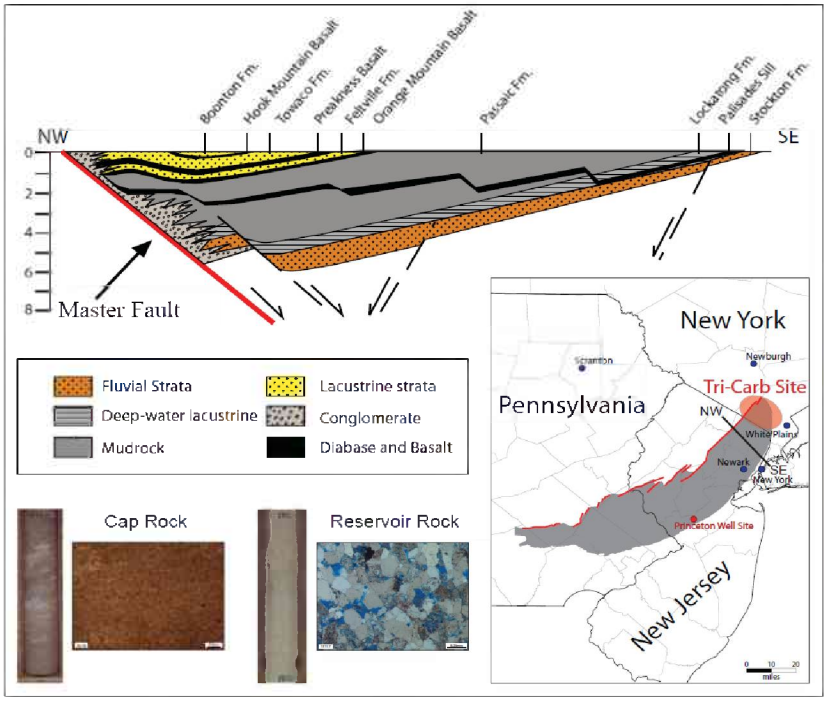

Figure 1.1. General stratigraphy of the Newark Basin and location of the Tri-Carb Site. Source: Unpublished figure, New York State Museum (*http://www.nysm.nysed.gov/nysgs/research/carbon/images/NewarkBasin.pdf*).

The new exploration well NYSTA Tandem Lot Well #1, drilled to a total depth of 6,870 ft (2,094 m) near the southeast edge of the basin (Figure 1.1), provided additional stratigraphic data at the well location and further characterization of the Stockton and overlying formations (cite reports from other groups working with us). One main difference with the stratigraphy observed at other locations in the Newark Basin is the shallower occurrence of all units near the edge of the basin and the presence of the Palisade Sill (a widespread igneous intrusion) near the contact between the Stockton and Lockatong formations (Figure 1.1). In fact, below the Palisade Ssill, the new exploratory well did not encounter sandstones with sufficient porosity to consider CO_2 injection. For this reason, experimental and numerical studies presented in this report rely on data collected for permeable sandstones collected above the Palisade Sill (at a depth of about 4,190 ft, or 1,277 m), possibly representative of the Passaic Formation instead of the Stockton Formation.

1.3 Report Organization

The feasibility of CO_2 injection into a deep sandstone formation in the Newark Basin is investigated following a four-prong approach: (1) development of a reliable hydrological model of the site including analysis of available site characterization data for developing a hydrological parameter set; (2) analysis of available geochemical data to reconstruct the deep brine composition; (3) laboratory experiments and geochemical modeling of CO_2-brine-rock reaction, using sandstone samples from the target storage formation; and (4) development of a reactive transport simulation framework by combining inputs from (1) and (2). Therefore, this report is organized into sections following the sequence described above, as summarized below.

Section 2 of this report focuses on hydrological model building. In this section, we analyze the available site characterization data and develop a base-case hydrological parameter set, which forms the basis for the flow-only and reactive transport simulations presented later in this report. The flow-only model described in Section 2 is used to predict the maximum plume migration distance, partitioning of the injected CO_2 between the compressed (CO_2-rich) "gas" and brine (or aqueous) phases, and evolution of pressure near the injection well. Extensive sensitivity simulations are also presented in this section to bracket the range of predicted values. The flow-only model of Section 2 is used as the starting point for reactive transport simulations presented in Section 6.

In Section 3, we present site-specific geochemical data relevant for (and used in) our laboratory experiments and reactive transport modeling investigations. This includes mineralogical data for the targeted sandstone formation, and analyses of fluids collected while drilling the NYSTA Tandem Lot Well #1. Because deep fluid samples were not recovered, we also present in Section 3 the rationale for estimating the composition of deep brines, and geochemical modeling analyses conducted to derive these deep fluid compositions.

The results of laboratory experiments reacting supercritical CO_2 with various brine chemistries and sandstone samples collected in exploration well NYSTA Tandem Lot Well #1 are presented in Section 4. Geochemical modeling analyses of these experiments are also presented in this section, to provide

insights on reactive processes at play, and to help guide further geochemical and reactive transport modeling work presented in Sections 5 and 6.

In Section 5, we report on the setup and results of reaction-path geochemical simulations that consider the chemical reactions between formation water, sediments, and CO_2, without considering transport. These simulations are conducted as a prelude to more sophisticated field-scale reactive transport simulations, with the goal of determining potential thermodynamically stable (secondary) minerals forming by the reaction of the target sandstone with brine at various brine/rock ratios in the presence of supercritical CO_2.

Finally, in Section 6, we describe reactive transport simulations of CO_2 injection into the target sandstone formation. These simulations consider multiphase fluid flow at field scales with hydrological inputs consistent with the model presented in Section 2, coupled to multicomponent reactive transport.

The findings from the present experimental and numerical study are summarized in Section 7, where we also make recommendations for possible further investigations to improve our confidence in model predictions.

2. MULTIPHASE FLOW MODELING FOR CO_2 INJECTION

In this section, we report on the development of, and results from, multiphase flow simulations aimed at assessing the migration of CO_2 upon injection into the Newark Basin. The simulations are carried out for a hypothetical but typical injection scenario (1 MMt/year for 30 years) into a geologic formation with physical and hydrological properties determined from the characterization of core samples recovered from exploration well NYSTA Tandem Lot Well #1. In the conceptual model presented in this section, the effect of CO_2 reaction with formation brine and minerals on fluid flow is not taken into account. These reactive effects were investigated experimentally, with results presented in Sections 3 and 4, then incorporated into full reactive transport simulations discussed in Section 6. As discussed in these later sections, the reactivity of CO_2 in the investigated system is expected to be low and have little effect on CO_2 injection and migration, at least under the conditions of temperature, pressure, formation mineralogy, and brine chemistry assumed for injection activities in the Newark Basin.

Understanding and accurately predicting the fate of the injected CO_2, both during injection and many decades after injection ceases, has become one of the key prerequisites of planning and successful implementation of GCS projects (Jiang, 2011). The concerns regarding the fate of the injected CO_2 often center around the questions of how far and how fast a large volume of CO_2 will migrate inside the storage formation, what will be the nature of its interaction with the resident fluid phase (e.g., brine), and whether it will ever be able to escape from its storage location and either cause harm to groundwater or escape to the atmosphere, negating the climate benefit (IPCC, 2005). While an effective monitoring, verification, and accounting framework (Chadwick et al., 2009; Plasysnski et al., 2011; Monea et al., 2013) may be able to provide answers regarding some of these concerns, reliable and directly observed information about CO_2 migration over extended spatial and temporal scales will continue to remain elusive and expensive. More specifically, such information will simply not be available before designing a GCS project, and, when available, can possibly assist only in validation but not in making predictions. It is in

this context that predictive fluid flow and reactive transport modeling has been performed for expected future CO_2 injection in the Newark Basin. Therefore, the objective of the multiphase fluid flow modeling presented in this section is to provide an estimate of the extent of the CO_2 plume migration after being injected into a deep sandstone formation (~1,500m depth) in the Newark Basin. Reactive transport modeling based on the same hydrological parameters and model domain as developed for multiphase fluid flow simulations is then applied (Section 6) to investigate the nature of geochemical reactions between the injected fluid and resident brine and the impact of these reactive transport processes on flow and transport of CO_2.

Generally speaking, considerable effort has been and continues to be invested in developing mathematical models for not only gaining insights into the processes controlling CO_2 migration, but also making reliable and accurate predictions about the fate of CO_2 at GCS sites such as the Newark Basin. While we will discuss the processes controlling CO_2 migration in detail later, it will suffice to state here that these models must account for multiple physicochemical processes involving interactions between the injected CO_2, the formation fluids (either brine or hydrocarbons), and the reservoir rocks over multiple spatial and temporal scales (Kang et al., 2010). Depending upon the nature of the fluids already residing in the formation, these processes may include (but are not necessarily limited to) fluid flow under pressure gradients created by the injection process; buoyancy-driven flow caused by density difference between the injected and formation fluids; diffusion, dispersion and fingering (arising from formation heterogeneities and mobility contrast between the fluids); capillarity (resulting from different wetting characteristics of the fluids concerned); dissolution into the formation fluid, mineralization, and adsorption of CO_2 (IPCC, 2005).

2.1 Physicochemical Processes Controlling CO_2 Migration

When supercritical CO_2 ($scCO_2$) is injected into a DSA, its flow (and also that of the resident brine) depends on, among other factors, the relative densities and viscosities of the two fluid phases, both of which depend on temperature and pressure (and hence depth) of the aquifer. According to Nordbotten et al. (2005), under typical storage conditions, the density ratio of $scCO_2$ and brine is likely to be in the range 0.22–0.75 ($scCO_2$ is the lighter fluid phase and hence the density ratio is less than one); however, the viscosity ratio of these two fluid phases is expected to be in the range 0.026–0.22. These differences in density and viscosity have important consequences for the fate of the injected CO_2. For example, the comparatively large density difference between CO_2 and formation brine creates strong buoyancy forces that drive CO_2 upwards from the point of injection. However, the rise of the buoyant plume is non-uniform, and is controlled by formation heterogeneity such that low-permeability layers within the formation decelerate the upward motion of the buoyant plume, and force it to move laterally. This is particularly true once the plume reaches a sealing caprock at the top of the storage formation, after which it cannot rise any further, and continues to spread laterally along the sealing boundary. Additionally, the large contrast in mobility between the injected $scCO_2$ and the resident brine, resulting from the significantly smaller viscosity of the former, causes it to move ahead of the brine phase, bypassing most of the pore space in its flow path, the degree of which depends on the heterogeneity and anisotropy in formation permeability.

As CO_2 migrates through the storage formation, some of it dissolves into the formation brine, after which

the dissolved CO_2 migrates along with regional groundwater flow. DSA are often characterized by low permeability and high salinity, and have extremely low groundwater flow velocities. As a result, migration rates of dissolved CO_2 are substantially lower than that of gas-phase (or supercritical-phase) CO_2. Furthermore, as CO_2 migrates through the DSA, some of it is retained in the pore space by capillary forces, with the potential to immobilize significant amounts of CO_2. Over time, much of the CO_2 retained by capillary forces dissolves in the formation water, and ceases to exist as a separate supercritical ("gas") phase.

Injection of large volumes of CO_2 is also likely to bring about substantial geomechanical changes in the storage formation. In fact, the area over which geomechanical changes may occur is likely to extend far beyond the area of actual pressure changes, which in turn extends far beyond the CO_2 plume (Rutqvist, 2012). Even a small pressure change and straining of the rock (resulting from injection and associated thermal effects) might result in small microseismic events because of rock heterogeneities, including fractures and local stress concentrations. If reservoir pressure becomes sufficiently high, more substantial, irreversible mechanical changes could occur, e.g., creating new fractures, straining the well assembly, or reactivating larger faults within the reservoir, in the caprock or overburden. This could possibly open new flow paths through otherwise low-permeability caprock or sealing formations and thereby enable enhanced, buoyancy-driven, upward migration of the injected CO_2 (Teatini et al., 2011; Rutqvist, 2012; Teatini et al., 2014). Moreover, reactivation of a fault could potentially result in a notable seismic event that, if felt, may raise concern in local communities. Note that these geomechanical processes associated with GCS were not addressed in this study and are not discussed further in this report.

In addition to geomechanical processes, geochemical processes (such as salt precipitation resulting from evaporation of water near the injection well) also can lead to significant formation overpressuring, reduction in permeability, and loss of injectivity during CO_2 injection in DSA. During the injection phase, large temperature gradients also exist between the injection well and the storage formation because the injected CO_2 is considerably cooler than the original formation temperature. This results in significant water-rock interactions involving carbonate minerals, as well as sulfate and evaporite minerals, because their reaction kinetics are fast and equilibrium is reached almost instantaneously (Gaus, 2010). Over longer time scales, dissolved CO_2 in brine and acidification of the brine will generate chemical interactions with the minerals of the reservoir rock. Understanding these longer-term water-rock interactions is important in predicting the capacity of the reservoir to permanently trap CO_2 in a mineral, which is termed mineral trapping. Water-rock interactions can also alter the properties of the sealing caprocks, opening up the possibility of enhanced leakage and contamination of nearby underground sources of drinking water (USDW). Injection of large volumes of CO_2 in DSA also causes large-scale migration of brine, which may contaminate aquifers. An excellent review of the water-rock interactions during CO_2 injection and afterwards can be found in Gaus (2010). We discuss some of these geochemical processes in more detail, in the context of reactive transport modeling in the Newark Basin, later in the report (see Sections 3 through 6).

Based on the above discussion, it can be seen that spread of CO_2 in storage formations is controlled by two dominant trapping processes, namely physical and chemical trapping (IPCC, 2005; Bachu, 2008). Physical trapping includes structural and stratigraphic trapping wherein the injected $scCO_2$ is stored in closed, physically bound traps or structures, often under low-permeability caprocks. Physical trapping

also refers to residual-trapping wherein the DSA may not have a closed trap but the injected CO_2 is retained by capillary forces. In chemical trapping, CO_2 is trapped through dissolution into brine (i.e., solubility trapping), adsorption on to rock matrix (i.e., adsorption trapping), and/or reaction with minerals in the rock matrix (mineralization).

The trapping mechanisms mentioned above occur over distinctly different time scales. Initially, injected CO_2 migrates away from the point of injection under the influence of either the applied pressure gradient or the forces of buoyancy. During this time period, when active injection happens and which generally lasts a few decades, spread of CO_2 is mainly diminished by structural and stratigraphic trapping. This is followed by residual and solubility trapping in the intermediate time scales spanning from 100 to 1,000 years (IPCC, 2005; Zhang and Song, 2014). Mineral trapping, on the other hand, is a much slower process and continues to occur long after injection ceases, and will likely extend to hundreds of thousands of years. Because of these differences in time scales, storage by stratigraphic and structural trapping has been often termed as primary trapping, whereas that by solubility and mineral trapping is called secondary trapping. While secondary trapping does not necessarily increase the storage capacity, they are important for increasing the security of storage.

From the foregoing discussion, it is clear that modeling of CO_2 migration is a challenging task involving multiphase flow and transport in porous media along with slow chemical reactions. Modeling of long-term geological storage of CO_2 needs to address all the relevant physical and chemical processes that may take place. In addition, CO_2 properties as well as the properties of the geological media, including their spatial variability, need to be taken into account in the model being developed.

2.2 Multiphase Flow Simulator

The injection and migration of CO_2 in the target sandstone formation were simulated using the TOUGH2 V2 (Pruess et al., 2012) and ECO2N (Pruess and Spycher, 2007) multiphase flow modules incorporated into the TOUGHREACT V2.0 (Xu et al., 2011) and V3.0 (Sonnenthal et al., in prep.) reactive transport simulators. In other words, for the flow modeling effort in this section, TOUGHREACT was applied with the reactive chemistry options disabled, equivalent to running TOUGH2 V2 with the ECO2N equation of state module. A brief description of these simulators/modules is given in Appendix A1. At a later stage (Section 6) TOUGHREACT was then applied with the reactive chemistry options enabled.

2.3 Flow Model Design

For developing any numerical model, a suitable domain size and computational grid first need to be defined. In principle, a very large model domain can be used (e.g., few kilometers long and a few kilometers wide) such that the injected CO_2 will never reach the boundaries of the model domain such that appropriate boundary conditions can be imposed. Note, however, that the larger the model domain, the larger the computational cost. Additionally, to capture certain physical and chemical processes (e.g., to obtain estimates of pressure buildup near the injection well or to incorporate reactive transport processes), it is preferable to use fine gridding, which often restricts the maximum size of the model domain that can be practically used in a simulation.

It will therefore be convenient to have some *a priori* information regarding the expected extent of plume migration as a function of time resulting from a specific injection rate. A significant number of analytical and semi-analytical solutions are available in the literature which can provide estimates of the extent of the CO_2 plume migration, even though these analytical solutions have been developed with many simplifying assumptions. For example, Nordbotten and Celia (2006) assert that the extent of plume migration can be obtained from (see Figure 2.1)

$$\begin{aligned}\zeta(\xi,\tau) &= 1, \eta \le \frac{2}{\lambda} \\ &= \frac{1}{\lambda - 1}\left[\sqrt{\frac{2\lambda}{\eta}} - 1\right], \frac{2}{\lambda} < \eta < 2\lambda \\ &= 0, \eta \ge 2\lambda\end{aligned} \qquad \text{(Eq. 2.1)}$$

where $\eta = \frac{\xi^2}{\tau}$ is the similarity variable, and ξ and τ are dimensionless radial distance and time, respectively. In Equation 2.1, $\xi = r/\sqrt{k}$, and $\tau = Q_0 t/[2\pi H \varphi k(1 - S_{wr})]$, where Q_0 is the volumetric injection rate ($m^3\ s^{-1}$), r is radial distance (m), t is time (s), H is the depth or height of the storage formation (m), φ is porosity (-), k is absolute permeability (m^2), and S_{wr} is the residual saturation of brine. Furthermore, in Equation 2.1, λ (-) is the ratio of the phase mobilities, i.e., $\lambda = \lambda_g / \lambda_w$, where subscript '$g$' refers to the gas (or supercritical) phase and 'w' refers to the brine phase. The mobility (λ_α) of phase α is defined as $\lambda_\alpha = k_{r,\alpha}/\mu_\alpha$ (m s kg^{-1}). As noted in Nordbotten and Celia (2006), Equation 2.1 is strictly valid for negligible values of the dimensionless injection variable $\Gamma = \frac{2\pi\Delta\rho g k \lambda_w H^2}{Q_0}$. Note that Nordbotten and Celia (2006) assume an injection model with radial symmetry, where the fluid phases are incompressible and immiscible, and the assumptions of vertical equilibrium (Yortsos, 1995) are valid.

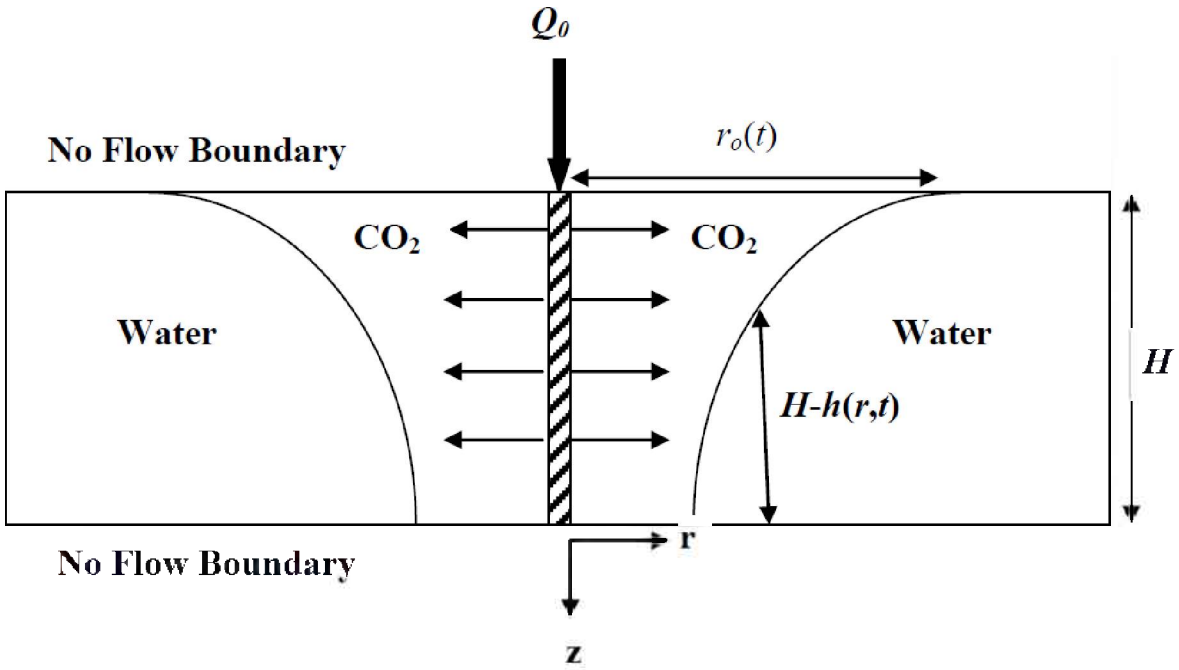

Figure 2.1. A schematic diagram showing a two-dimensional (2D) vertical cross section of a DSA with radial symmetry, where CO_2 is injected at the center trough a vertical well at the volumetric injection rate of Q_0. The radial location of the moving front at time t is $r_o(t)$, and its depth (from the top of the formation) is $h(r,t)$. The formation depth is H. This schematic diagram provides the basis for the conceptual model used by Nordbotten and Celia (2006) in developing their analytical solution for estimating the extent of plume migration at a specified time t.

For the Newark Basin, where the storage formation is located at an approximate depth of 1,524 m (5,000 ft) with a pressure of ~15 MPa and temperature of 53.8°C, CO_2 and water densities are ~666 and 992 kg m^{-3} (Lemmon et al., 2005), respectively, and their viscosities are 5.24×10^{-5} and 5.17×10^{-4} Pa-s, respectively. Assuming a formation permeability of 5×10^{-14} m^2 (see Section 2.5) and an injection rate of 1 MMt/year (or ~31.7 kg s^{-1}) of CO_2, Eq. 2.1 predicts the injection front to be at ~2,840 m at the end of a 30-year injection period. Note that in obtaining the front location, we have used the values of 0.1 for residual water saturation (S_{wr}) and, as an initial guess, the relative permeability of CO_2 ($k_{rel,\ nw}$) was assumed to be 1.0. If the relative permeability is assumed to be 0.7, still the migration distance is 1,987 m, or approximately 2,000 m. A question remains, however, regarding the speed of the plume after active injection ceases, for which there is no simple analytical solution.

Another estimate of the front location can be obtained from the derivations of Dentz and Tartakovsky (2009). They predicted that the inside radius of the plume will be located at $r_i(t)$ (see Figure 2.2) at time t, where $r_i(t)$ is given by

$$r_i(t) = \sqrt{\frac{2Q_0 t}{\pi\varphi H \gamma_{cw}}\left[\exp\left(\frac{2}{\gamma_{cw}}\right)-1\right]^{-1}} \qquad \text{(Eq. 2.2)}$$

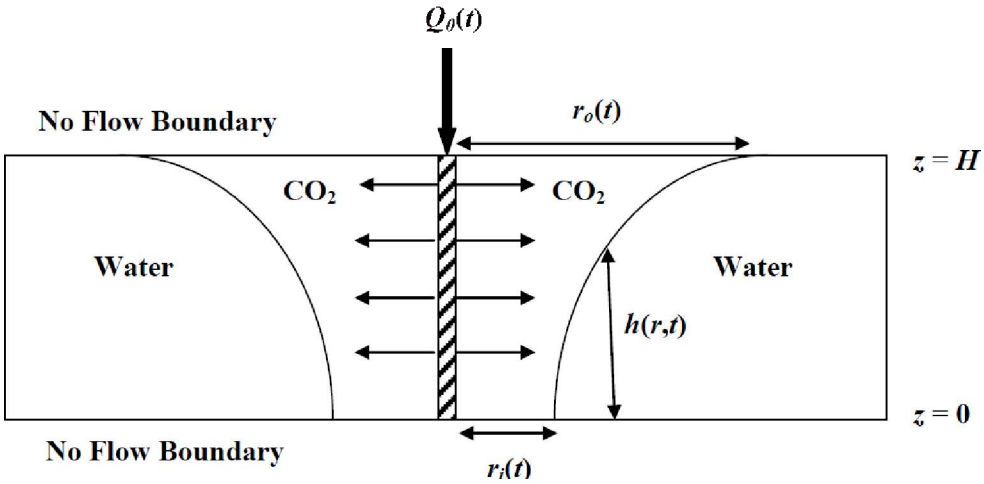

Figure 2.2. A schematic diagram showing a 2D vertical cross section of a DSA with radial symmetry, where CO_2 is injected at the center trough a vertical well at the volumetric injection rate of Q_0. The radial location of the moving front at time is $r_o(t)$, and its depth (from the bottom of the formation) is $h(r,t)$. The formation depth is H. The inner location of the moving front at time t is $r_i(t)$. This schematic diagram provides the basis for the conceptual model used by Dentz and Tartakovsky (2009) in developing their analytical solution for estimating the extent of plume migration at a specified time t.

Dentz and Tartakovsky (2009) also derived an expression for the outer radial location of the front, which is

$$r_o(t) = r_i(t)\exp\left(\frac{1}{\gamma_{cw}}\right) \qquad \text{(Eq. 2.3)}$$

In Equations 2.2 and 2.3, $\gamma_{cw} = \frac{Q_0}{2\pi k H^2 g}\frac{\Delta\mu}{\Delta\rho}$, where the symbols have their usual meanings (and have been defined in the context of Equation 2.1). If we introduce the values of the variables as applicable for the Newark Basin simulations, we see that the front is expected to be situated at 22,000 m at the end of the injection period, which is not quite convincing. Actually, while these solutions have been widely used for first-order estimates of plume locations, problems with these solutions have also been pointed out (Lu et al., 2009). For the sake of completeness, Juanes et al. (2010) also provide a set of analytical solutions to compute the location of the moving CO_2 front, which yields similar results.

The difficulty with these analytical solutions is not only that they predict wide ranges (which one should accept as reasonable without prior knowledge of system behavior) but also the fact that they assume radial symmetry. In a target formation such as that considered here, the storage capacity and injectivity is not well constrained. For example, the areal extent of the Stockton Formation is not precisely known. Additionally, the formation is inclined by a significant amount (as discussed in Section 1.2), a situation that cannot be modeled with simple radially symmetric models. Note that a gravity-current model for CO_2 immiscible flow in an inclined aquifer is available in the literature (Hesse et al., 2008); however, that model does not account for flow in the third dimension. In the following, we describe a model for flow of CO_2 and water in a three-dimensional (3D) model space.

In this 3D flow model, it is assumed that the fluids are immiscible and the assumptions of vertical equilibrium are valid, which implies that the length of the reservoir is considerably larger than its thickness (see Figure 2.3).

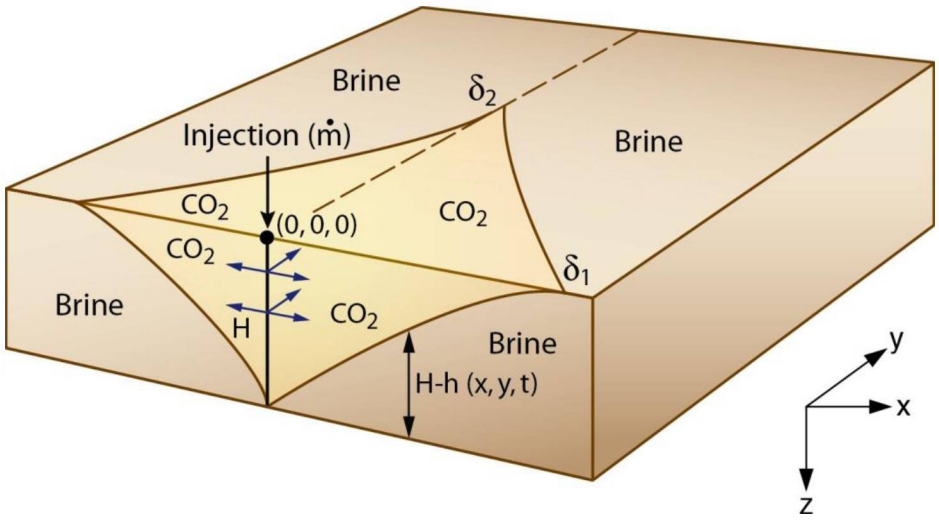

Figure 2.3. A schematic diagram of a 3D model domain representing a DSA in which CO_2 is injected at the center through a well at the rate of $\dot{m}$ kg s^{-1}. This conceptual representation forms the basis for the mathematical derivation in Appendix B for estimating the transient location of the advancing CO_2 plume in a 3D model domain. Note that δ_1 and δ_2 are the locations of the front at any time t along the *x*- and *y*-axis, resepectively at the top of the model domain.

The full derivation for the transient front locations is given in Appendix B. Briefly, if $\eta_1(\tau)$ and $\eta_2(\tau)$ are the dimensionless front locations in *x* and *y* directions, respectively, at dimensionless time τ in (see Appendix B for definitions of symbols), it can be shown that (Mukhopadhyay, unpublished)

$$erf(\eta_1)erf\left(\eta_2/\sqrt{a}\right)=\left[\frac{2\sqrt{a}}{a+1}\right]\left(\frac{\dot{m}_D}{\pi}\right) \qquad \text{(Eq. 2.4)}$$

where *a* is an anisotropic ratio (defined as the ratio of permeability in the *y* and *x* directions). Note that, if the system is isotropic with $a=1$, the term within the [-] on the right hand side of Equation 2.4 becomes unity and η_1 becomes equal to η_2 (from Equation B.31 in Appendix B), which then leads us to a simple expression for η_1, i.e.,

$$erf(\eta_1)=\sqrt{\frac{\dot{m}_D}{\pi}} \qquad \text{(Eq. 2.5)}$$

where $\dot{m}_D$ is the dimensionless injection rate (see Appendix B for definition). From Equation 4.5, it is easy to calculate the transient front location by using an inverse error function routine such as *erfinv* in

MATLAB. For anisotropic systems, the nonlinear equation in Equation 2.4 needs to be solved alongside another nonlinear algebraic equation (see Equation B.31 in Appendix B). This can be accomplished by using a nonlinear equation solver such as FSOLVE in the optimization toolbox of MATLAB, or simply by using the SOLVER function in Excel.

When the relevant parameters for injection into Newark Basin are introduced in Equation 4.5, we see that the front is supposed to be located at 1,490 m at the end of the injection period. When we present the numerical simulation results with the base-case property set (see Section 2.7), we will see that this estimate is much closer to the numerical simulation results in comparison to the other analytical solutions. These estimates give us an idea about how large a model domain we need for simulating the injection processes at Newark Basin. In the next section, we discuss the model domains used for flow-only and reactive transport simulations and the numerical grid used for these purposes.

2.4 Model Domain and Numerical Grid

The primary objectives of the flow modeling are to assess the (1) extent of CO_2 plume migration during both the active injection period and an extended observation period after injection ceases, (2) fate of the injected CO_2 in terms of what fraction of it that remains as a free compressed "gas" phase (i.e., supercritical fluid phase) and what fraction becomes dissolved in the aqueous phase, and (3) expected pressure buildup near the injection location. From the nature of the underlying physical processes, as discussed in Section 2.1, different time scales are involved in modeling the fate of the injected CO_2 (both in terms of plume migration and partitioning of injected CO_2 between the CO_2-rich compressed "gas" and aqueous phases) and pressure evolution associated with the injection process. For assessing the fate of the plume, we need to model the physical processes over a large spatial domain (a few kilometers in both x and y directions) and also a large temporal scale (we will restrict ourselves to 100 years in this report). On the other hand, for assessing pressure buildup, we need to focus on processes occurring over much shorter spatial and temporal scales. While the former needs to be simulated with a numerical grid extending over a larger spatial domain but with acceptable coarse gridding, the latter requires a much more refined grid but covering a smaller spatial domain. Given this situation, if we were to use the same numerical grid for both the objectives, a very large grid (to capture the long term flow behavior) with extreme refinement (to capture the pressure behavior near the injection well) will be needed. Such an approach is not practical because of the large computational demands, more so because we are aiming for full 3D flow simulations. We thus use different numerical grids for these different objectives.

Most of the 3D flow simulations presented in this report have been performed with a 3D model domain that extends 16,000×16,000 m in x and y directions, respectively, and is 150 m thick in the vertical (z) direction. Note that, because of symmetry, we have used only half of the model domain (i.e., 8,000 m) in the y direction for numerical simulations. The gridblocks are 5×5×5 m at and near the injection location, however, away from that location, the gridblock sizes are gradually increased, even though the vertical discretization always remains 5 m. The extent of the model domain and level of discretization was decided based upon a series of scoping simulations with numerical grids of varying degrees of complexity, and we found that the above-mentioned numerical grid was mostly adequate and optimum (in terms of time required for one simulation, number of simulations that need to be performed to address parameter sensitivity reasonably and satisfactorily, and the level of precision needed at this stage of

preliminary predictive modeling). This 3D numerical mesh has 57,660 gridblocks, and 168,268 connections between them, and is shown schematically in Figure 2.4.

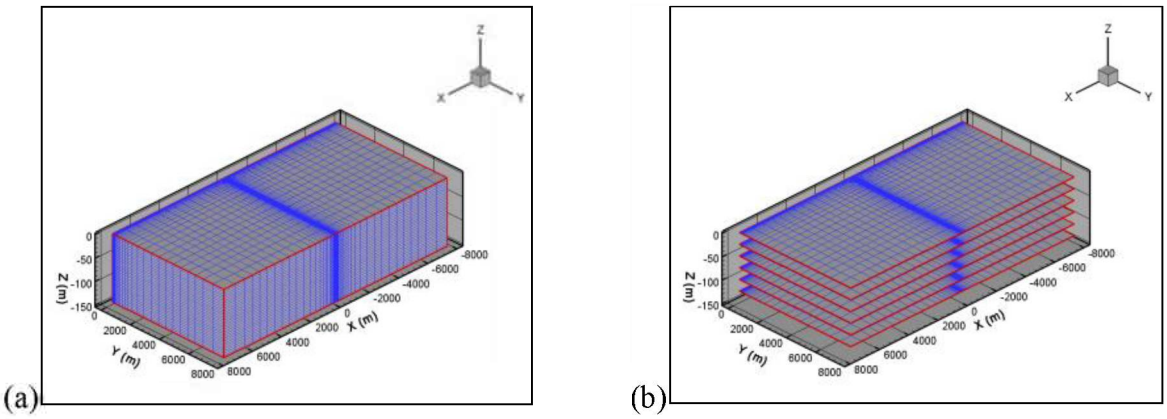

Figure 2.4. A graphical representation of the 3D numerical mesh used in the base-case CO_2 injection simulations. This numerical mesh represents a 16,000×16,000×150 m model domain, and has 57,600 gridblocks. The base-case simulations use the base-case hydrologic property set provided in Table 2.7. (a) The full 3D model domain (exposed surfaces are shown), and (b) selected horizontal planes of the 3D model domain.

Note that, while performing the sensitivity studies—more specifically for those sensitivity simulations which required us to use permeability values that were significantly larger than the base-case permeability values or for formations that are significantly inclined—we realized that an even larger model domain was needed. Consequently, a larger numerical mesh was generated that covered a model domain of 24,000×24,000×150 m (Note that, as before, only half the model domain in *y* direction was needed because of symmetry.) In this numerical mesh, the gridblocks near the injection location are 10×10×10 m and are larger farther away from the injection point. The vertical discretization in this numerical mesh is always maintained at 10 m. The other defining feature of this numerical mesh is that the gridblocks are never larger than 500 m. This numerical mesh has 45,630 gridblocks and 132,093 connections between them.

One of the main characteristics of the Newark Basin stratigraphy is that its geologic formations have a significant dip (between 8° to 14°; Figure 1.1; thus, the model domain needs to be tilted to model the dipping formation). When CO_2 is injected in such a dipping formation, the forces of buoyancy drive it upwards along the top boundary from the point of injection. In other words, the extent of plume migration is much larger in the up-dip direction compared to the down-dip direction. Consequently, the spread of the injected CO_2 plume is asymmetric around the injection point, and this is the main reason a radial mesh cannot be used to estimate CO_2 migration distance in dipping formations such as the Newark Basin. Therefore, we used a tilted 3D numerical mesh for that purpose. To do this, we simply tilted the 3D parallelepiped domain discussed in the preceding two paragraphs by 8°, which we assessed to be a reasonable value for the dip of the Stockton Formation. Note that, because the top of the Stockton Formation is situated 1,524 m below the ground surface at the location of interest, if we tilt it by 8°, it touches the ground surface at a distance of about 11,000 m from the injection point. We thus restrict the

numerical mesh to 12,000×11,000×150 m for situations where the mesh is tilted by 8° such that the entire model domain remains below ground surface.

For estimating pressure evolution, where the focus is on short-term processes, formation dip is not a controlling factor. Thus, for simulations designed to estimate pressure buildup near the injection well, it is acceptable to use a radial numerical mesh. This is justified because, in the short term, flow around the injection well is expected to be radial, and pressure buildup is mostly controlled by radial flow (instead of linear flow, which controls the migration pattern in the long term and far away from the injection well, and particularly in a dipping formation). To this end, we generated a radial mesh extending 10,000 m radially with thickness of 150 m in the vertical direction. The gridblocks near the injection location are 2 m wide (radially), and gradually coarsen farther away from it. The discretization in the vertical direction is non-uniform, with the gridblocks in the injection interval being 2 m thick and gradually increasing to 5 m towards the top of the storage formation. Note that we did not attempt to simulate the actual flow processes inside the injection borehole. Thus, the pressure estimates obtained with these numerical simulations can be construed as the averages over a 2 m radial distance and 2 m depth. This radial numerical mesh has 6,820 gridblocks, and 13,461 connections between them.

2.5 Rock Properties

In this study, we used rock properties measured on (or representative of) core samples collected in NYSTA Tandem Lot Well #1. This well (see Section 1.2) was sited in the (NYSTA Tandem Truck Lot adjacent to west-bound entrance to I-287 at Exit 14. The site was chosen due to its central location in the northern part of the Newark Basin, and its accessibility for equipment. Additionally, this site is advantageous because it is directly adjacent to the 13 mile east-west (E-W) seismic line shot along I-287. The well was permitted through three agencies; the United State Environmental Protection Agency (USEPA), New York State Department of Conservation (NYSDEC), and the Rockland County Department of Health (RCDOH). The NYSDEC issued permits to drill, plug, and abandon the well in May, 2011. Surface casing for the well was completed by Ziegenfuss Drilling Inc., and the borehole was completed at a total depth of 6,881 (2,097 m) feet by Union Drilling Inc. in October 2011. 150 feet (46 m) of continuous core was collected during drilling. 50 sidewall cores and a full suite of wireline logs were collected prior to plugging. Site restoration was completed in December 2011. Interpreted data from the E-W seismic line shows the overall geometry of the basin. Although the initial intention of the NYSTA Tandem Lot Well #1 was to sample the formations below the Palisade Sill in hopes of finding an equivalent to the Stockton sandstone, the focus eventually shifted to the 1,500 ft (~457 m) of porous sandstone lying above the sill. The rock properties used in this report (for flow-only and reactive transport simulations) are mostly derived from the cores collected at the NYSTA Tandem Lot Well #1.

2.5.1 Absolute permeability, porosity, and grain density

Open-hole logs at the location of the NYSTA Tandem Lot Well #1 indicate three potential flow units (see Table 2.1): Flow Unit 1 at depths of 2,110-2,465 ft (643-751 m), Flow Unit 2 at depths of 2800-3300 ft (853-1,006 m), and Flow Unit 3 at depths of 3,650-4,250 ft (1,113-1,295 m). Within each of these flow units, the formation is classified into two categories, namely "rock" and "reservoir," depending on

average fractional clay volume, average effective porosity, and average permeability. Note that, because of its shallower depths, Flow Unit 1 may not provide supercritical conditions for CO_2 storage, and thus Flow Unit 2 and 3 remain the best choice.

Table 2.1. Location, average porosity and permeability, and clay volume fractions of potential flow units as identified from cores collected from the NYSTA Tandem Lot Well #1. Numbers within ( ) represent the depth information in m.

Zones	Flag Name	Top (ft)	Bottom (ft)	Avg. Porosity	Avg. Permeability (mD)	Avg. Clay Volume Fraction
Flow_Unit_1	ROCK	2,110 (643)	2,465 (751)	0.110	79.51	0.115
Flow_Unit_1	RES	2,110 (643)	2,465 (751)	0.114	85.08	0.108
Flow_Unit_1	PAY	2,110 (643)	2,465 (751)			
Flow_Unit_2	ROCK	2,800 (853)	3,300 (1,006)	0.075	37.78	0.147
Flow_Unit_2	RES	2,800 (853)	3,300 (1,006)	0.108	59.86	0.101
Flow_Unit_2	PAY	2,800 (853)	3,300 (1,006)			
Flow_Unit_3	ROCK	3,650 (1,113)	4,250 (1,295)	0.039	8.31	0.16
Flow_Unit_3	RES	3,650 (1,113)	4,250 (1,295)	0.088	30.46	0.096
Flow_Unit_3	PAY	3,650 (1,113)	4,250 (1,295)			

Table 2.2 is excerpted from the core data provided to the LBNL modeling team by Sandia Technologies. Along with the sample number and its collection depth, Table 2.2 lists the net confining stress (NCS), permeability (both air permeability and Klinkenberg permeability), porosity (under both ambient and NCS conditions)), grain density, and water saturation percent for each core sample. At the bottom of the table, we list the arithmetic average value of each of the above parameters. Note that there are a total of 46 core samples in Table 2.2. Of these 46 samples, 31 have been collected from depths of 2,500 ft (762 m) or shallower (622–2,460 ft or 190–750 m), i.e., they are collected from within Flow Unit 1 or even shallower depths. There are 12 other samples that are located completely within Flow Unit 2 (depths of 2,832–3,082 ft or 863-939 m), and three samples are from deeper depths (3,753–4,191 ft or 1,144–1,277 m).

Table 2.2. Net confining stress (NCS), permeability (both air permeability and Klinkenberg permeability), porosity (under both ambient and NCS conditions), grain density, and water saturation percent for each of the available core samples (46 in number) collected from the NYSTA Tandem Lot Well #1.

Sample Number	Sample Depth, feet	Sample Depth, m	Confining Stress, psi	Permeability, millidarcys		Porosity, percent		Grain Density, gm/cc	Water Saturation, percent
				to Air	Klinkenberg	Ambient	NCS		
1-1R	622.0	190	200	160.	144.	13.4	13.4	2.67	87.0
1-2R	689.0	210	200	538.	505.	16.2	16.2	2.66	88.5
1-3R	705.0	215	200	200.	182.	14.7	14.7	2.66	88.4

1-6R	752.0	229	200	0.764	0.581	9.4	9.4	2.67	81.8
1-7R	811.0	247	300	51.9	44.7	10.6	10.6	2.66	99.3
1-8R	829.0	253	300	1080.	1020.	16.0	16.0	2.65	86.8
1-9R	833.0	254	300	0.052	0.027	11.1	11.1	2.71	93.0
1-10R	904.0	276	300	16.4	13.4	12.2	12.2	2.67	88.0
1-11R	966.0	294	300	193.	175.	17.4	17.4	2.68	87.9
1-12R	1,017.0	310	300	17.1	13.9	8.4	8.4	2.68	67.5
1-14R	1,034.0	315	300	496.	464.	16.7	16.7	2.65	86.4
1-15R	1,082.0	330	300	248.	228.	13.1	13.1	2.66	84.7
1-17R	1,172.0	357	400	51.2	44.0	11.9	11.9	2.66	69.9
1-18R	1,181.0	360	400	0.012	0.0044	6.1	6.1	2.70	76.0
1-21R	1,263.0	385	400	0.0091	0.0032	5.8	5.7	2.69	67.6
1-22R	1,319.0	402	400	0.022	0.0095	7.3	7.3	2.70	**
1-23R	1,393.0	425	400	0.0046	0.0013	7.7	7.7	2.73	98.9
2-4R	2,262.0	689	700	2.16	1.71	5.6	5.6	2.68	68.5
2-5R	2,265.0	690	700		+	13.4		2.63	59.6
2-6R	2,268.0	691	700	137.	123.	12.0	11.9	2.64	77.1
2-7R	2,318.0	707	700						
2-8R	2,318.5	707	700		+	20.5		2.63	86.0
2-9R	2,321.0	707	700		+	10.7		2.64	67.3
2-10R	2,334.0	711	800	1.11	0.850	7.7	7.7	2.68	66.1
2-11R	2,336.0	712	800	23.8	20.0	12.5	12.5	2.66	81.8
2-12R	2,338.0	713	800	0.027	0.012	3.6	3.5	2.69	**
2-13R	2,438.0	743	800	53.4	46.2	11.6	11.5	2.66	73.5
2-14R	2,440.0	744	800	79.2	69.8	12.3	12.2	2.64	82.3
2-15R	2,451.0	747	800	4.55	3.59	10.9	10.9	2.65	76.4
2-16R	2,456.0	749	800	121.	108.	13.8	13.7	2.64	83.1
2-17R	2,460.0	750	800	79.2	69.8	11.7	11.6	2.64	84.4
2-20R	2,832.0	863	900	257.	236.	15.4	15.3	2.64	86.2
2-21R	2,835.0	864	900	64.9	56.7	11.6	11.5	2.65	80.7
2-22R	2,838.0	865	900	355.	329.	14.4	14.3	2.65	85.6
2-24R	3,053.0	931	1000	110.	98.5	15.7	15.6	2.64	84.4
2-25R	3,055.0	931	1000	23.6	19.7	13.2	13.1	2.66	88.6
2-26R	3,057.0	932	1000	1300.	1240.	15.1	15.0	2.64	78.1
2-27R	3,059.0	932	1000	1780.	1700.	12.4	12.3	2.63	64.9
2-28R	3,064.0	934	1000	343.	318.	11.3	11.2	2.64	74.7
2-29R	3,066.0	935	1000	875.	829.	11.7	11.6	2.65	79.0
2-30R	3,077.0	938	1000	27.7	23.4	14.4	14.3	2.66	85.7
2-31R	3,080.0	939	1000	244.	224.	13.1	13.0	2.65	81.9
2-32R	3,082.0	939	1000	23.7	19.8	13.6	13.5	2.65	90.1
2-37R	3,753.0	1,144	1200	0.080	0.045	9.1	9.0	2.62	98.8
2-38R	3,757.0	1,145	1200	0.223	0.145	10.6	10.5	2.63	94.5
2-41R	4,191.0	1,277	1400	0.013	0.0049	2.3	2.2	2.63	**
			Average values:	213.	199.	11.7	11.5	2.66	81.7

+ Indicates sample is unsuitable for this type of measurement

** Pore volume is insufficient for analysis of fluid saturations

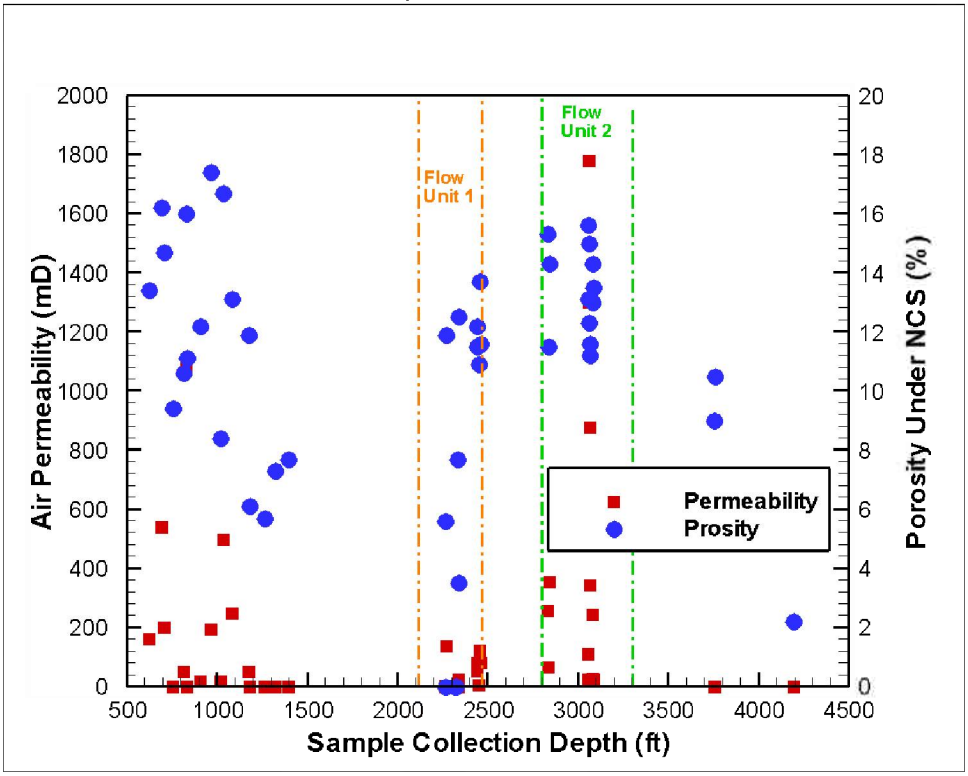

Figure 2.5. Air permeability and porosity under net confining stress (NCS) as function of depth for all 46 core samples from NYSTA Tandem Lot Well #1.

In Figure 2.5, we show the variation in air permeability and effective porosity under NCS as a function of depth of sample collection. Observe that there are 14 core samples in Flow Unit 1 with a geometric mean permeability of 11 mD (and a range of 0.027-137 mD). From where NYSTA Tandem Lot Well #1 is located within the Newark Basin, this flow unit most likely consists of predominantly sands and shales. It also is located above 2,500 ft (762 m), which is the cut-off depth for supercritical CO_2 storage. It is therefore prudent not to consider the mean permeability of this flow unit as the representative permeability of the storage formation. As far as Flow Unit 2 is concerned, 12 core samples are available in that unit, whose geometric mean average is 185 mD with a range of 23.6-1780 mD. This flow unit at the location of the well is situated fully within the reservoir flow unit. On the other hand, the three samples that are available from Flow Unit 3, even though they are also within the reservoir flow unit, have a geometric mean permeability of 0.06 mD (range of 0.013-0.223 mD), which of course is not representative of the formation.

Without having any data to constrain the lateral and vertical permeabilities, and with available data showing such wide variability, selecting an average permeability remains a challenge, and any number selected leaves a lot of uncertainty. Having mentioned these limitations, and noting that the target storage formation in the conceptual model presented in this report is situated at a depth of 5,000 ft (1,524 m), we have set a permeability of 50 mD for the base-case value. To address the uncertainty in permeability in

both the lateral and vertical directions, sensitivity studies with a large range of permeability values will be performed (see later for details on sensitivity studies).

As far as porosities are concerned, the average values are 10.1%, 13.4%, and 7.2% (not quite representative given that there are only 3 samples) in Flow Unit 1, 2, and, 3, respectively. The average porosity of all samples in Flow Unit 2 and 3 is 12.6%. We thus select an average porosity of 13% for the base-case simulations. Grain density is selected as 2,650 kg m^{-3}, which is close to the average value from the collected samples.

2.5.2 Liquid- and gas-phase relative permeabilities

One of the key parameters affecting fate and transport of the injected CO_2 in the subsurface is its relative permeability, which is a property of both the rock and the fluid phases involved. Relative permeability is a parameter that quantifies the extent to which the injected CO_2 and the formation fluids (e.g., brine) interfere with each other as they move through the pore-space of the rocks. It affects not only the spatial extent of the plume but also the injectivity of a well, extent of capillary trapping, and leakage through the seal (Bennion and Bachu, 2008, 2010; Bachu, 2013; Benson et al., 2013). In numerical simulations, which are designed to accurately predict the subsurface migration of CO_2, one needs to provide relative permeability data for the fluid phases involved as an input, either as a constitutive relationship or measured data in a tabulated form. In this report, we fit measured relative permeability data from cores collected within the Newark Basin to standard relative permeability curves to generate smooth relative permeability versus (water) saturation functions, and provide these relative permeability functions as input to the simulator. The measured relative permeability data and the curve fitting process is explained in more detail below.

Liquid- and gas-phase relative permeabilities, k_{rl} and k_{rg}, respectively, as a function of (water) saturation for a total of seven core samples were made available to the LBNL modeling team. All seven samples are from NYSTA Tandem Lot Well #1 and they have been collected at different depths. Of these seven core samples, sample number 2-21R did not produce enough relative permeability data to generate a relative permeability versus saturation curve. As a result, this sample is not included in this analysis. Table 2.3 provides the k_{rl} and k_{rg} data for the remaining six core samples as a function of liquid saturation. Note that the relative permeability data were estimated using the unsteady-state method under a NCS of 800 psi (~5.5 MPa) and a temperature of 72°F (22.2°C). Figure 2.6(a) shows k_{rl} as a function of liquid saturation for all six samples, and Figure 2.6(b) shows k_{rg} as a function of liquid saturation for these samples.

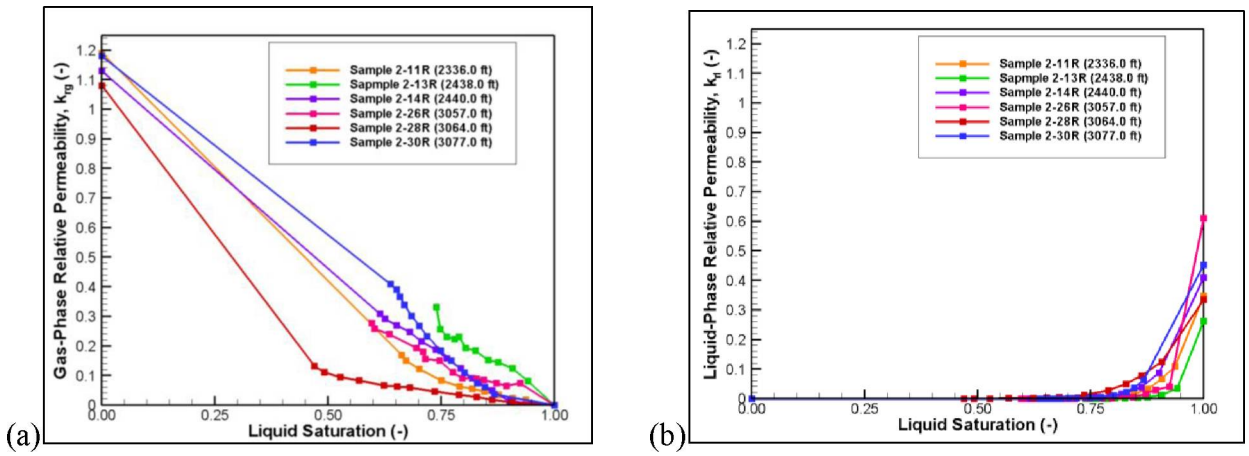

Figure 2.6. Measured relative permeabilities as a function of liquid saturation for six core samples collected from NYSTA Tandem Lot Well #1. (a) Measured gas-phase relative permeabilities, and (b) measured liquid-phase relative permeabilities.

Table 2.3. Measured gas-phase and liquid-phase relative permeability data from six core samples collected from NYSTA Tandem Lot Well #1, (a) Sample 2-11R (collection depth 2,336 ft or 712 m), (b) Sample 2-13R (collection depth 2,438 ft or 743 m), (c) Sample 2-14R (collection depth 2,440 ft or 744 m), (d) Sample 2-26R (collection depth 3,057 ft or 932 m), (e) sample 2-28R (collection depth 3,064 ft or 934 m), and (f) Sample 2-30R (collection depth 3,077 ft or 938 m).

(a)

Gas Saturation	Gas-phase relative permeability	Liquid-phase relative permeability
0	0	0.349
0.063	0.0177	0.11
0.092	0.0245	0.067
0.123	0.035	0.0334
0.155	0.046	0.0153
0.181	0.055	0.0081
0.209	0.064	0.0044
0.25	0.083	0.00185
0.299	0.122	0.00045
0.328	0.15	0.000127
0.338	0.17	1.00E-20
1	1.19	1.00E-20

(b)

Gas Saturation	Gas-phase relative permeability	Liquid-phase relative Permeability
0	0	0.262
0.058	0.0821	0.036
0.092	0.124	0.013
0.124	0.146	0.005
0.146	0.153	0.003
0.174	0.185	0.002
0.196	0.194	0.001
0.211	0.23	1E-20
0.221	0.224	1E-20

0.237	0.23	1E-20
0.252	0.257	1E-20
0.261	0.331	1E-20

(c)

Gas Saturation	Gas-phase relative permeability	Liquid-phase relative Permeability
0	0	0.262
0.058	0.0821	0.036
0.092	0.124	0.013
0.124	0.146	0.005
0.146	0.153	0.003
0.174	0.185	0.002
0.196	0.194	0.001
0.211	0.23	1E-20
0.221	0.224	1E-20
0.237	0.23	1E-20
0.252	0.257	1E-20
0.261	0.331	1E-20

(d)

Gas Saturation	Gas-phase relative permeability	Liquid-phase relative permeability
0	0	0.61
0.075	0.075	0.04
0.106	0.066	0.03
0.128	0.074	0.016
0.156	0.085	0.0057
0.172	0.089	0.0084
0.204	0.091	0.0021
0.224	0.111	0.0027
0.253	0.15	0.002
0.285	0.157	0.00076
0.29	0.18	0.00059
0.305	0.194	0.00042
0.365	0.24	0.0002
0.397	0.258	0.000026
0.403	0.278	1E-20

(e)

Gas Saturation	Gas-phase relative permeability	Liquid-phase relative permeability
0	0	0.336
0.092	0.00931	0.1239
0.137	0.0179	0.0784
0.172	0.0279	0.0502
0.211	0.035	0.0279
0.265	0.047	0.0136
0.319	0.06	0.0051
0.348	0.064	0.0034
0.377	0.067	0.00218
0.431	0.083	0.00088

0.473	0.094	0.00036
0.509	0.112	0.000106
0.531	0.133	1.00E-20
1	1.08	1.00E-20

(f)

Gas Saturation	Gas-phase relative permeability	Liquid-phase relative permeability
0	0	0.452
0.133	0.0376	0.0634
0.154	0.062	0.0373
0.17	0.075	0.0227
0.198	0.11	0.0117
0.228	0.15	0.00614
0.251	0.184	0.00343
0.281	0.232	0.00165
0.298	0.268	0.00104
0.316	0.302	0.000637
0.331	0.338	0.000385
0.341	0.367	0.000269
0.349	0.391	0.000185
0.362	0.409	1.00E-20
1	1.18	1.00E-20

From Figure 2.6(a), it is observed that the gas-phase relative permeability data are not extensive. There exists almost no gas- or liquid-phase relative permeability data when liquid saturation is less than 50%. When CO_2 is injected into a DSA, liquid saturation near the injection well declines rapidly and the supercritical CO_2 "gas" saturation builds up accordingly. Note that liquid-saturation near the injection well decreases not only because of displacement by the invading supercritical CO_2 "gas" phase but also because of strong evaporation effects of water into this phase. At very early times during the injection process, liquid saturation close to the injection may fall below 50%, with its relative permeability dropping close to zero and gas relative permeability increasing. Subsequent plume migration is controlled to a large extent by this jump in gas-phase relative permeability. If no data exist for this region, it poses a challenge in developing a representative relative permeability curve, and some uncertainties will remain no matter what curve we use in the simulations, particularly when these curves are developed on such limited data.

The key factor controlling relative permeability is the rock/fluid combination. In other words, if the rock/sediment types were similar, we could accept the relative permeability data from a core sample even if it were from much shallower depths. However, core samples 2-11R, 2-13R, and 2-14R were not only collected from shallower depths, they also represented rock types that were different from the rock type expected in the storage formation. As a result, we excluded relative permeability data from core samples 2-11R, 2-13R, and 2-14R (even though sample 2-14R provides a reasonable looking set of relative permeability data). The gas-phase relative permeability data measured in sample 2-26R, though this sample is from reservoir flow sandstone units, are not smooth. This leaves us with two samples: 2-28R and 2-30R. Note that these two sets coincidentally provide a lower and upper limit on gas-phase relative permeability data (discounting the data from sample 2-13R). We fitted both these sets to the van

Genuchten relationship (for liquid-phase relative permeability) and to the Corey relationship (for gas-phase relative permeability) as given in Equations A1.8 and A1.9, respectively. The fitted phase relative permeabilities for these two core samples are shown in Figures 2.7 (for core sample 2-28R) and 2.8 (for core samples 2-30R). For convenience, Figures 2.7 and 2.8 also show the measured relative permeability data. The parameters obtained from fitting are shown in Table 2.4. Note that, where there is little basis upon which to choose one sample from the other as far as liquid-phase relative permeability is concerned (which is to a large extent controlled by the van Genuchten parameter *m* (see Equation A1.8), we needed to use an unrealistic residual liquid saturation (S_{lr}) of 0.47 to match the measured gas-phase relative permeability data of sample 2-30R. We thus selected the parameters obtained by fitting the relative permeability data of sample 2-28R to generate the gas- and liquid-phase relative permeability data for the base-case flow and transport simulations.

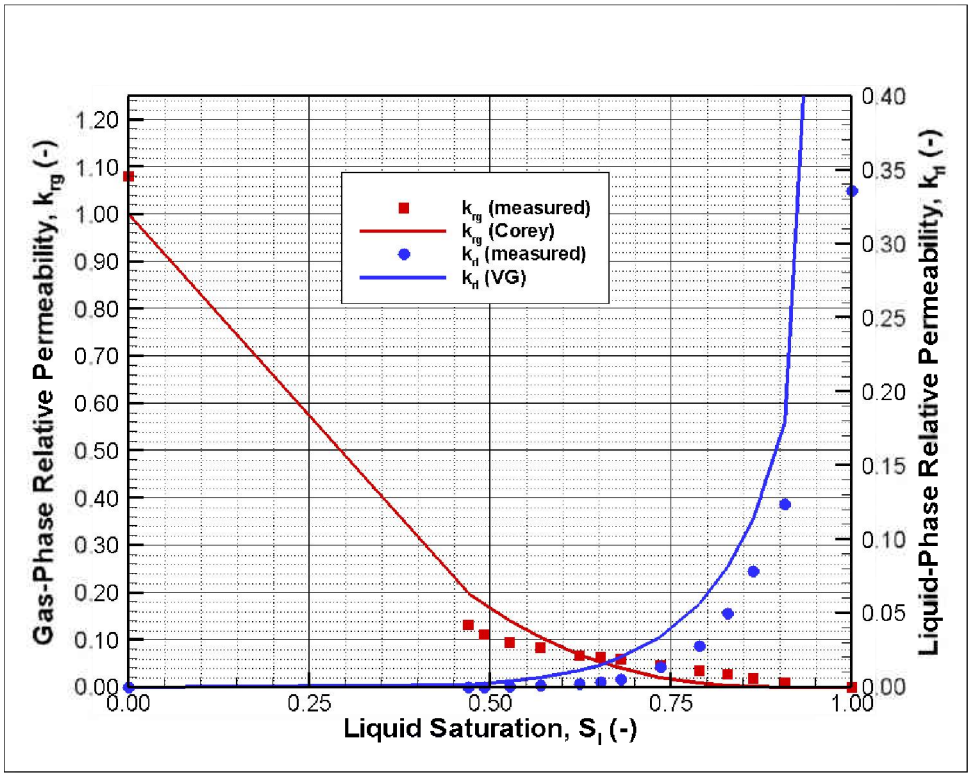

Figure 2.7. Measured and fitted gas-phase and liquid-phase relative permeabilities for NYSTA Tandem Lot Well #1 core sample 2-28R.

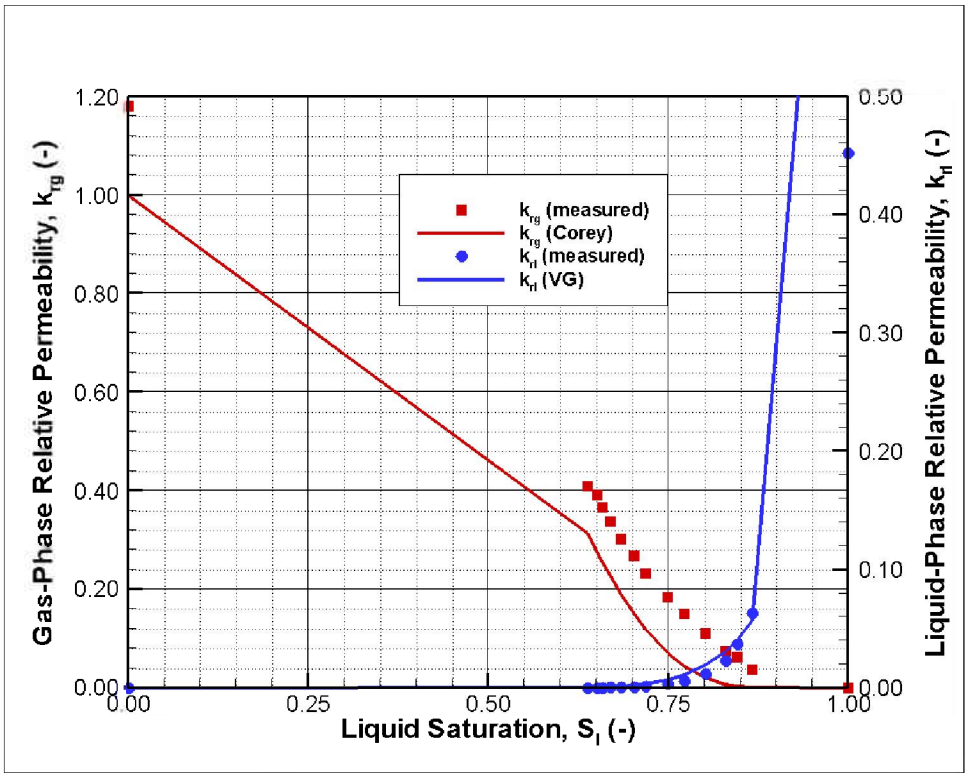

Figure 2.8. Measured and fitted gas-phase and liquid-phase relative permeabilities for NYSTA Tandem Lot Well #1 core sample 2-30R.

Table 2.4. Parameters obtained from fitting the measured gas- and liquid-phase relative permeability data of samples 2-28R and 2-30R. The estimated parameters are used in generating smooth relative permeability curves for the gas and liquid phases using Equation A1.8 and A1.9, respectively, and the curves thus generated are used in the flow and transport simulations.

Core Sample	Residual Gas Saturation (S_{gr})	Residual Liquid Saturation (S_{lr})	Van Genuchten m
2-28R	0.05	0.01	0.38
2-30R	0.10	0.47	0.42

2.5.3 Capillary pressure of water-CO_2 systems

The dependence of capillary pressure (P_c) on wetting phase (i.e., water or brine) saturation (S_w) under reservoir conditions is a basic constitutive relation needed to predict CO_2 flow and capillary trapping during sequestration. In this context, it is worth noting that knowing only the dependence of relative permeability on S_w is not enough to accurately predict fluid flow or equilibrium saturations in a system involving multiphase flow of different fluids. It is also essential to include a capillary pressure relationship in the mathematical description of such multiple fluid systems. More specifically, in geologic carbon sequestration, where capillary trapping is expected to be one of the key storage mechanisms, a

reliable $P_c(S_w)$ constitutive relationship for the water/scCO$_2$ system is needed for reliably predicting the fate of the injected CO$_2$ and estimating the storage potential of a reservoir.

Because of the paucity of actual capillary pressure/saturation data in water-sc CO$_2$ systems, these data are often obtained by suitable scaling of mercury injection pressures. Results from mercury injection tests with seven core samples collected from NYSTA Tandem Lot Well #1 were included in the data package provided to the LBNL modeling team by Sandia Technologies. These seven samples are 2-6R (at 2,268 ft or 691 m), 2-10R (at 2,334 ft or 711 m) and 2-15R (at 2,451 ft or 747 m) in Flow Unit 1; 2-20R (at 2,832 ft or 863 m), 2-24R (3,053 ft or 931 m), 2-31R (at 3,080 ft or 939 m) and in 2-38R (at 3,757 ft or 1,145 m) in Flow Unit 2. Furthermore, mercury injection test results from three Princeton NBCP cores were also supplied: PC-44 (at 1,311 ft or 400 m), PC-41 (at 1,464 ft or 446 m), and PC-34 (at 1,714 ft or 522 m). These last three samples, being collected from much shallower depths and the rock types being different when compared to the target formation, are not relevant for the modeling studies presented in this report.

From the mercury saturation versus capillary pressure data provided in the data package, we obtain the capillary pressure curve for the water–scCO$_2$ system, where scCO$_2$ implies supercritical CO$_2$, using the relationship

$$P_{C2} = P_{C1}\left(\frac{\sigma_2}{\sigma_1}\right)\left(\frac{\cos\theta_2}{\cos\theta_1}\right) \qquad \text{(Eq. 2.6)}$$

In Equation 2.6, subscript 2 refers to water–scCO$_2$ system, and subscript 1 refers to mercury-air system. Additionally, σ refers to interfacial tension (IFT) and θ is the contact angle between the two fluid phases.

The contact angle (140°) and IFT (485 mN/m) for the mercury-air system are adopted from the literature. The water-scCO$_2$ contact angle with different mineral system is investigated by different authors (Bikkina, 2011; Chiquet et al., 2005; Yang and Gu, 2004). Bikkina (2011) carried out experiments of water-CO$_2$ with quartz and carbonate systems from 200-3000 psi and 77-122°F. From these experiments (Bikkina, 2011), contact angle of water/CO$_2$/quartz at higher temperatures decreases from 45° (135°) at 77°F to 20° (160°) at 122°F. Here, we choose the water/CO$_2$ contact angle as 160° (corresponding to a temperature of 50°C). Chiquet et al. (2007a) did experiments about CO$_2$-water (brine) IFT at a range of temperatures (308 –383 K) and pressures (5 – 45 MPa). For CO$_2$/pure water at conditions closest to the assumed pressure and temperature of the target formation (53.8°C and 15 MPa), the interfacial tension is 32 mN/m. Through their experiments, they reported that NaCl dissolved in water has negligible effect on IFT. Here we use 32 mN/m as IFT of CO$_2$/water. As an example, the computations of equivalent water-scCO$_2$ capillary pressure from the mercury injection tests for sample 2-6R are shown in Table 2.5. Figure 2.9 shows the calculated water-scCO$_2$ capillary pressure versus water saturation curves for all 10 samples (7 from the NYSTA Tandem Lot Well #1 cores and 3 from the Princeton NBCP cores).

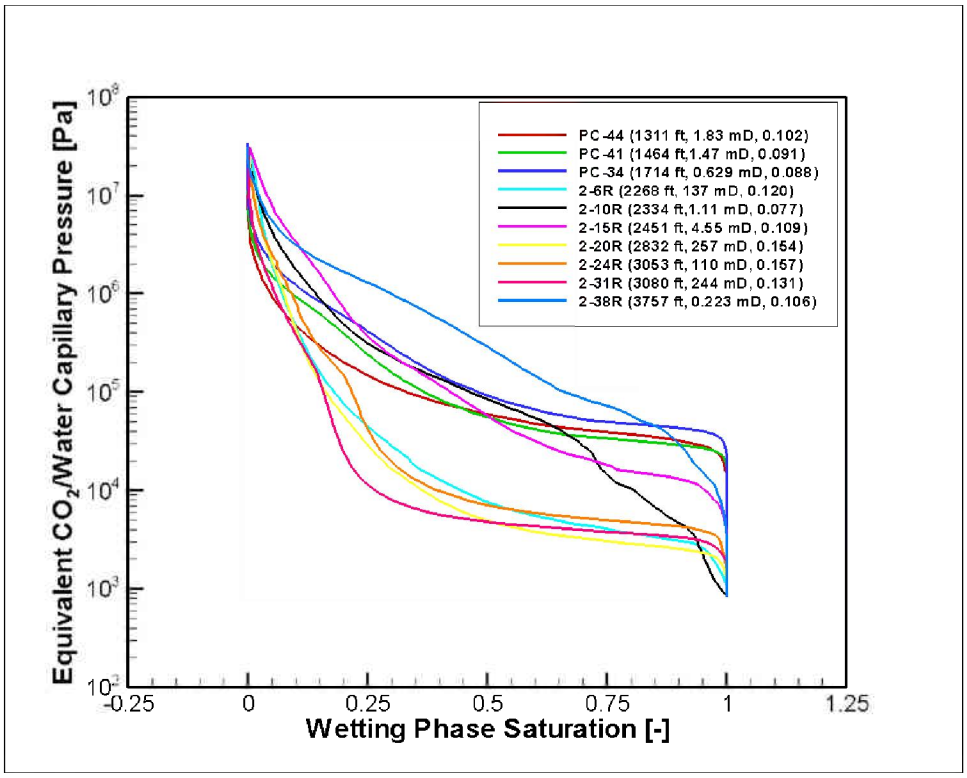

Figure 2.9. Calculated water-$scCO_2$ capillary pressure versus water saturation curves for ten core samples (seven from NYSTA Tandem Lot Well #1 cores, and three from the Princeton NBCP cores). The water-$scCO_2$ capillary pressure curves were obtained from measured mercury injection pressures in those core samples by using Equation 2.6.

Table 2.5. Computation of water-$scCO_2$ capillary pressure from mercury injection tests using Equation 2.6 in core sample 2-6R with sample collection depth of 2,268.0 ft (691 m).

Wetting Phase Saturation	Mercury Injection Pressure (psia)	Equivalent Water/$scCO_2$ Capillary Pressure (psi)	Equivalent Water-$scCO_2$ Capillary Pressure (Pa)
1.00E+00	1.52E+00	1.23E-01	8.47E+02
1.00E+00	1.61E+00	1.30E-01	8.98E+02
1.00E+00	1.82E+00	1.47E-01	1.02E+03
9.97E-01	2.02E+00	1.63E-01	1.13E+03
9.94E-01	2.18E+00	1.77E-01	1.22E+03
9.91E-01	2.37E+00	1.92E-01	1.32E+03
9.87E-01	2.59E+00	2.10E-01	1.45E+03
9.83E-01	2.82E+00	2.28E-01	1.57E+03
9.78E-01	3.10E+00	2.51E-01	1.73E+03
9.73E-01	3.40E+00	2.75E-01	1.90E+03
9.68E-01	3.70E+00	3.00E-01	2.07E+03
9.62E-01	4.05E+00	3.28E-01	2.26E+03
9.55E-01	4.43E+00	3.59E-01	2.47E+03
9.42E-01	4.83E+00	3.91E-01	2.69E+03
9.28E-01	5.28E+00	4.27E-01	2.94E+03

8.68E-01	5.78E+00	4.68E-01	3.23E+03
8.27E-01	6.32E+00	5.11E-01	3.53E+03
7.71E-01	6.90E+00	5.59E-01	3.85E+03
7.30E-01	7.55E+00	6.11E-01	4.22E+03
6.73E-01	8.26E+00	6.68E-01	4.61E+03
6.34E-01	9.04E+00	7.32E-01	5.04E+03
5.96E-01	9.89E+00	8.00E-01	5.52E+03
5.67E-01	1.08E+01	8.74E-01	6.02E+03
5.34E-01	1.19E+01	9.63E-01	6.64E+03
5.13E-01	1.29E+01	1.04E+00	7.19E+03
4.91E-01	1.42E+01	1.15E+00	7.92E+03
4.71E-01	1.55E+01	1.25E+00	8.64E+03
4.55E-01	1.69E+01	1.37E+00	9.42E+03
4.38E-01	1.85E+01	1.50E+00	1.03E+04
4.21E-01	2.03E+01	1.64E+00	1.13E+04
4.05E-01	2.22E+01	1.79E+00	1.24E+04
3.89E-01	2.43E+01	1.97E+00	1.36E+04
3.75E-01	2.66E+01	2.15E+00	1.48E+04
3.60E-01	2.90E+01	2.35E+00	1.62E+04
3.50E-01	3.17E+01	2.56E+00	1.77E+04
3.42E-01	3.42E+01	2.76E+00	1.91E+04
3.35E-01	3.80E+01	3.08E+00	2.12E+04
3.25E-01	4.14E+01	3.35E+00	2.31E+04
3.13E-01	4.53E+01	3.66E+00	2.53E+04
3.02E-01	4.88E+01	3.95E+00	2.72E+04
2.92E-01	5.43E+01	4.40E+00	3.03E+04
2.82E-01	5.92E+01	4.79E+00	3.31E+04
2.71E-01	6.45E+01	5.22E+00	3.60E+04
2.61E-01	7.08E+01	5.73E+00	3.95E+04
2.52E-01	7.80E+01	6.31E+00	4.35E+04
2.43E-01	8.48E+01	6.86E+00	4.73E+04
2.34E-01	9.32E+01	7.54E+00	5.20E+04
2.26E-01	1.01E+02	8.17E+00	5.63E+04
2.17E-01	1.11E+02	8.97E+00	6.18E+04
2.10E-01	1.21E+02	9.79E+00	6.75E+04
2.02E-01	1.34E+02	1.08E+01	7.46E+04
1.95E-01	1.45E+02	1.18E+01	8.11E+04
1.88E-01	1.59E+02	1.29E+01	8.89E+04
1.81E-01	1.74E+02	1.41E+01	9.70E+04
1.75E-01	1.91E+02	1.54E+01	1.06E+05
1.69E-01	2.08E+02	1.68E+01	1.16E+05
1.63E-01	2.28E+02	1.85E+01	1.27E+05
1.57E-01	2.50E+02	2.02E+01	1.39E+05
1.52E-01	2.73E+02	2.21E+01	1.52E+05
1.47E-01	3.00E+02	2.43E+01	1.67E+05
1.42E-01	3.27E+02	2.65E+01	1.83E+05
1.37E-01	3.59E+02	2.90E+01	2.00E+05
1.32E-01	3.92E+02	3.17E+01	2.19E+05
1.28E-01	4.30E+02	3.48E+01	2.40E+05
1.24E-01	4.69E+02	3.79E+01	2.62E+05
1.20E-01	5.13E+02	4.15E+01	2.86E+05
1.16E-01	5.61E+02	4.54E+01	3.13E+05
1.12E-01	6.14E+02	4.97E+01	3.43E+05

1.09E-01	6.72E+02	5.44E+01	3.75E+05
1.05E-01	7.36E+02	5.95E+01	4.11E+05
1.01E-01	8.05E+02	6.51E+01	4.49E+05
9.76E-02	8.79E+02	7.11E+01	4.90E+05
9.39E-02	9.63E+02	7.79E+01	5.37E+05
9.09E-02	1.05E+03	8.49E+01	5.85E+05
8.74E-02	1.15E+03	9.30E+01	6.41E+05
8.41E-02	1.26E+03	1.02E+02	7.03E+05
8.09E-02	1.38E+03	1.12E+02	7.70E+05
7.78E-02	1.51E+03	1.22E+02	8.41E+05
7.48E-02	1.65E+03	1.33E+02	9.19E+05
7.18E-02	1.81E+03	1.46E+02	1.01E+06
6.87E-02	1.98E+03	1.60E+02	1.10E+06
6.59E-02	2.16E+03	1.75E+02	1.20E+06
6.28E-02	2.37E+03	1.92E+02	1.32E+06
6.00E-02	2.59E+03	2.10E+02	1.45E+06
5.72E-02	2.83E+03	2.29E+02	1.58E+06
5.41E-02	3.10E+03	2.51E+02	1.73E+06
5.18E-02	3.39E+03	2.74E+02	1.89E+06
4.91E-02	3.71E+03	3.00E+02	2.07E+06
4.67E-02	4.06E+03	3.28E+02	2.26E+06
4.48E-02	4.44E+03	3.59E+02	2.48E+06
4.26E-02	4.85E+03	3.92E+02	2.70E+06
4.07E-02	5.31E+03	4.30E+02	2.96E+06
3.87E-02	5.81E+03	4.70E+02	3.24E+06
3.70E-02	6.36E+03	5.14E+02	3.55E+06
3.54E-02	6.95E+03	5.62E+02	3.88E+06
3.37E-02	7.61E+03	6.16E+02	4.24E+06
3.22E-02	8.32E+03	6.73E+02	4.64E+06
3.09E-02	9.10E+03	7.36E+02	5.08E+06
2.94E-02	9.96E+03	8.06E+02	5.56E+06
2.83E-02	1.09E+04	8.82E+02	6.08E+06
2.67E-02	1.19E+04	9.63E+02	6.64E+06
2.57E-02	1.30E+04	1.05E+03	7.25E+06
2.41E-02	1.43E+04	1.16E+03	7.98E+06
2.26E-02	1.56E+04	1.26E+03	8.70E+06
2.17E-02	1.71E+04	1.38E+03	9.54E+06
2.13E-02	1.87E+04	1.51E+03	1.04E+07
1.96E-02	2.04E+04	1.65E+03	1.14E+07
1.80E-02	2.23E+04	1.80E+03	1.24E+07
1.70E-02	2.44E+04	1.97E+03	1.36E+07
1.54E-02	2.67E+04	2.16E+03	1.49E+07
1.39E-02	2.93E+04	2.37E+03	1.63E+07
1.24E-02	3.20E+04	2.59E+03	1.79E+07
1.09E-02	3.50E+04	2.83E+03	1.95E+07
9.13E-03	3.83E+04	3.10E+03	2.14E+07
7.83E-03	4.19E+04	3.39E+03	2.34E+07
6.31E-03	4.58E+04	3.71E+03	2.56E+07
4.57E-03	5.01E+04	4.05E+03	2.79E+07
2.61E-03	5.48E+04	4.43E+03	3.06E+07
0	5.95E+04	4.81E+03	3.32E+07

Similar to the uncertainties associated with selecting a set of representative relative permeability curves, the available data on capillary pressure also pose significant challenges in selecting a consistent set. One of the first challenges is that the capillary pressure and relative permeability data have all been collected from different samples. In other words, there is no core sample for which both measured capillary pressure and relative permeability data exist. If such data were to exist, we could have easily selected the core sample with both sets (i.e., capillary pressure and relative permeability) of data on the basis of consistency. Not having such data requires that we need to carefully interpret the various data to arrive at defensible choices for relative permeability and capillary pressure functions.

Even though capillary pressure data obtained from the Princeton core samples (PC-34, PC-41, and PC-44) all appear to be of good quality, we set them aside based on the fact that they have been collected from a different location. (All the other rock properties are based on cores collected from the NYSTA Tandem Lot Well #1 – so why use the Princeton core for capillary pressure?) We exclude samples 2-6R, 2-10R, and 2-15R because they are from much shallower depths. Also, capillary pressure data from core sample 2-20R are excluded because this core has been collected at a depth almost 200 ft above the core sample which has been used for generating relative permeability curves. Of the remaining three core samples (2-24R, 2-31R, and 2-38R), we further analyze the last two because the capillary pressure data from these two samples together provide an envelope within which the rest of the capillary pressure data are located.

The capillary pressure data from the core samples 2-31R and 2-38R are fitted as a function of liquid saturation using the van Genuchten capillary pressure-saturation relationship as given in Equation A1.8. Figure 2.10 shows the measured and fitted capillary pressure curves for these two samples. The parameters obtained after fitting for these two samples are listed in Table 2.6. Note that, as we have already selected the van Genuchten parameter m as 0.38 while generating the relative permeability of the liquid-phase, we initiated the curve-fitting process for capillary pressure with $m = 0.38$. Based on the parameters obtained after fitting the capillary pressure data, it seems reasonable to retain $m = 0.38$. As for the initial capillary entry pressure, we select the value for core sample 2-38R, even though this sample is not near the sample from which the relative permeability data have been collected. We justify this by noting that the capillary suction observed in core sample 2-38R is significantly larger than that in 2-31R. Thus, if we select sample 2-38R as the representative function for capillary suction in our flow and transport model, we are implementing a stronger rock affinity for the wetting phase (i.e., water). In other words, the liquid phase in our model formation will be less mobile, and the supercritical "gas" phase will be more mobile, relatively speaking, than if we chose the capillary suction of 2-31R.

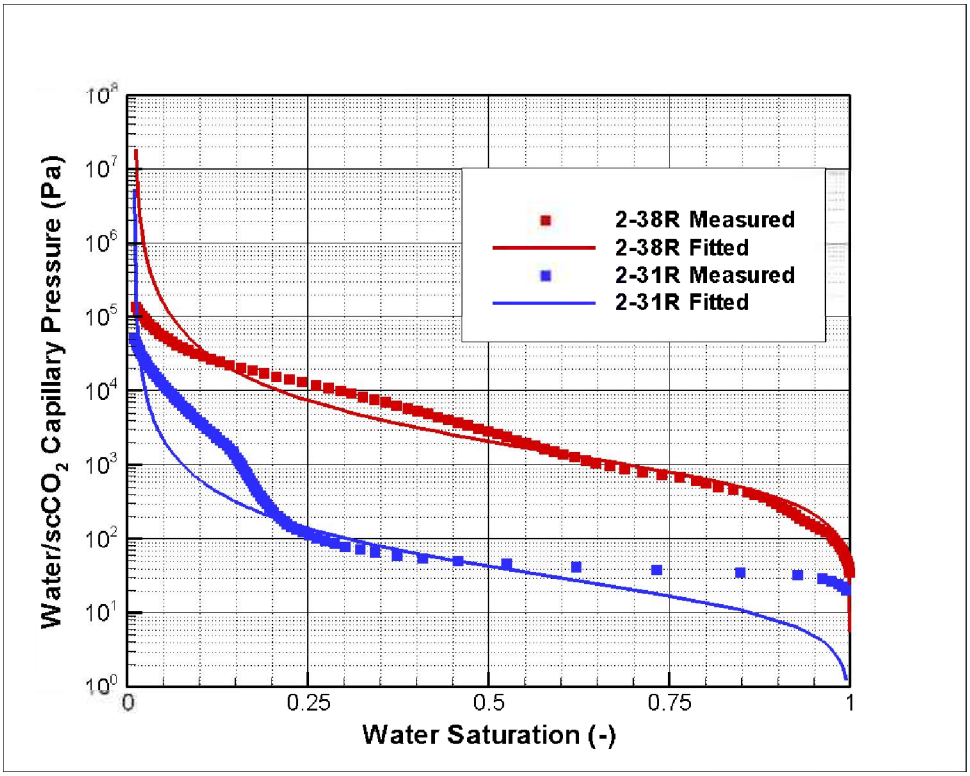

Figure 2.10. Measured and fitted capillary pressure curves for two core samples (2-31R and 2-38R) from the NYSTA Tandem Lot Well #1.

Table 2.6. Best-fit parameters obtained after fitting the measured water-$scCO_2$ capillary pressure data of Sample 2-31R and Sample 2-38R to van Genuchten capillary pressure function (Equation A1.8).

Core Sample	van Genuchten *m*	α (Pa^{-1})	S_{lr}	S_{ls}
2-31R	0.397	6×10^{-2}	0.01	0.999
2-38R	0.376	4×10^{-4}	0.01	0.999

Note that recent experimental investigations (e.g., Tokunaga et al., 2013) have questioned the validity of using scaling relationships, such as the ones being used here, for estimating the capillary pressure of water-$scCO_2$ systems from mercury injection pressures. Introduction of $scCO_2$ into reservoirs often results in geochemical reactions (Kaszuba et al., 2003; Kharaka et al., 2006; Shao et al., 2011), including wettability alterations (Bikkina, 2011; Chiquet et al., 2007a,b; Dickson et al., 2006; Jung and Wan, 2012; Kim et al., 2012). Because of these geochemical and wettability alterations, capillary behavior of water-$scCO_2$ systems cannot be reliably estimated from scaling-based extrapolation of nonreactive immiscible fluids such as air, certain oils, or mercury. Additionally, reservoir conditions span a very broad range of *P*, *T*, and chemistry; over which large variations occur in $scCO_2$ density (Span and Wagner, 1996), water-$scCO_2$ interfacial tension (Bachu and Bennion, 2009; Chalbaud et al., 2010; Li et al., 2012), and wettability of mineral surfaces (Bikkina, 2011; Chiquet et al., 2007a,b; Jung and Wan, 2012; Wang et al., 2013), all of which can have significant consequences on capillary behavior in water/$scCO_2$ systems,

rendering simple scaling-based estimations questionable. However, for the preliminary predictive modeling addressed in this report, scaling-based relationships may be adequate. Appropriate capillary pressure curves can be incorporated in future model revisions when more site-specific data become available. Finally, the base case property set for flow modeling is summarized in Table 2.7.

Table 2.7. Base-case hydrologic-property-set data, which have been developed based on available core data from the NYSTA Tandem Lot Well #1. Most of the flow and reactive transport simulations in this report were performed using this base-case property set. Additional sensitivity simulations were also performed (to bracket the range of acceptable values) by changing the values of the key parameters from this base-case property-value set, one parameter at a time.

No.	Property	Value	Comments
1.	Porosity	0.130	See discussion in Section 2.5.1
2.	Grain density	2650 kg/m^3	See discussion in Section 2.5.1
3.	Permeability	50 mD	See discussion in Section 2.5.1
4.	VG λ	0.38	See discussion in Section 2.5.2
5.	Residual liquid saturation for relative permeability	0.01	See discussion in Section 2.5.2
6.	Residual gas saturation	0.05	See discussion in Section 2.5.2
7.	VG α	4.0×10^{-4} Pa^{-1}	See discussion in Section 2.5.3

2.6 Boundary and Initial Conditions

For all the flow simulations presented in this report, the top and bottom boundaries are assumed to be no-flow boundaries. These no-flow boundaries were imposed to simulate a sealing caprock at the top and a low-permeability formation at the base of the target injection formation. While these assumptions may be justified, it should be noted that caprocks are seldom fully sealing, and may provide leakage pathways, which present a potential risk to underground sources of drinking water (USDW). Leakage through the caprock can also have significant consequences for the fate of the CO_2 within the injection formation. However, these risks and uncertainties were not investigated in this work, whose main focus was, as stated previously, preliminary reactive transport modeling. The two lateral boundaries along the *y* direction were also assumed to be no-flow boundaries. The side boundaries, however, were open to flow.

Before starting an actual injection simulation, a proxy simulation was performed to generate the initial pressure distribution within the model domain. This was accomplished by closing all six boundaries of the 3D model domain, and applying a constant hydrostatic pressure at the center of the top of the domain. The applied pressure at the top of the model domain was 15.024 MPa, which is equivalent to the pressure of water at a depth of 1,524 m (5,000 ft) corresponding to the depth of the Stockton Formation. This proxy simulation was carried out for an extended period (in excess of 10,000 years) such that a true steady-state condition (as far as pressure distribution within the model domain is concerned) was realized. The eventual pressure distribution from this proxy simulation was used as the initial pressure condition

for the injection simulation. To make the side boundaries open for injection simulations, the gridblocks at these locations were assigned very large volumes (such that their conditions would remain unaffected by any fluxes into or out of the gridblocks) but were given the pressure values generated from the proxy simulation. Isothermal conditions were assumed for all the simulations. In other words, temperature variation within the storage formation and any thermal effects resulting from injection of CO_2 into water were ignored. A temperature of 53.8°C was assigned to each gridblock within the model domain. This assumed temperature value is consistent with generally accepted geothermal gradient data. For most of the flow simulations, it is assumed that water has no dissolved salt. However, a few sensitivity simulations were also performed with water having different levels of salt content. These will be discussed separately later (see Section 2.8.2).

For all simulations, it is assumed that 1 MMt of CO_2 is injected per year for a period of 30 years. Because symmetry allows us to use only half the model domain, the model has 15 MMt of CO_2 injected over 30 years at a constant rate of 0.5 MMt/year. While the model domain is 150 m deep vertically, injection takes place in the bottom 60 m of the injection formation. A special treatment was needed for numerically implementing CO_2 injection in the gridblocks while trying to estimate pressure buildup. We provided a large vertical permeability value (relative to the formation permeability) for all the gridblocks representing the injection nodes and introduced all of the CO_2 in one single gridblock representing the top of the injection formation. This allowed the injected CO_2 to be distributed among the different injection nodes according to their prevailing densities (which in turn depend on pressure under isothermal conditions).

2.7 Base-Case Simulation Results

The base-case simulations were performed with the base-case hydrological property set as provided in Table 2.7. Unless stated otherwise, here and elsewhere in this section, each simulation consists of a 30-year injection period, which is followed by a 70-year observation (or rest) period, resulting in 100 years of total simulation time. Pressure evolution within the model domain during injection can be assessed from Figure 2.11, which shows, the contours of pressure at 1 (Figure 2.11(a)), 10 (Figure 2.11(b)), and 30 years (Figure 2.11(c)), respectively. Apart from a small region around the injection location, pressure rise elsewhere within the model domain is less than 1.5 MPa or 10% of the initial pressure (~15 MPa). Note that, because the primary objective of these basin-scale simulations is to assess the CO_2 plume migration distance with passage of time, they do not provide an accurate estimate of the pressure increase close to the injection location. Separate simulations were performed to assess pressure buildup near the injection location, and these will be discussed later in this section (see Section 2.8.2).

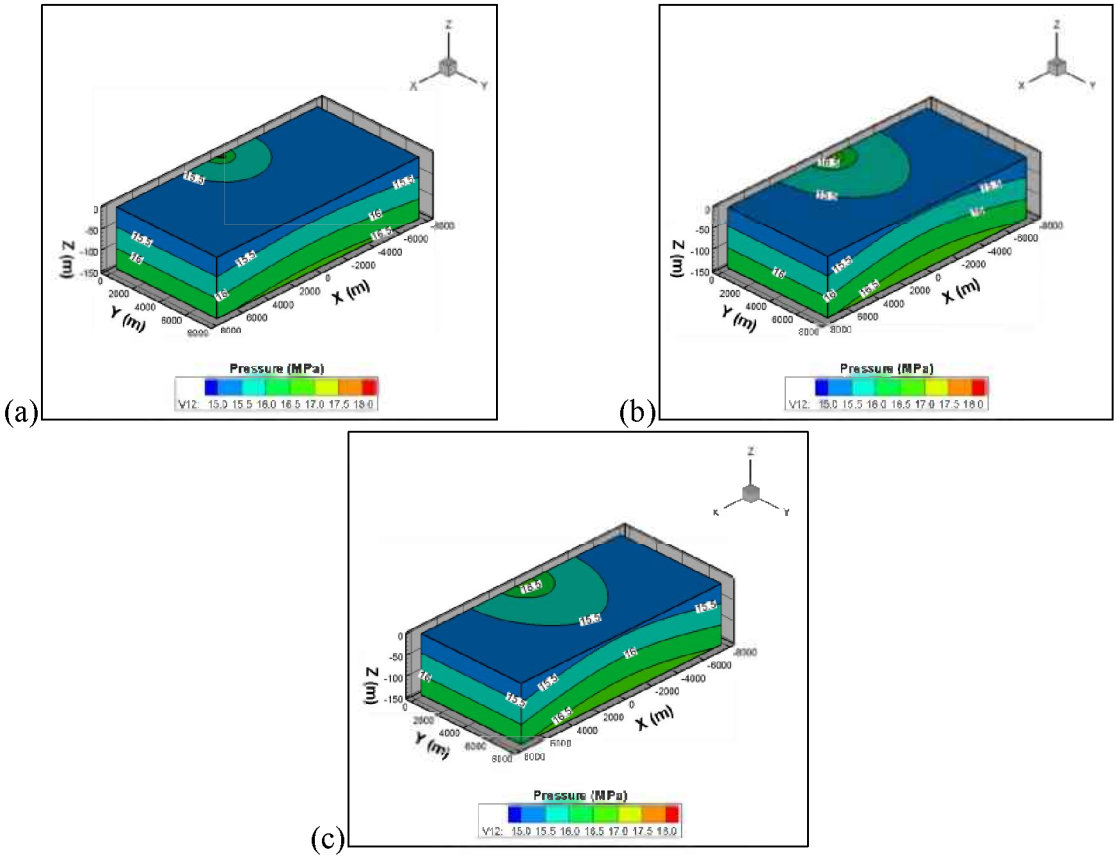

Figure 2.11. Contours of pressure in the 3D model domain obtained with the base-case hydrological property set (see Table 2.7) at (a) 1, (b) 10, and (c) 30 years.

Simulated locations of the CO_2 plume can be seen in Figure 2.12, where the contours of CO_2 saturation in the 3D model domain are shown at 5 (Figure 2.12(a)), 10 (Figure 2.12(b)), and 30 (Figure 2.12(c)) years. Note that these are saturations corresponding to the free CO_2 (supercritical) phase, hereafter referred to as gas saturations. The funnel-like shape of the plume in 3D space is caused by forces of buoyancy, which preferentially drive the injected CO_2 towards the top of the injection formation. Once CO_2 reaches the top of the formation, it flows outward along the top boundary. Consequently, the horizontal migration distance is more along the upper part of the formation compared to other deeper locations. Similar patterns of migration are also observed during the observation or rest period after injection ceases. As can be seen in Figure 2.13, where gas saturations are shown at 50 (Figure 2.13(a)) and 100 (Figure 2.13(b)) years, the funnel-like plume shape persists even after injection ceases. During this rest period, supercritical CO_2 continues to move outward along the top part of the formation, and below it, continuous dissolution of CO_2 in the aqueous phase causes the funnel to reduce in size towards the bottom of the formation.

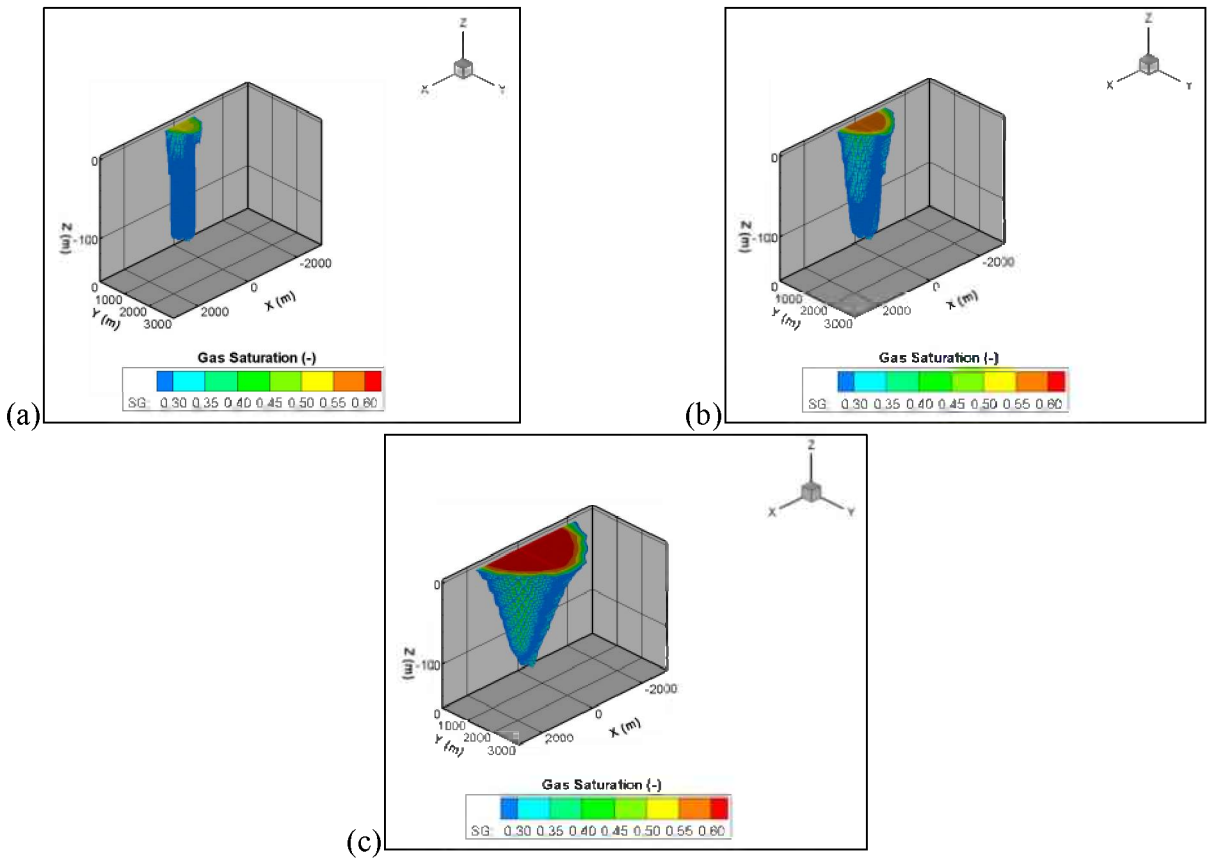

Figure 2.12. Contours of free-phase or gas CO_2 saturation in the 3D model domain obtained with the base-case hydrological property set (see Table 2.7) at (a) 5, (b) 10, and (c) 30 years.

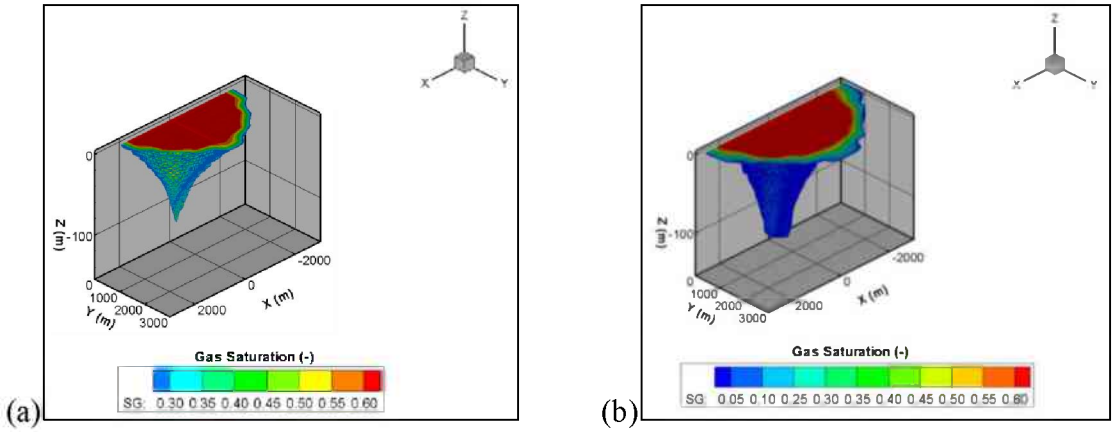

Figure 2.13. Contours of gas saturation in the 3D model domain during the rest period. These results have been obtained with the base-case hydrological property set (see Table 2.7). Contours of gas saturation are shown at (a) 50 and (b) 100 years.

While a general assessment about the shape of the injected plume can be made from Figure 2.12 and 2.13, they do not provide a clear picture of the plume migration distance. For this purpose, instead of showing

the CO_2 saturations in 3D space, we show the contours of CO_2 saturation in a 2D vertical (x-z) slice at y = 0 (i.e., the vertical slice containing the injection gridblock) in Figure 2.14. Figure 2.14(a) shows these contours at 30 (i.e., end of injection period), and Figure 2.14(b) shows the same at 100 years (i.e., end of observation period). Note that at the end of the injection period, the plume has moved to a location of ~2,000 m along the top edge of the formation. The migration distances, as expected, are much smaller as one moves towards the bottom of the formation. At 100 years, the plume is predicted to reach a distance of ~3,000 m at the top, while dissolution has caused free-phase CO_2 to disappear below a certain depth (~60 m from the top).

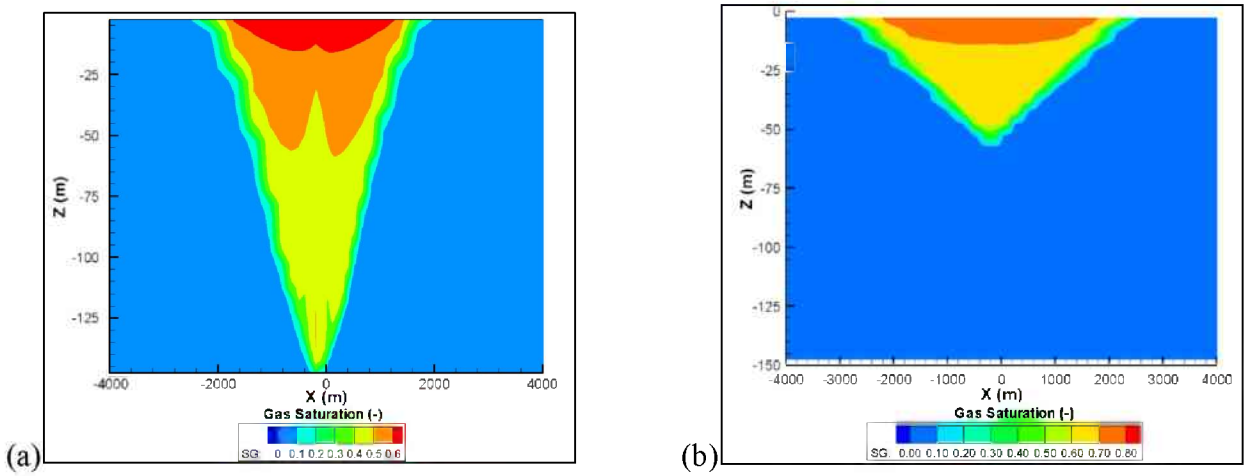

Figure 2.14. Contours of gas saturation in a 2D vertical slice at y = 0, containing the injection gridblocks. Saturation contours are shown at (a) 30 years and (b) 100 years. Simulation results were obtained with the base-case hydrological property set (see Table 2.7).

The role of dissolution in controlling plume shape and migration extent is further illustrated in Figure 2.15, which shows the partitioning of the injected CO_2 between gas and aqueous phases at different times. In Figure 2.15, the green line shows the fraction of the injected CO_2 that remains as a separate gas phase, which continues to increase through the injection period (30 years) and then declines steadily in the observation (or rest) period. The fraction of CO_2 in the aqueous phase, on the other hand, increases slowly during both the injection and observation periods. Dissolution of CO_2 in water is controlled by temperature, pressure, and salinity conditions of the resident brine. It should be noted that in these simulations, the decreased solubility of CO_2 in water caused by dissolved salts is not taken into account, but would likely have only a small effect given the presumed moderate salinity of the brine (see Section 3). During the injection period, more CO_2 is injected than can be dissolved in water, resulting in a rapid increase in the proportion of CO_2 (as fraction of total CO_2 mass) entering the gas phase. After injection stops, some of the excess gas-phase CO_2 slowly dissolves (the rate of which depends on solubility conditions) in the aqueous phase, causing a slow rise in the aqueous phase mass fraction. Note that, in Figure 2.15, phase partitioning has been presented as the ratio of mass of CO_2 in a particular phase (gas or aqueous) at a certain time and the total cumulative mass of CO_2 injected through that time. The total injected mass of CO_2 is shown by the red line, which reaches the value of 1.0 at the end of the injection

period. Because no other CO_2 is injected after the injection period ends, total CO_2 mass fraction remains at 1.0 through the observation period.

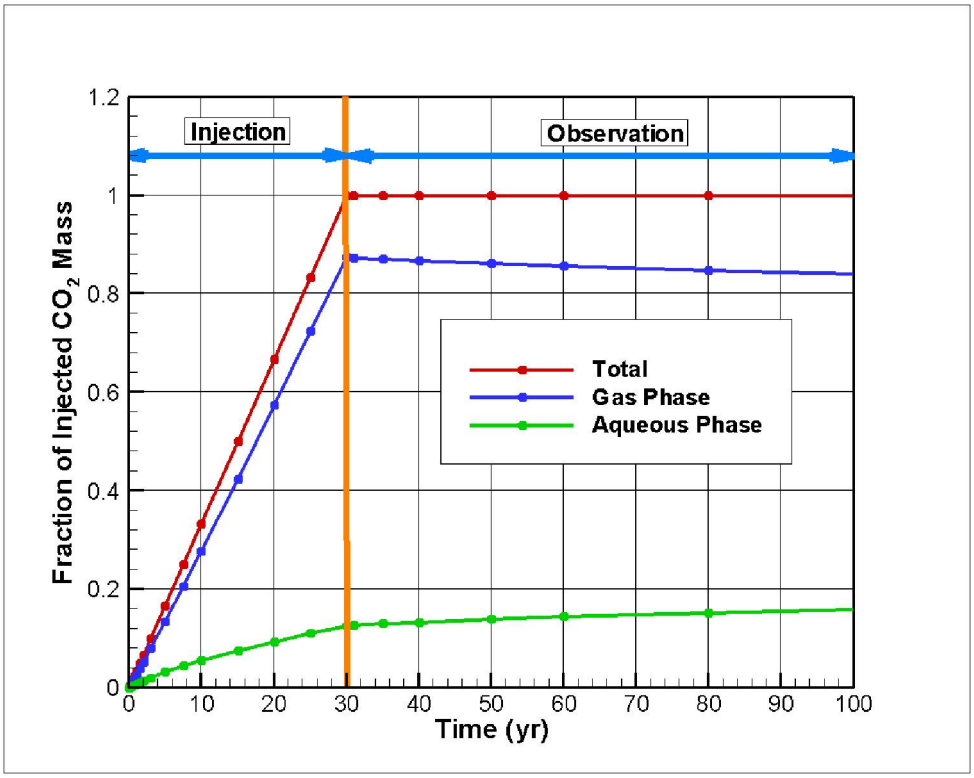

Figure 2.15. Partitioning of the injected CO_2 between the gas ("gaseous") (line in blue) and aqueous (line in green) phases as a function of time. The red line represents the total injected mass of CO_2 as a function of time. Results are shown as a fraction of the total injected mass. Injection happens over 30 years, at which time the total injected mass fraction becomes 1.0, and remains constant at that value during the rest period. These results were obtained with the base-case hydrological property set (see Table 2.7).

Note also that the CO_2 distribution in DSA also depends on factors such as the relative permeability and capillary characteristics of the fluid phases and the rocks. Because our objective is to conservatively estimate the migration distance, which in this case should be interpreted as creating situations that will favor gas-phase migration, the base-case hydrological property set, including its small gas residual saturation (0.05), has been selected to favor the migration of the gas-phase CO_2 plume. This likely resulted in an overprediction of gas-phase CO_2 mobility. Finally, these base-case simulations suggest that, at the end of the injection period, nearly 88% of the injected CO_2 will remain in the gas phase, which declines to a value of 83% at the end of the 100-year observation period. We will soon show how these predictions change with changes in the input parameter values.

One of the factors that is expected to have a strong influence on plume migration distance is the formation dip. To illustrate the influence on plume shape and migration distance, we repeated the base-case simulations with a dipping formation. We did this by tilting the model domain by a certain angle and keeping everything else identical to the base-case simulations including the hydrological properties. As discussed in Section 1.2, the Stockton Formation has a significant dip, estimated to be between 8° to 14°.

We selected a tilt of 8° as an average value for the entire model domain. Note that, before starting the actual injection simulations, similar to the base-case simulations with a flat (i.e., not tilted) numerical mesh, proxy steady-state simulations were also performed with this new tilted numerical mesh to generate the initial hydrostatic pressure distribution. Because the model domain is tilted by such a large angle, the bottom of the model domain reaches a depth of ~2,714 m (below ground surface), whereas the top of the model domain is situated at a depth of ~475 m (below ground surface). In comparison, the flat numerical mesh is situated between 1,524 m (top) and 1,675 m (bottom) below the ground surface. As a result, the initial hydrostatic pressures at the bottom of the tilted mesh are considerably larger. Conversely, the initial hydrostatic pressures at the top of the tilted mesh are significantly smaller (compared to those with the flat mesh). In other words, there is a significant variation in pressure within the model domain, dictated by gravity. Pressure within this tilted model domain at end of injection is shown in Figure 2.16.

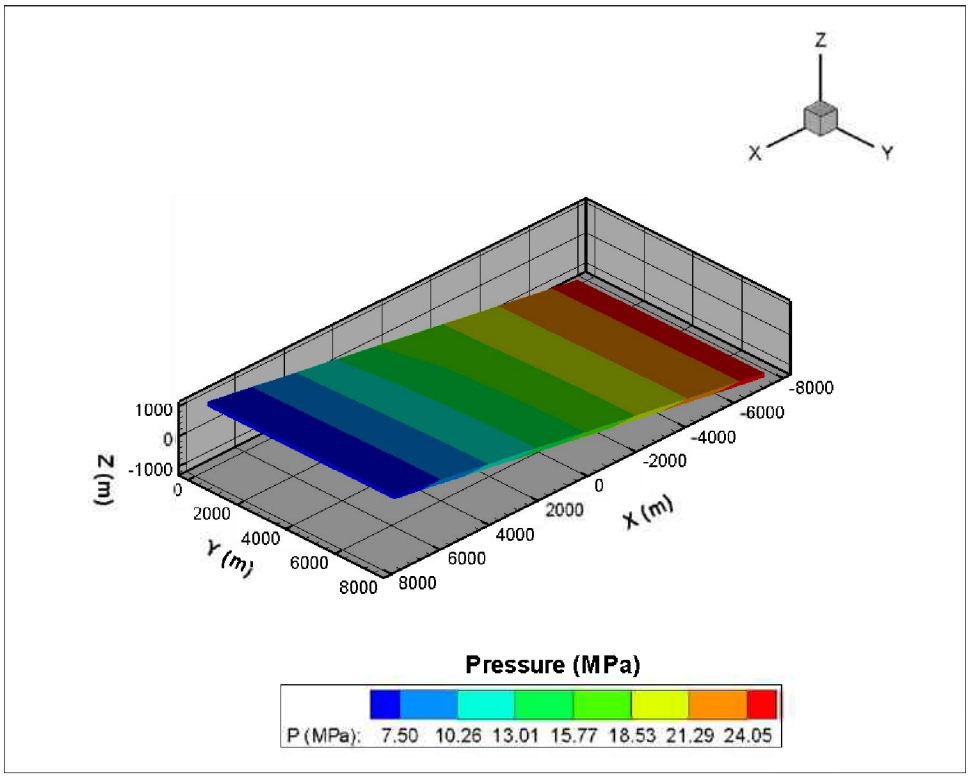

Figure 2.16. Contours pf pressure at 30 years (end of injection) in the 3D model domain, when it is tilted by an angle of 8°. Results are obtained with the base-case hydrological property set.

When CO_2 is injected in a tilted formation, buoyancy forces drive it preferentially upgradient. This can be seen in Figure 2.17, where we show the contours of gas-phase CO_2 saturation at 5, and 30 years. Because of the different scales involved in x and z directions, the plume shape in the vertical direction is not clearly visible in this figure; however, it gives a clear picture of the plume's transient spread at the top of the formation. The plume migration patterns during the observation period can be seen in Figure 2.18, which shows the saturation contours at 100 years. A clearer picture emerges when we show the contours of gas-saturation from this simulation in a vertical cross section at $y = 0$ m in Figure 2.19. While the plot in Figure 2.19(a) shows the results at 30 years, Figure 2.19(b) is for 100 years. Both these figures show

that the injected plume has moved significantly more in the up-gradient direction. At 30 years, the plume has moved upwards of 3,000 m in the up-gradient direction compared to only about 1,600 m in the down-gradient direction. These migration distances are different from those (~2,000 m) obtained from the simulations with the flat model domain. The plume shape is also significantly different from the symmetric funnel-type shape observed with the flat model domain. By 100 years, the injected plume has virtually become a layer floating on water at the top of the model domain, and migrating along with water.

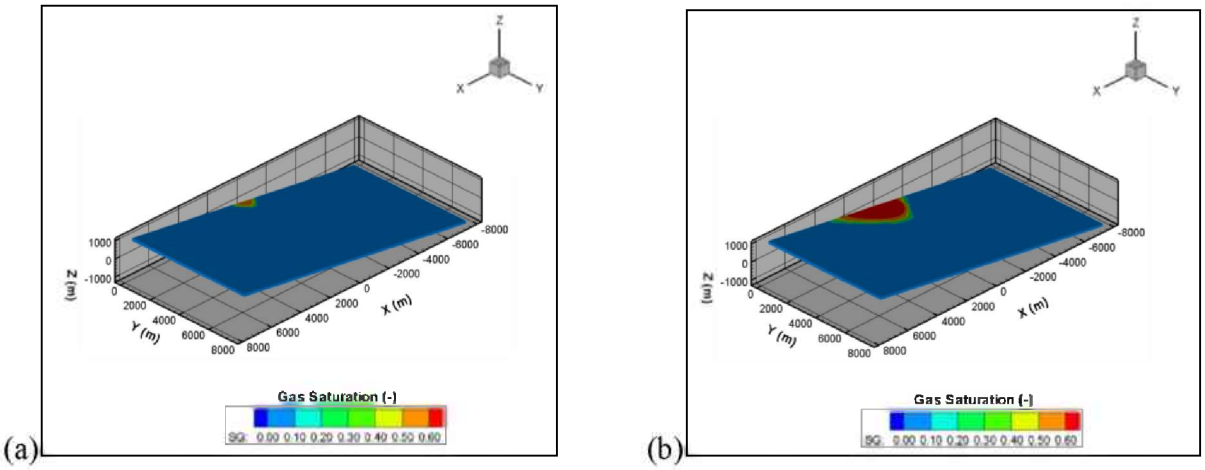

Figure 2.17. Transient migration of the injected CO_2 plume in the 3D model domain showing the impact of the angle of inclination on the front location. The model domain is tilted by an angle of 8°. Contours of gas saturation are shown at (a) 5 and (b) 30 years. Results were obtained with the base-case hydrological property set (see Table 2.7).

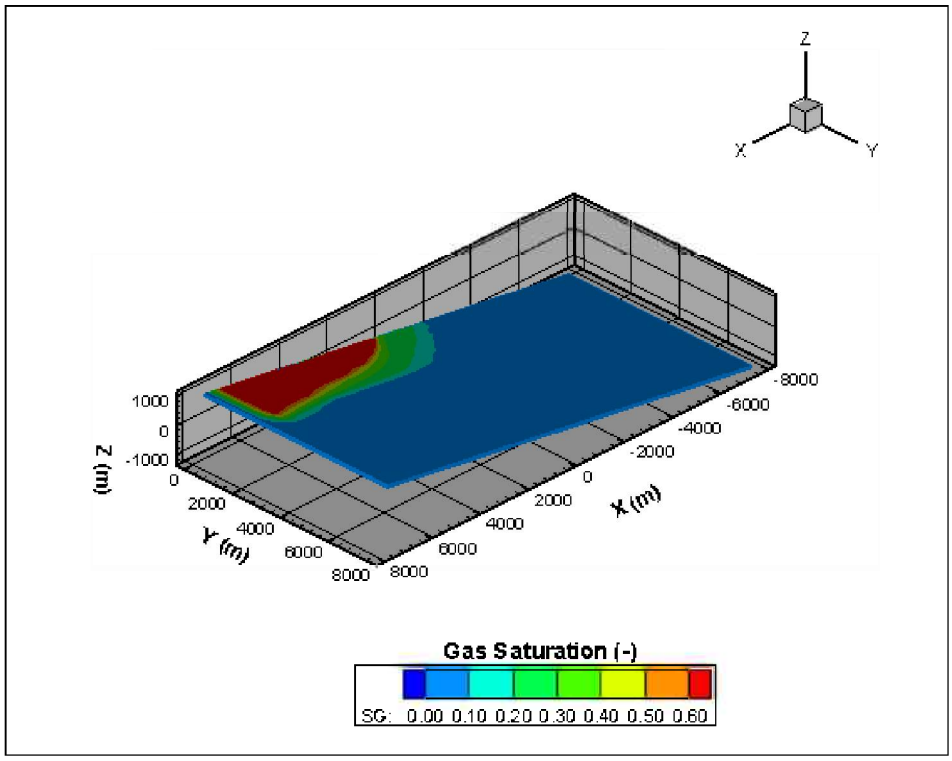

Figure 2.18. Contours of gas saturation at the end of the rest period (100 years) in the 3D model domain, when it is tilted by an angle of 8°. Base-case hydrological property set (Table 2.7) was used in these simulations.

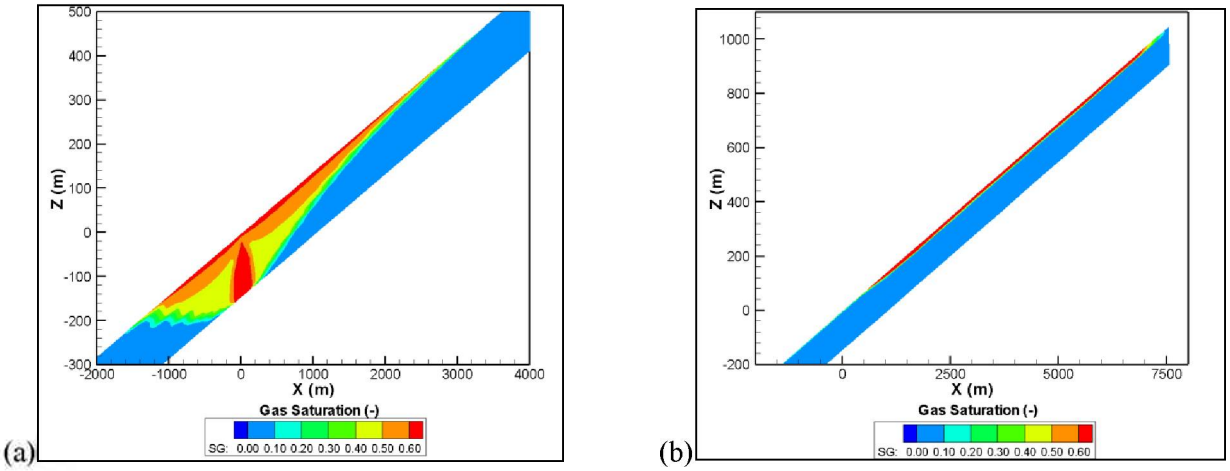

Figure 2.19. Contours of gas saturation in a 2D vertical slice at y = 0, containing the injection gridblocks. The model domain is tilted by an angle of 8°. Saturation contours are shown at (a) 30 years and (b) 100 years. Simulation results were obtained with the base-case hydrological property set (see Table 2.7). Note the differences in axes in the two plots of this figure.

These differences in plume migration behavior are reflected in how the injected CO_2 is partitioned between the gas and aqueous phases. This is shown in Figure 2.20, which is similar to Figure 2.15. In simulations with the flat model domain, it was predicted that almost 88% of the injected CO_2 will remain

as a separate phase at the end of injection, and no less than 83% would remain in the phase even after 100 years. Figure 2.20 presents a different scenario, where, even though it is predicted that a comparable CO_2 amount will remain in gas phase at end of the injection period, the fraction of total (gas phase + dissolved) CO_2 mass remaining in the gas phase declines rapidly during the rest period. So much so that, after about 90 years, more CO_2 remains in aqueous phase than as a free gas phase. By 100 years, it is predicted that only about 36% of the injected CO_2 will remain in gas phase, with the rest being dissolved in the formation brine. The only way to explain these predictions is as follows. Because the formation tilt causes the injected CO_2 to travel much longer distances in the up-gradient direction, the injected plume comes in contact with a significant amount of fresh water (or brine), which allows additional CO_2 to dissolve, diffuse, and mix in the formation brine. Consequently, there is a steady decline in the amount of CO_2 in the gas phase of the system, and a corresponding increase in the total amount of CO_2 dissolved in brine. These predictions thus point towards significant dissolution trapping over time.

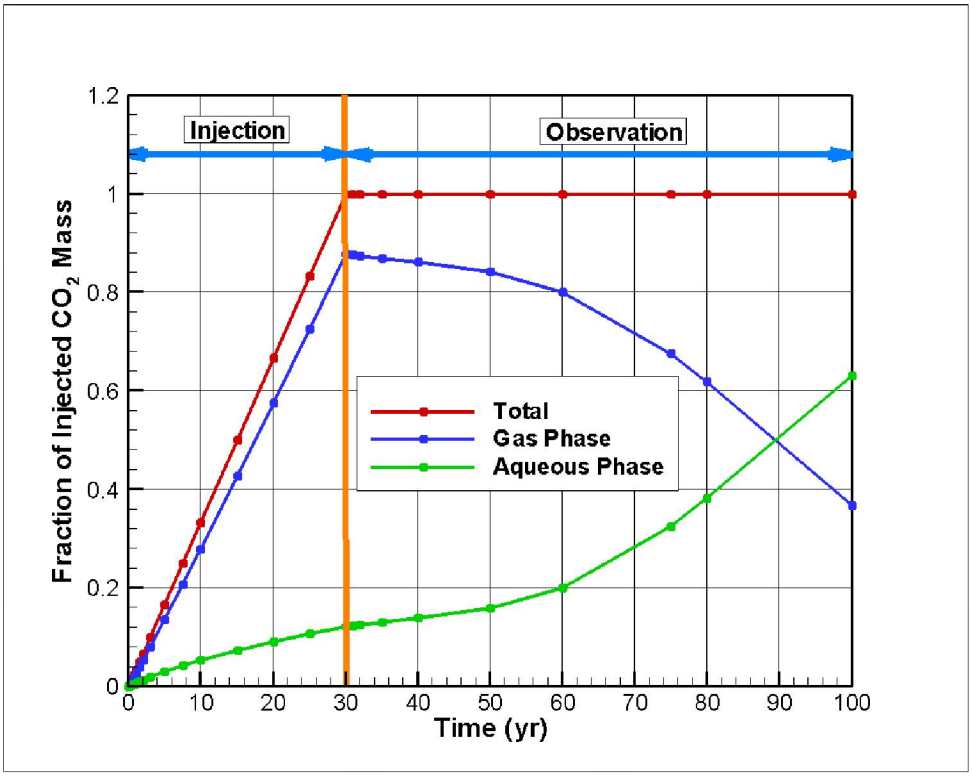

Figure 2.20. Same as Figure 2.15, however, these results are obtained by tilting the 3D model domain by an angle of 8°.

2.8 Sensitivity Study

In Section 2.5, we indicated that, because of the paucity of reliable site characterization data, considerable uncertainties existed with the base-case hydrological parameters selected for performing the flow and transport simulations. To assess the impact of these uncertain input parameters, and to bracket the range of predicted results, we performed a number of sensitivity simulations. The sensitivity simulations were carried out with three objectives: (1) to determine an acceptable value for the maximum distance that the

injected CO_2 plume can travel; such an estimation can be useful for assessing the areal footprint of the plume, if CO_2 were to be actually injected in DSA of the Newark Basin in the future; (2) to determine how changes in relevant input parameters affect the fate of the injected CO_2 plume; and (3) to determine the impact of uncertainties in model input parameters on pressure buildup near the injection location. The answer to this last question can be important in assessing injectivity (and or safe injection limits) while storing CO_2 at the Newark Basin. In the following, we seek answers to these questions through systematic sensitivity studies.

2.8.1 Migration Distance and Fate of Injected CO_2

The flow parameters that have the most influence on migration of the injected CO_2 plume are absolute permeability of the storage formation, permeability anisotropy, and the factors controlling relative permeability and capillary characteristics of the fluid-rock combination.

2.8.1.1 Permeability

Conservatism in the context of assessing uncertainty in plume migration distance dictates that we use a larger permeability for the storage formation. This is because using a permeability smaller than the base-case permeability value of 50 mD will obviously yield a smaller migration distance, which is not helpful while assessing the maximum plume migration distance. We thus carried out two sensitivity simulations to assess the impact of permeability on plume migration distance by using two different formation permeabilities, i.e., 100 and 500 mD. Increasing the permeabilities beyond 500 mD will increase the maximum migration distance even more; however, we do not feel it is necessary to investigate any larger permeability value. In other words, we feel it is unlikely that we will find a storage formation within the Newark Basin that will have permeabilities larger than 500 mD, while providing the needed storage volume to store large amounts of CO_2. Thus, we believe our choice for the range of permeability in these sensitivity studies is justified. Furthermore, because formation tilt causes the injected plume to move farther in a particular direction (i.e., upgradient), we performed these sensitivity simulations with the model domain tilted by an angle of 8°. Note that, after performing some preliminary simulations with 500 mD permeability, it was determined that the 16,000×16,000×150 m model domain was not adequate. We thus used the model 3D numerical mesh covering a model domain of 22,000×22,000×150 m 3D numerical mesh (see Section 2.4) for these sensitivity studies.

Figure 2.21 shows CO_2 saturation at 30 years in a vertical slice of the 3D model domain. This vertical slice is located at $y = 0$ and contains the injection blocks. While the plot in Figure 2.21(a) shows the saturation contours obtained with 100 mD, the plot in Figure 2.21(b) corresponds to formation permeability of 500 mD. As expected, the very large permeability of 500 mD in the latter simulation makes the plume move much longer along the top of the formation compared to the base case or the 100 mD simulation. The size of the funnel-shape plume around the injection location is also much smaller when the permeability is 500 mD compared to the 100 mD or base-case simulations. This is expected because the very large permeability of 500 mD drives the buoyant CO_2 plume along the top of the formation very rapidly. This can be more clearly seen in Figure 2.22, where we show the partitioning of the injected CO_2 mass between the gas and aqueous phases from three simulations with different permeabilities: base-case (which includes a formation permeability of 50 mD), 100 mD, and 500 mD.

Figure 2.22(a) shows the fraction of the injected CO_2 in the gas phase for these three permeabilities, and Figure 2.22(b) shows the same in the aqueous phase. For convenience, the total injected fraction line is retained in both the plots. Note that, as permeability is increased, more and more CO_2 is allowed to dissolve into the aqueous phase, and less and less CO_2 remains as a free gas phase. Larger permeability causes the injected CO_2 to move farther away from the injection location and come in contact with fresh water (or brine), resulting in more and more dissolution. Note also that, for large enough permeabilities (e.g., 500 mD), significant dissolution can take place even during the active injection period as shown by the declining gas-phase CO_2 mass fraction during this phase for the simulation with 500 mD permeability. In other words, for highly permeable formations, while it is true that the plume can move extreme distances along the top of the formation (which can have significant environmental impact), strong dissolution is also expected in such formations. However, it is not realistic to have a storage formation with permeabilities as large as 500 mD or even 100 mD.

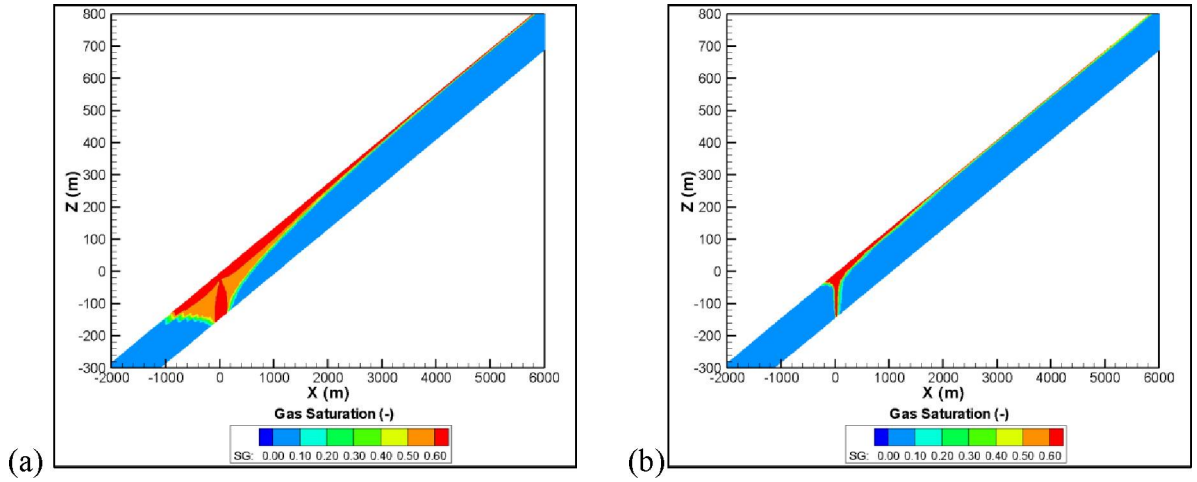

Figure 2.21. Impact of formation permeability on injected CO_2 plume. Simulated contours of gas saturation obtained with permeabilities of (a) 100 and (b) 500 mD are shown. The base-case permeability is 50 mD, results for which are shown in Figure 2.19. All other hydrological properties are identical to base-case hydrological property values.

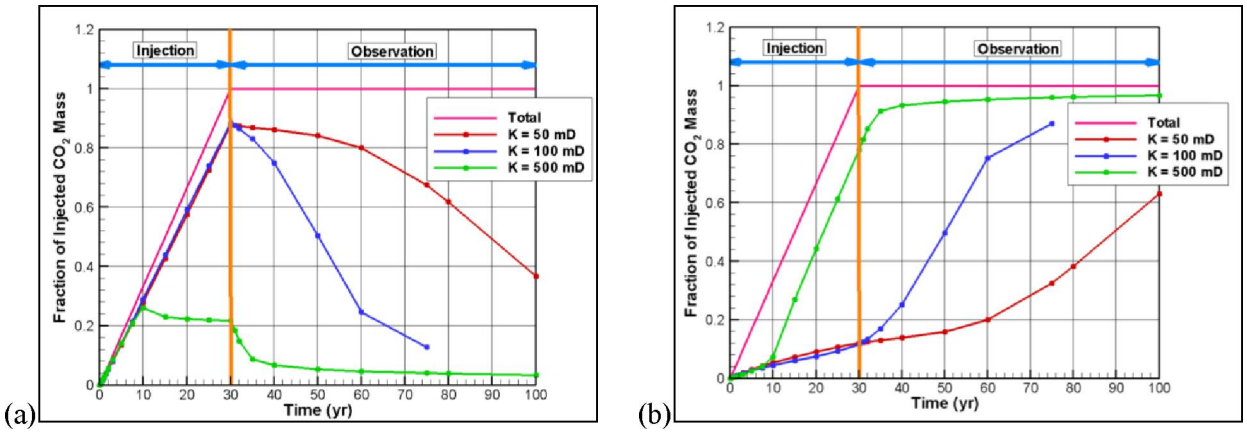

Figure 2.22. Fraction of injected CO_2 predicted to remain in the gas and aqueous phases for different values of formation permeability. For these simulations, except permeability, all other hydrological

properties are obtained from the base case hydrological property set (Table 2.7). (a) CO_2 predicted to remain in the gas phase, and (b) CO_2 predicted to remain in the aqueous phase.

2.8.1.2 Permeability Anisotropy

Most geological formations exhibit anisotropy in their rock properties, particularly permeability. In such formations, more specifically in deep sedimentary basins, vertical permeability is often significantly smaller than horizontal permeability. This anisotropy in formation permeability, as we will soon illustrate, exercise significant controls over plume shape and migration. While we have no convincing data establishing anisotropy in permeability for the formation core samples studied, for the purposes of this sensitivity study, we assume different values of the anisotropy ratio (a_v), which is defined as the ratio of vertical to horizontal permeability. For the base-case simulation, $a_v = 1.0$ (i.e., it was isotropic) because we assumed the same permeability value of 50 mD for vertical and horizontal directions. We performed sensitivity studies with three more values of the anisotropy ratio, i.e., $a_v = 0.5$, 0.2, and 0.1. In Figure 2.23(a), we show, as an example, the gas saturations at 30 years for the simulation with $a_v = 0.1$. Gas saturations from the same simulation but at 100 years are shown in Figure 2.23(b). These results should be compared with the base-case simulation results in Figure 2.19. Note that the smaller vertical permeability in Figure 2.23 has caused the plume to retain the funnel-like shape even at 100 years, which was completely unnoticeable in Figure 2.19, particularly at end of rest period. The partitioning of the injected CO_2 between the different phases from these sensitivity simulations are shown in Figure 2.24(a) (for gas phase) and Figure 2.24(b) (for aqueous phase). As the value of a_v decreased (i.e., the vertical permeability decreased), more and more CO_2 remained as a free gas phase because of reduced (buoyancy driven) upward migration of the injected plume.

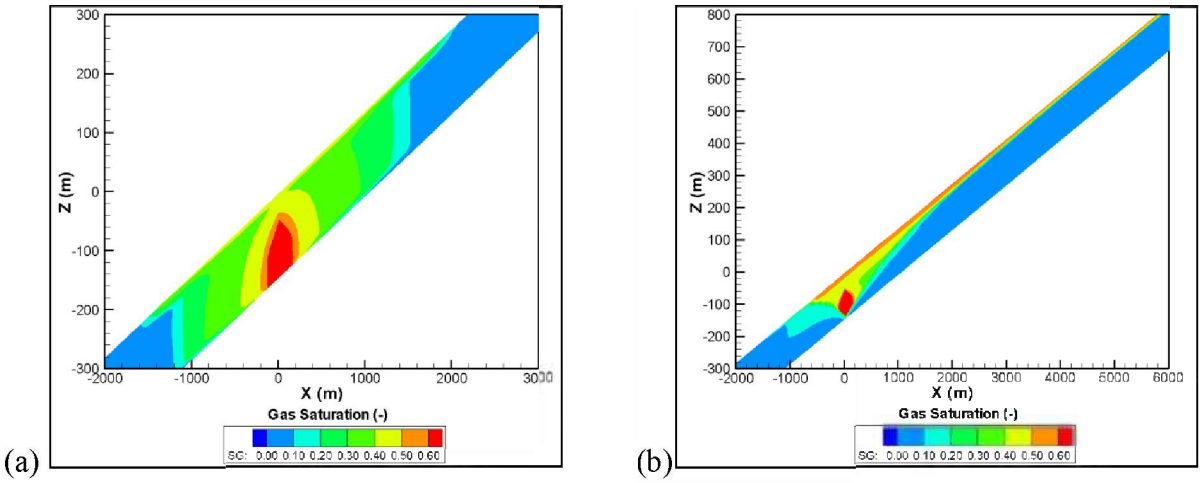

Figure 2.23. Contours of gas saturation at (a) 30 and (b) 100 years when the anisotropy ratio $a_v = 0.1$.

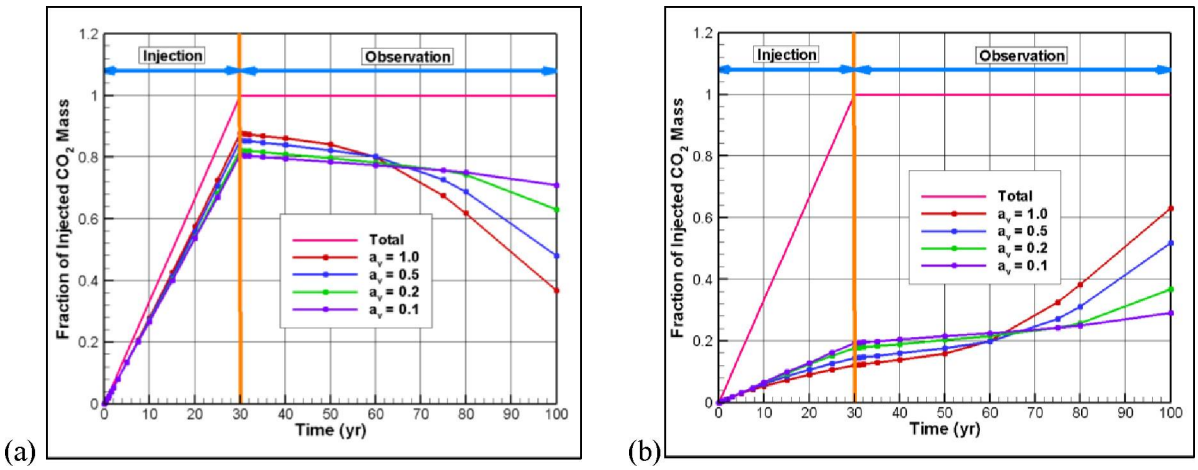

Figure 2.24. Fraction of injected CO_2 predicted to remain as free gas phase as opposed to a dissolved phase for different values of anisotropy ratio a_v. For these simulations, except vertical permeability, all other hydrological properties are obtained from the base-case hydrological property set (Table 2.7). (a) Fraction of injected CO_2 predicted to remain as a free gas phase, and (b) Fraction of injected CO_2 predicted to dissolve in the aqueous phase.

2.8.1.3 Residual Gas Saturation

Residual "gas" saturation or S_{gr} is thegas saturation at which the free-phase CO_2 becomes immobile. If a large value of S_{gr} is used in simulations, it implies that a relatively large amount of CO_2 will remain trapped as an immobile phase within the pore space of the storage formation. In other words, the imbibing water phase during the rest period will be unable to displace this trapped gas. A smaller value of S_{gr} has the converse effect on the mobility of CO_2 as a free gas phase. Having a reliable estimate of S_{gr} is therefore critical for correctly predicting the gas-phase relative permeability, which in turn controls its migration velocity. Based on the analysis of available relative permeability measurement data (Section 2.5.2), we used $S_{gr} = 0.05$ in the base case simulations. This S_{gr} value appears to be on the smaller side based on our knowledge of its literature value. To quantify its impact on the plume shape and velocity (and hence migration distance), we performed additional sensitivity simulations with $S_{gr} = 0.1$ and $S_{gr} = 0.2$. The fraction of CO_2 in the gas and aqueous phases as a function of time for different values of S_{gr} is shown in Figures 2.25(a) and 2.25(b), respectively. When $S_{gr} = 0.05$ (i.e., as in base-case simulations), only about 36% of the injected CO_2 is predicted to remain in the gas phase after 100 years. However, gas-phase CO_2 increases to 44% for $S_{gr} = 0.10$, and further increases to 66% when $S_{gr} = 0.20$. The corresponding impact on CO_2 plume location can be seen in Figures 2.26 for 30 and 100 years. While the plume shape is somewhat similar to the base-case results at the end of injection period (compare Figure 2.26 with Figure 2.19), these sensitivity simulations with different S_{gr} predict that a large bank of gas-phase CO_2, whose size depends on the value of S_{gr}, is left at the back end of the

moving plume. Based on these sensitivity analyses, it is clear that S_{gr} plays a significant role in defining the storage characteristics of a target injection formation, and an accurate estimation of this parameter is needed for correctly predicting the fate of the injected CO_2, particularly for better prediction of residual trapping. Note that, in these simulations, capillary hysteresis, which accounts for different capillary behavior during drainage (i.e., displacement of the brine phase by CO_2 during injection) and imbibition (displacement of the injected CO_2 by brine at end of injection) have not been included. Capillary hysteresis can have a noticeable impact on plume shape and migration velocity (Doughty, 2007).

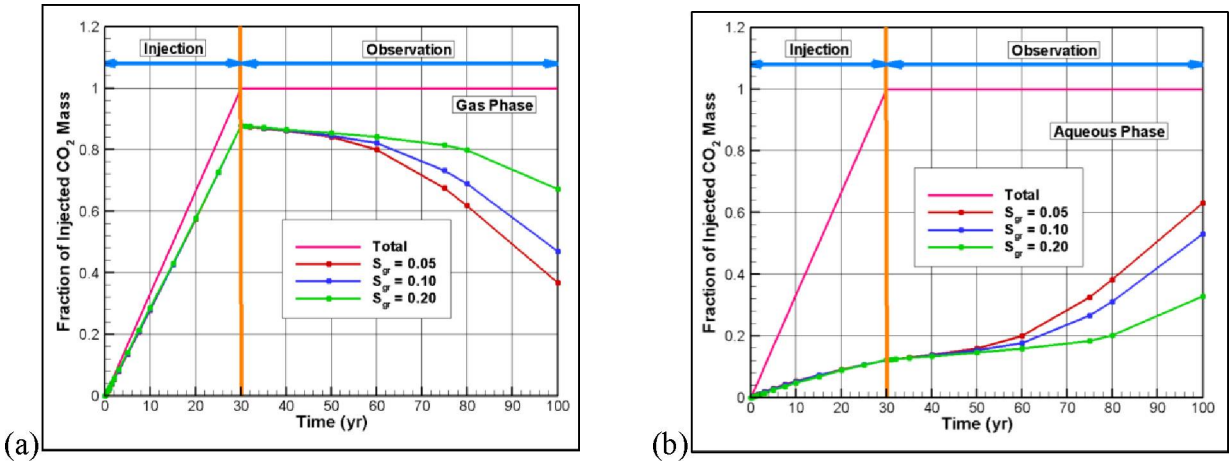

Figure 2.25. Fraction of injected CO_2 predicted to remain as free gas phase as opposed to dissolved in the aqueous phase for different values of residual gas saturation S_{gr}. For these simulations, except S_{gr}, all other hydrological properties are obtained from the base-case hydrological property set (Table 2.7), (a) Fraction of injected CO_2 predicted to remain as free gas phase, and (b) Fraction of injected CO_2 predicted to dissolve in the aqueous phase.

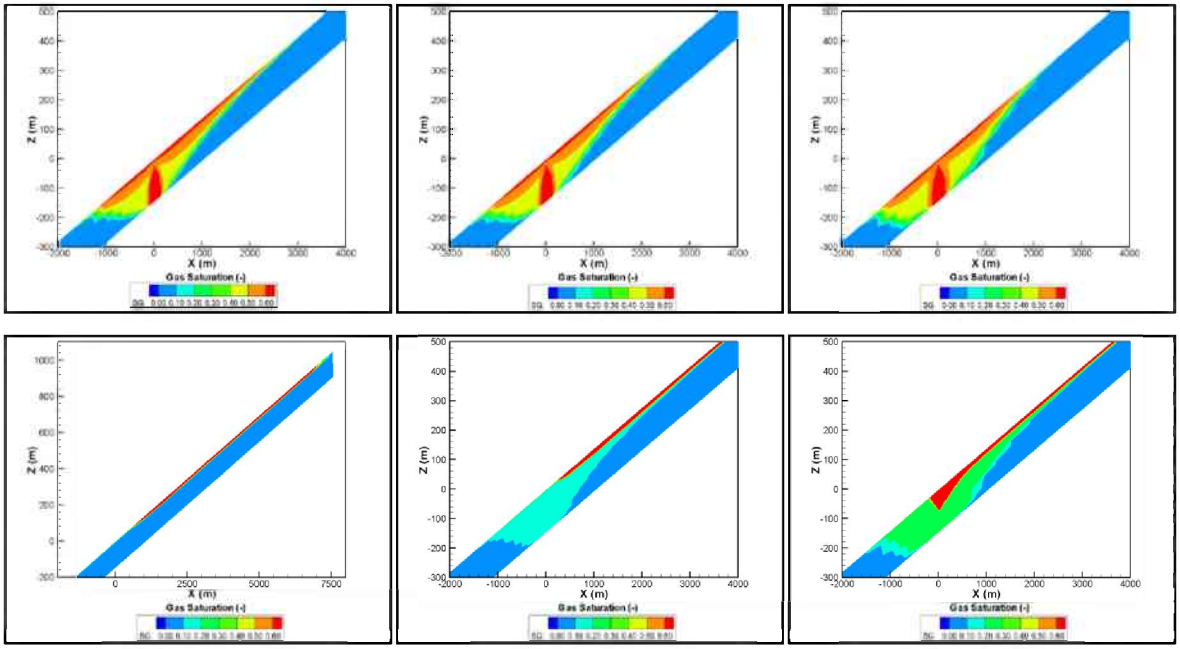

Figure 2.26. Contours of free-phase gas saturation at 30 (top three graphs) and 100 years (bottom three graphs) for $S_{gr} = 0.05$ (left-hand-side), 0.10 (middle), and 0.20 (right-hand-side).

2.8.1.4 Irreducible Water Saturation

Irreducible water saturation or S_{wr} is the water saturation below which the aqueous phase loses its mobility. It plays a similar role for water relative permeability as does S_{gr} for gas relative permeability. A large value of S_{wr} causes the aqueous phase to be less mobile. It also signifies a larger affinity of the rock towards the aqueous phase. As a result, a larger portion of the pore space in the injection formation remains occupied by the aqueous phase, which causes the gas phase to migrate farther and get dissolved in the aqueous phase. The overall result is that less of the injected CO_2 remains in the gas phase when S_{wr} is large compared to when it is smaller. This is confirmed by our sensitivity simulations, where in addition to the base-case simulation with $S_{wr} = 0.01$, we performed two other simulations with $S_{wr} = 0.10$ and 0.20. The fraction of free-phase CO_2 as a function of time for different values of S_{wr} is shown in Figure 2.27(a), and the fraction of CO_2 dissolved in the aqueous phase is shown in Figure 2.27(b). Note that, for the base-case simulation where we used $S_{wr} = 0.01$, it is predicted that about 36% of the injected CO_2 will remain as a free phase, this percentage drops to 20% when $S_{wr} = 0.20$. Similar to S_{gr}, reliable estimates of S_{wr} are also needed for accurately predicting the fate of the injected CO_2. The corresponding gas saturation contours are shown in Figure 2.28.

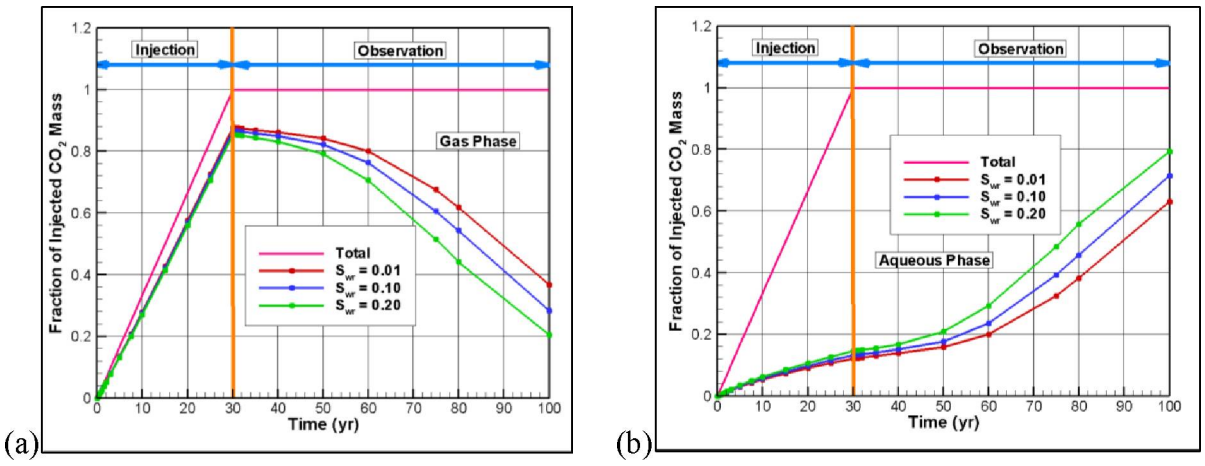

Figure 2.27. Fraction of injected CO_2 predicted to remain as a free gas phase as opposed to dissolved in the aqueous phase for different values of residual gas saturation, S_{wr}. For these simulations, except S_{wr}, all other hydrological properties are obtained from the base-case hydrological property set (Table 2.7), (a) Fraction of injected CO_2 predicted to remain as a free gas phase, and (b) Fraction of injected CO_2 predicted to dissolve in the aqueous phase.

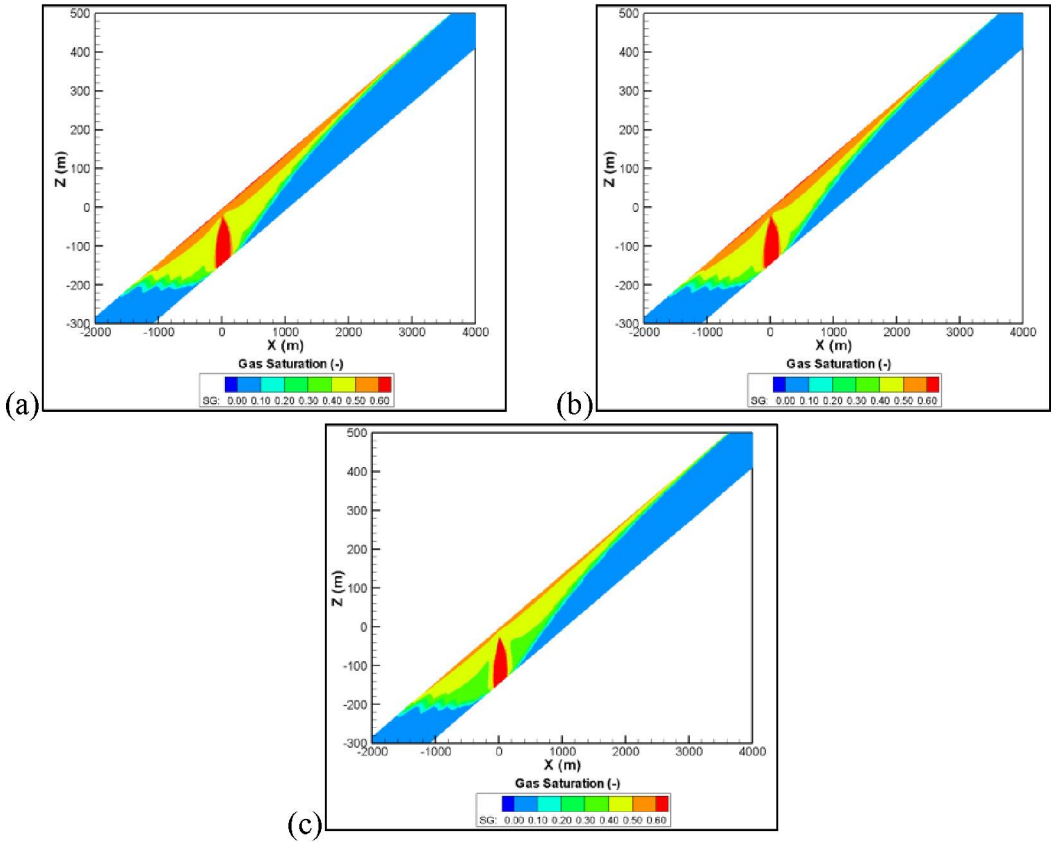

Figure 2.28. Contours of gas-phase CO_2 saturation at 30 years for $S_{wr} = 0.01$ (a), 0.10 (b), and 0.20 (c).

2.8.1.5 Capillary Pressure

In Section 2.5.3, we analyzed all the mercury injection pressure data that were measured in core samples from Newark Basin area, and presented the equivalent capillary pressure-versus-saturation curves in Figure 2.9. We then selected the capillary-pressure curve corresponding to core sample 2-38R for inclusion in the base-case hydrological property set, based on the logic that it provided the upper curve of an envelope covering all the capillary pressure data. In other words, we selected the curve corresponding to maximum capillary pressure for a given saturation value. Our justification was that a stronger capillary pressure would make the free CO_2 phase more mobile, which would be "conservative" while assessing the maximum plume distance. At that time, we also commented that we would perform a sensitivity study with the smallest capillary pressure (which corresponds to Sample 2-31R) to bracket the entire range of capillary data. The reciprocal capillary entry pressure corresponding to data from Sample 2-31R, as noted in Table 2.6, is 6×10^{-2} Pa^{-1}, i.e., approximately two orders of magnitude larger than that for Sample 2-38R. We thus performed a sensitivity simulation with $\alpha = 4\times10^{-2}\,Pa^{-1}$ (exactly two orders of magnitude larger than base case α). We also performed another sensitivity simulation with an intermediate value of this parameter, i.e. $\alpha = 4\times10^{-3}\,Pa^{-1}$.

The fraction of injected CO_2 mass remaining as a free gas phase as a function of time for three different values of α is shown in Figure 2.29. It appears that increasing α, even by two orders of magnitude, has no appreciable impact on the distribution of free-phase CO_2. In other words, CO_2 plume characteristics appear to be relatively insensitive to even a large change in α. One possible explanation for this observation could be that the base-case α value was already large (i.e., small capillary suction); increasing it even more did not change the model prediction in an appreciable way. The other explanation can be that an increase in α is generally associated with a corresponding increase in permeability through Leverett scaling effects, which would have made the plume more mobile (relative to the base-case situation), and a larger fraction of the injected CO_2 would have entered the aqueous phase (i.e., less would have remained in gas phase, compared to the base-case situation). However, because these Leverett scaling effects were not included in the flow simulations, we do not see a noticeable change in model predictions resulting from a change in α value. Further investigation of Leverett scaling effects and more reliable capillary pressure data are thus recommended.

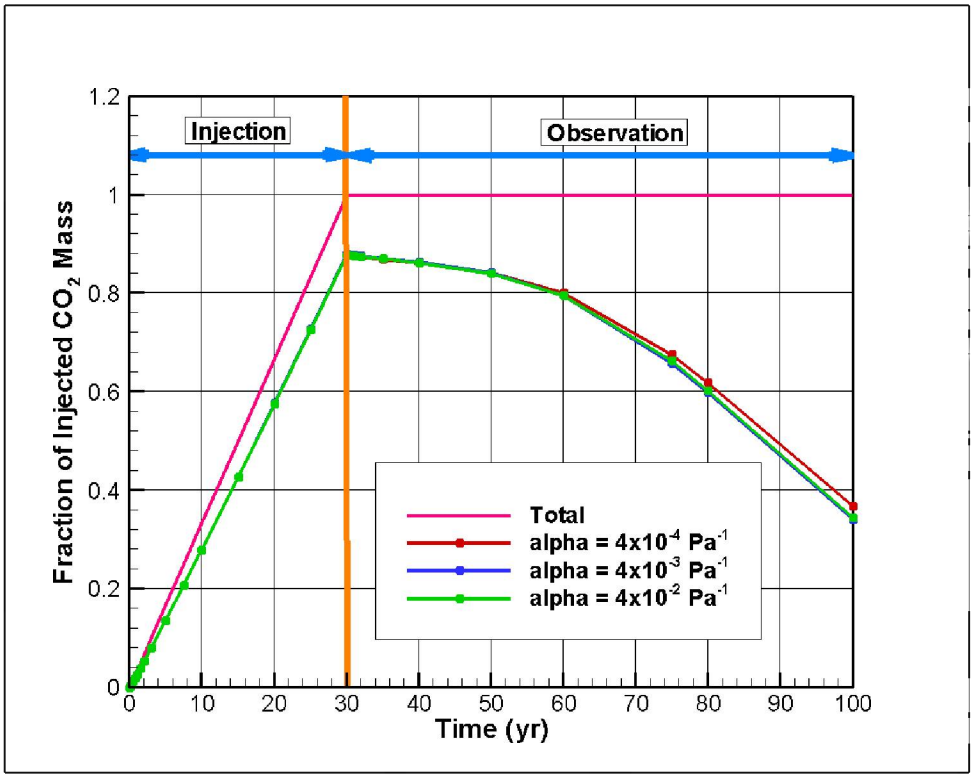

Figure 2.29. Fraction of injected CO_2 predicted to remain as a free gas phase for different values of reciprocal capillary entry pressure, α. For these simulations, except α, all other hydrological properties are obtained from the base case hydrological property set (Table 2.7).

2.8.2 Pressure Evolution

After investigating the parameter sensitivity of plume migration and the fate of the injected CO_2, we turn our focus on pressure evolution. The amount of CO_2 that can be injected or at what rate it can be injected is often dictated by the safe injection limit. The safe injection limit basically specifies the maximum allowable injection rate such that the resulting pressure buildup from injection will not exceed the fracture pressure. If this limit is exceeded, injection can cause significant damage to the storage formation including excessive fracturing, which brings with it enhanced risks of leakage. It is therefore helpful to have an idea about the expected pressure buildup from a planned injection scenario, such that injection would have no adverse impact on the storage formation.

In the context of GCS, there are several factors that affect pressure buildup from a particular injection scenario. The permeability of the formation, its thickness, relative permeabilities of the CO_2 and brine phases (Mathias et al., 2013), their mutual solubilities (Burton et al., 2008; Azizi and Cinar, 2013), and reservoir heterogeneities can all significantly influence the pressure-buildup characteristics of a storage formation. In addition, injection of CO_2 can cause the resident brine to evaporate, resulting in salt precipitation and permeability reduction near the injection well, thereby significantly impacting pressure behavior near the injection well (e.g., Pruess and Müller, 2009). At injection rates generally associated with GCS, it is also likely that inertial effects and non-Darcy flow effects will influence pressure buildup (e.g., Mijic et al., 2014). In summary, the combination of permeability and relative permeability, salt precipitation, gas compressibility, and inertial and thermal effects is likely to control the evolution of

pressure. In the following, we investigate the impact of two factors on pressure buildup in the storage formation, namely permeability and salt precipitation.

In Section 2.4, we stated that for assessing pressure buildup near the injection location, it is more appropriate to use a radial symmetric model domain instead of a 3D basin-scale model domain. This is because pressure buildup mostly happens within a small area around the injection location over a short time period, and the flow is mostly radial within that small period. Thus, all the simulations related to investigating pressure behavior were carried out with the radial mesh discussed in Section 2.4, and CO_2 injection was implemented following the procedure discussed in Section 2.6. To recapitulate, CO_2 was introduced into one single gridblcok at the top of the injection interval (i.e., this gridblock was located 90 m below the top of the injection formation), and all gridblocks representing the injection interval (gridblocks between -90 m and -150 m) were given a large vertical permeability. The injected CO_2 was then distributed among the different gridblocks in the injection interval according to the prevailing pressure and corresponding density.

In Figure 2.30, we show the temporal evolution of pressure within the injection interval at three different locations—top of the injection interval, middle of the injection interval, and bottom of the injection interval. The pressure-evolution patterns at these locations are similar, except for the small but constant difference in pressure values at any given time. This small but constant difference results from slightly different initial pressure at these three locations, resulting from their different vertical locations and corresponding difference in initial hydrostatic pressure. This figure confirms that numerical implementation of CO_2 injection did not cause unwarranted pressure buildup within the gridblocks representing the injection zone (note that we did not actually model the flow and transport behavior within the injection well).

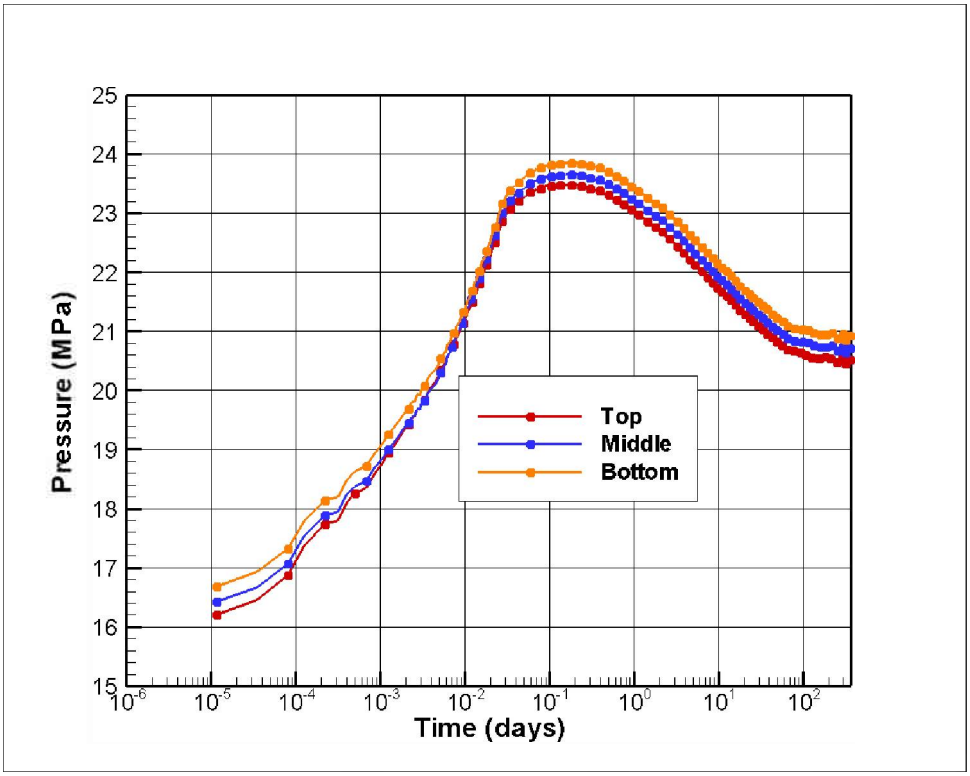

Figure 2.30. Simulated pressure versus time plots at three different locations within the injection zone. These results were obtained with the base-case hydrological preoperty set given in Table 2.7.

2.8.2.1 Permeability

The base-case hydrological property set for the storage formation included a permeability value of 50 mD. Numerical simulations predict that, when 1 MMt/year of CO_2 is hypothetically injected into the Newark Basin with 50 mD permeability, pressure may increase up to ~23 MPa within 2.5 hours of commencement of injection, after which time pressure gradually declines. This represents a buildup of pressure by an amount of ~8 MPa from the initial pressure. Note that these pressure-increase values are average values over a 2 m radial distance. Actual pressure increase closer to the injection well can be larger. Additionally, other factors such as presence of skin and salt precipitation may also increase pressure buildup.

Because our objective is to assess the maximum extent of pressure buildup resulting from CO_2 injection, a sensitivity simulation with permeability larger than 50 mD is not needed, because pressure increase will be, anyway, smaller than 8 MPa with a larger permeability. We thus performed sensitivity simulations with three reduced values of permeability. When the formation permeability is 25 mD (a reduction by a factor of two from the base case permeability value), pressure continues to rise for the first ~2 hours after which it begins to decline. The maximum pressure reached in this simulation is ~32 MPa, an increase of 17 MPa from the initial pressure of 15 MPa. When permeability is further reduced to 10 mD (a reduction factor of 5), maximum predicted pressure is 52 MPa at about 2.5 hours. Reducing permeability to 5 mD caused pressure to build up rapidly, and it reached the value of 60 MPa within a few minutes. This

simulation could not be completed (and the maximum pressure rise could not be estimated) because the ECO2N fluid property module of the TOUGHREACT simulator has a maximum pressure limit of 60 MPa. These results are summarized in Figure 2.31, which shows pressure as a function of time for different values of formation permeability. From these simulations, it can be stated that CO_2 can be safely injected into the considered geologic formation, if the formation permeability is indeed in the vicinity of 50 mD. However, injection may cause excessive pressure buildup if the formation permeability is anywhere close to 5 mD.

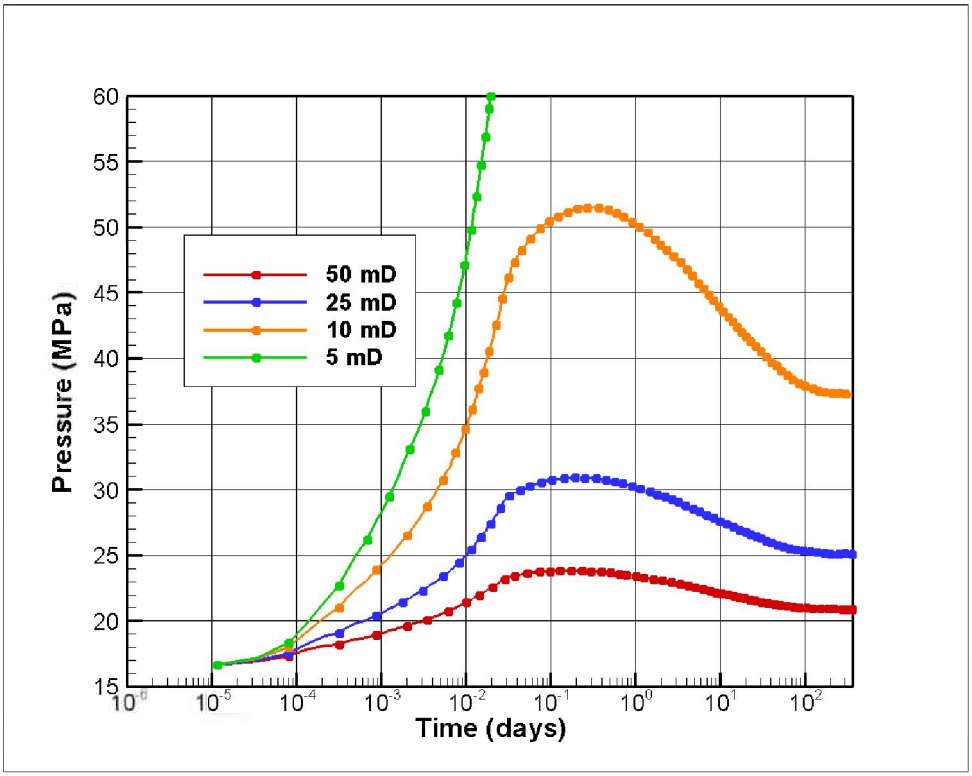

Figure 2.31. Simulated pressure versus time plots at the bottom of the injection zone for different values of formation permeability.

2.8.2.2 Salt Precipitation Amount

A factor that can influence the pressure-buildup behavior near an injection well is salt precipitation, caused by evaporation of the formation water into the injected CO_2. To assess the amount of salt precipitation during injection, we performed sensitivity simulations with resident brines containing different amount of dissolved salt. Note that the base-case simulations presented in Section 2.7 assumed there was no dissolved salts in the aqueous phase. On the other hand, the reactive transport simulations in Section 6 are performed with a dissolved salt content of 20,000 mg/lit (see Section 3.2.1 for the rationale behind this choice). We thus performed simulations with dissolved salt content of 0, 20,000, 50,000, and 100,000 mg/lit to bracket a range of typical salinities Figure 2.32 shows the zone of solid salt precipitation at end of injection (30 years), when the resident brine had 20,000 (Figure 2.32(a)) and

100,000 mg/lit dissolved salt. These results suggest that salt precipitation is small, and such small amounts of precipitation would not be expected to significantly impact injection and pressure.

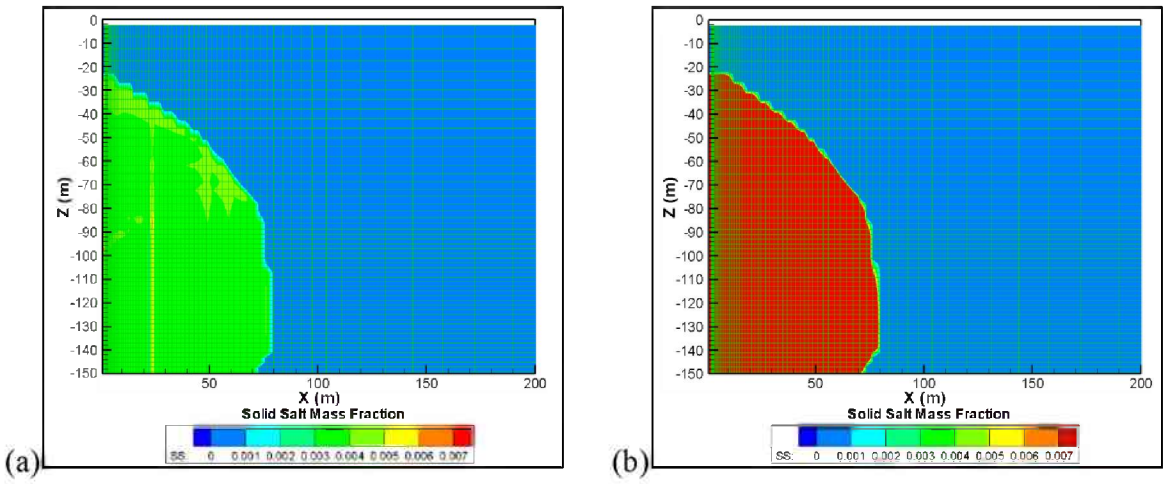

Figure 2.32. Simulated contours of solid salt volume fraction of pore space at 30 years (end of injection) for two different dissolved salt contents, (a) 20,000 mg/lit and (b) 100,000 mg/lit.

3. SITE-SPECIFIC GEOCHEMICAL DATA

In this section we discuss the mineralogy of sandstone samples selected for laboratory experiments. Because samples of deep brines in the Newark Basin could not be obtained, we also present an approach and modeling analyses to reconstruct the chemical composition of deep brine using various data, including analyses of shallow brines in the area of interest. These data feed directly into the laboratory experiments presented in Section 4 and modeling analyses presented in Section 5 and Section 6.

3.1 Formation Mineralogy

The formation mineralogy adopted for experimental and numerical studies presented in this report was based on X-Ray Diffraction (XRD) analyses of sandstone samples collected in well Tandem Lot Well #1 (Table 3.1). A review of the well geologic and geophysical logs by the research team reveals the presence of the Palisade Sill (an igneous feature, Figure 1.1) at a depth of about 5,000 ft (~1,500 m), with its contact metamorphism envelope first encountered at about 4,750 ft (1448 m)). The Stockton Formation was originally anticipated to occur at these depths, and at and below this point, down to the total depth of the well (6,870 ft; 2,094 m), geologic layers were found to be unreasonable candidates for CO_2 injection because of their low permeability and partially metamorphosed nature. For these reasons, the research team was constrained to search for geologic layers amenable to CO_2 injection at shallower depths. A "clean" sandstone interval between the depths of about 4,180 and 4,200 ft (1,244–1,280 m) was identified as a good potential target, because of reasonably good permeability and low clay content. This interval was tentatively determined to belong to the Passaic Formation. A sample from this interval (Sample 2-41R, collected at 4,191 ft; 1,277 m) was selected and split for CO_2-brine-rock interaction experiments. XRD analyses of one of the splits (Weatherford Laboratories, 2012) were conducted to identify minerals

taking part in reactions and provide the initial mineralogy for input into geochemical and reactive transport simulations (Table 3.1).

Table 3.1. XRD Analysis of potential target formation (sandstone).

Reactant	wt. %
Plagioclase	27.00
Quartz	57.96
Microcline	13.00
Anhydrite	1.00
Calcite	1.00
Kaolinite	0.01*
Illite	0.01*
Chlorite	0.01*
Hematite	0.01*

*Assumed in the modeling; reported as "traces"

3.2 Composition of the Deep Brine

Only two formation water samples could be recovered while drilling well Tandem Lot Well #1. These were collected at depths significantly shallower (2,322 and 3,058 ft; 708 and 932 m) than the originally anticipated depth of potential CO_2 injection (around 5,000 ft/1,500 m, see Section 1.2). As discussed below, the salinity of these two "shallow" water samples was found to be relatively low and thus likely not representative of deeper brines. No other fluid analyses from other deep wells drilled within the area of interest were found to help assess the composition of deep brines in the Newark Basin. For this reason, the composition of the deep brine had to be reconstructed based on the mineralogy of the target formation (Table 3.1), the composition of shallow water samples collected while drilling the Tandem Lot Well #1, and a review of the literature about the geochemical evolution of the basin.

The Newark Basin is a Mesozoic fluvial and fluvial/lacustrine rift basin. Its main geologic formations (Stockton, Lockatong and Passaic Formations, Figure 1.1) are characterized by particularly sodic sandstones (Na metasomatism) resulting from albitization of detrital plagioclase and also in part from sodium in authigenic silicates from alkaline brines/evaporites in lacustrine environment (van de Kamp and Leak, 1996). The sandstones are arkoses, derived from a basement rich in felsic rocks. Deep brines in the Newark Basin likely developed from evaporative concentration of low-salinity waters permeating sediments some time after deposition (van de Kamp and Leak, 1996), with an elevated salinity resulting primarily from evaporative pumping of groundwater rather than from evaporation in lakes; in rift basins, the circulation of meteoric water can penetrate several kilometers into sedimentary formations (e.g., Wolela and Gierlowski-Kordesch, 2007). Therefore, the main processes controlling the composition of deep brines in this basin are expected to be brine-rock interactions characterized by albitization of plagioclase, accompanied by evaporation.

On the basis of this information, the composition of the deep brine was reconstructed by simulating the reaction of the targeted formation (Table 3.1) with the deepest fluid sample recovered in the Tandem Lot

Well #1, followed by evaporation in contact with the reacted rock. In order to simulate evaporation, a target salinity had first to be estimated, as discussed below. Simulations were then run using a multicomponent reaction-path geochemical model, with details presented later in this section.

3.2.1 Salinity

Two water samples were recovered from the exploratory well (Tandem Lot Well #1) as follows (Schlumberger, 2012):

- Sample R1.02 at 2,322 ft below ground, with a salinity around 3,000 mg/L
- Sample R1.01 at 3,058 ft below ground, with a salinity around 7,000 mg/L

No other fluid analyses from other deep wells were found within the area of interest. For this reason, salinity logs from well Tandem Lot Well #1 were used to estimate the groundwater salinity at the location of the sandstone targeted for experiments (at a depth of 4,191 ft, Section 2.5). The salinities read on the logs (Figure 3.1, hereafter referred to as TDS_{calc} because these are originally calculated from resistivity measurements) were correlated with the measured salinities of water samples R1.01 and R1.02 (hereafter referred to as TDS_{true}, taken as the sum of the measured concentrations of dissolved inorganic species in these samples). This yielded a ratio TDS_{true}/TDS_{calc} averaging ~1.2 (Table 3.2). Using this ratio, the maximum TDS_{calc} value from the salinity logs around the location of core sample 2-41R at 4,191 ft (about 14,000 mg/L) converts to a TDS_{true} value about 17,000 mg/L (Table 3.2). Above around 4,750 ft, the upper limit of the contact metamorphism envelope associated with the Palisade Sill, TDS_{calc} values at other locations of low gamma and density (suggestive of higher permeability) appear to range between 10,000 and 20,000 mg/L, translating to TDS_{true} values between 12,000 and 24,000 mg/L.

On the basis of this approximate exercise, and recognizing its uncertainty, the salinity of deep brines in the vicinity of the formation targeted for experiments and reactive transport simulations were assumed to be on the order of 20,000 mg/L. It should be noted that fluids from a well in the same basin but quite far from the location of interest to the Southwest, in Montgomery County, Pennsylvania (Paresis Well) were reported to have concentrations of chlorides of 22,000 mg/L at 6,100 feet and 24,000 mg/L at 6,300 feet (Dan Collins, personal communication), thus in agreement with our estimated salinity values.

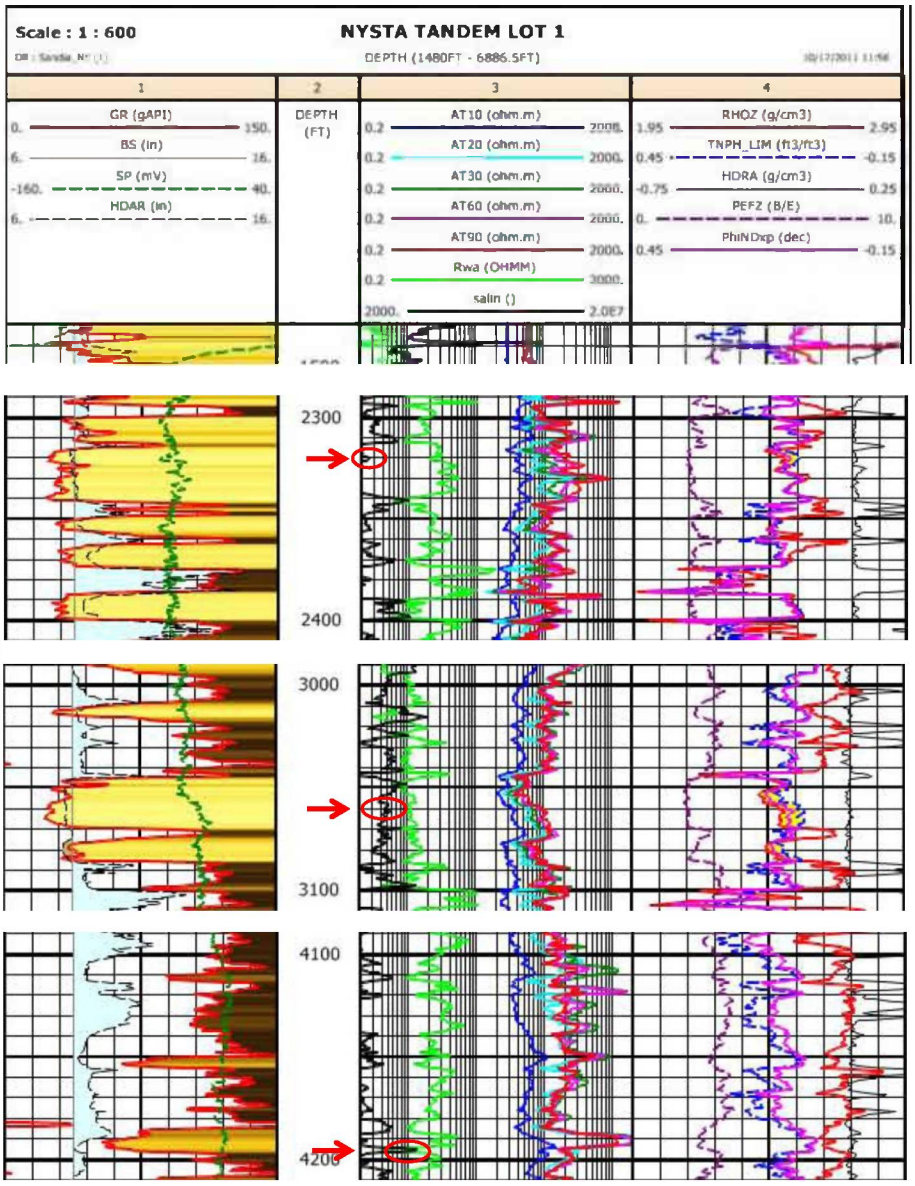

Figure 3.1. Tandem Lot Well #1 logs: spots at 2,322 ft and 3,058 ft show the recorded salinity (TDS_{calc}) at the location of the collected fluid samples. The high-salinity spot near 4,200 ft is close to the location of sample 2-41R at 4,191 ft.

Table 3.2. Estimation of deep brine salinity.

Depth Ft	TDS_{true} mg/L	From logs TDS_{calc} (approx) mg/L	Ratio TDS_{true}/TDS_{calc}
Fluid analyses:			
2322	3147	2551	1.23
3058	6740	6000	1.12
Selected interval:			Average= ~1.18
4191	17000*	14000	
Other interval:			
4650	24000*	20000	

* Calculated and rounded using the average TDS_{true}/TDS_{calc} ratio

3.2.2 Reconstruction of deep brine composition

3.2.2.1 Composition of recovered fluids

The collected fluid samples R1.01 and R1.02 are of type Na-SO_4, with proportions of major constituents shown in Figure 3.2. The fluid sample R1.01 at 3,058 ft (more saline of the two) was selected to reconstruct the brine (Table 3.3). This fluid sample was significantly degassed prior to analysis (Table 3.3). To compute the fluid composition at depth, the pH and bicarbonate composition were first recomputed to yield both charge balance and equilibration with calcite at 25°C, the approximate temperature of flashing and analyses. This was done using program GeoT (Appendix A2) (Spycher et al., 2013; 2014) and thermodynamic data discussed in Appendix C. The concentration of aluminum was assumed to be controlled initially by equilibration of the brine with illite. These calculations at 25°C bring the pH down to 6.14 and the total dissolved CO_2 up to 0.07 molal (~3,000 ppm) (Table 3.3). The resulting fluid was then speciated using program CHILLER (Appendix A3) (Reed, 1982; 1998) and the same thermodynamic database as for the GeoT computations (Appendix C) at both 25°C and 50°C, allowing supersaturated minerals to precipitate. The temperature of 50°C was initially estimated as a reasonable temperature at a targeted depth of CO_2 injection around 5,000 ft, given the geothermal gradient measured in Tandem Lot Well #1. This exercise did not significantly affect the fluid composition or pH, and yields a solution close to equilibrium with reasonable minerals, as indicated by the saturation index values (log(Q/K)) in Table 3.3. The fluid at 50°C was then used to react the brine with formation minerals as described below.

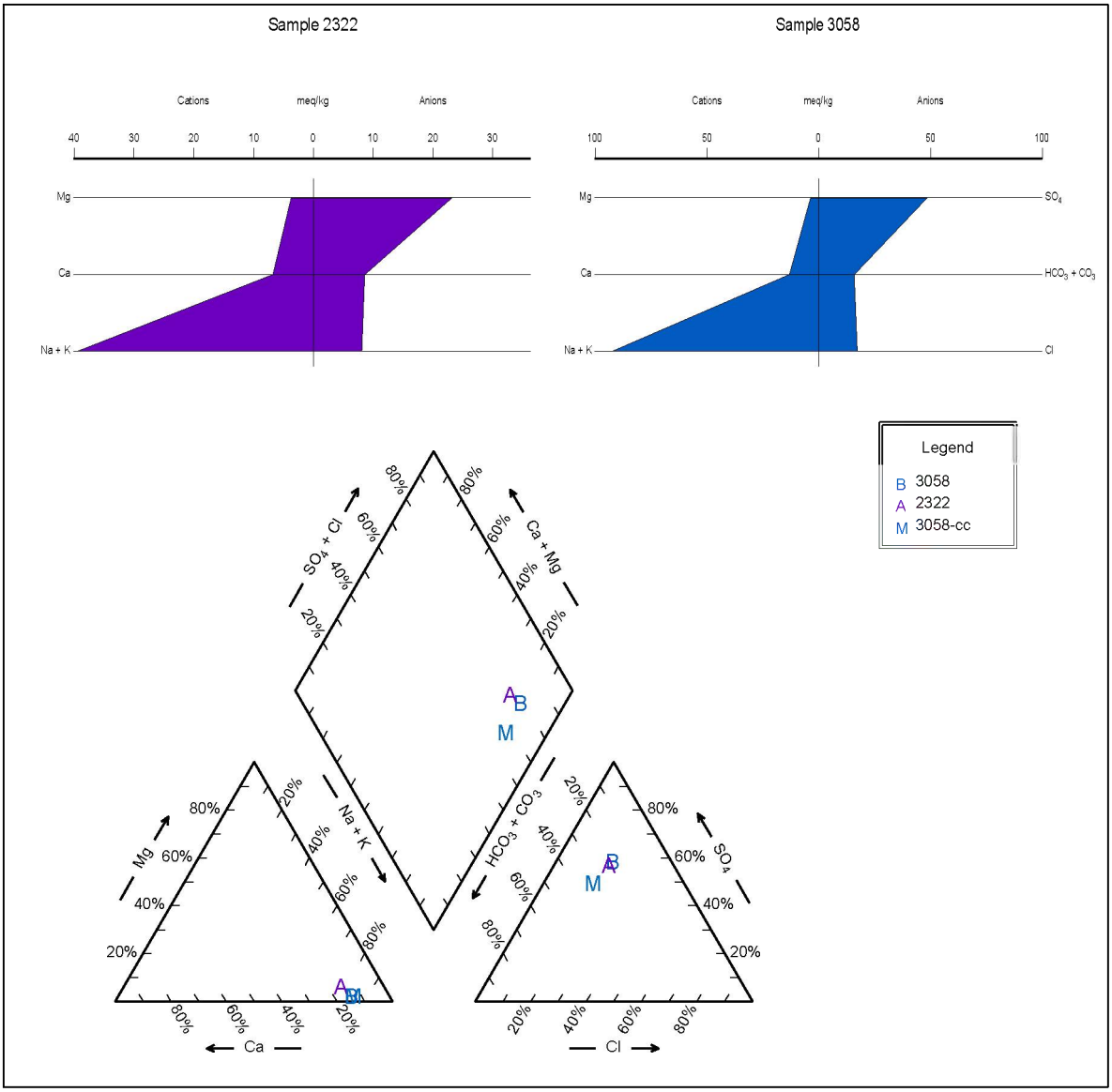

Figure 3.2. Composition of collected fluid samples. The sample name corresponds to the sampled depth. Sample 3058-cc is re-equilibrated with calcite at 50°C.

Table 3.3. Composition of collected fluid sample at 3,058 ft and recomputed concentrations (initial analyses from Schlumberger, 2012).

Sample ID	R1.01				
Depth)	3058 ft	932 m			
Pressure	1198 PSIA	81.5 bar	log(P)=1.91		
Temperature	73°F	22.8°C			
Gas/Water ratio	0.4				
pH (lab 25°C)	7.448	Flashed			
Computer code			**GeoT**	**CHILLER**	**CHILLER**
pH calc		7.448	6.141	6.141	6.00
	mg/kg	**mol/kgH_2O**	**25°C calcite-Eq**	**25°C Equil**	**50°C Equil**
Cl-	608.2	1.73E-02	1.73E-02	1.73E-02	1.73E-02
SO_4--	2331.72	2.44E-02	2.44E-02	2.44E-02	2.44E-02
HCO_3-	1032.92	1.70E-02	7.07E-02	8.85E-02	8.85E-02
HS-	2.9	8.83E-05	8.81E-05	8.81E-05	8.81E-05
Si	11	3.94E-04	3.94E-04	3.94E-04	3.94E-04
Al+++	NA	NA	1.42E-08	1.42E-08	1.42E-08
Ca++	259.9	6.53E-03	6.51E-03	6.51E-03	6.51E-03
Mg++	44.3	1.84E-03	1.83E-03	1.83E-03	1.83E-03
Fe++	3.27	5.90E-05	5.88E-05	5.88E-05	5.88E-05
K+	23.5	6.05E-04	6.03E-04	6.03E-04	6.03E-04
Na+	2108.7	9.23E-02	9.21E-02	9.21E-02	9.21E-02
Sr++	3.221	3.70E-05	3.70E-05	3.70E-05	3.70E-05
F-	NA	NA	1.0E-06*	1.0E-06*	1.0E-06*
B	2	1.86E-04	1.86E-04	1.86E-04	1.86E-04
Li+	0.4	5.80E-05	Not modeled	Not modeled	Not modeled
Br-	5.59	7.04E-05	Not modeled	Not modeled	Not modeled
Ba++	0.27	1.98E-06	1.98E-06	1.98E-06	1.98E-06
NH_4+	44	2.46E-03	2.45E-03	2.45E-03	2.45E-03
Mn++	0.65	1.19E-05	1.19E-05	1.19E-05	1.19E-05
P	0.32	1.04E-05	Not modeled	Not modeled	Not modeled
Zn	0.29	4.47E-06	Not modeled	Not modeled	Not modeled
Glycolic	27.3	3.61E-04			
Formic	8.5	1.86E-04	Take acetate as the sum of all carboxilic acids		
Acetic	218	3.65E-03	4.23E-03	4.23E-03	4.23E-03
Propionic	2.6	3.53E-05			
Charge balance		2.46E-02	< 1.E-06	< 1.E-06	< 1.E-06
* Assumed					

3.2.2.2 Brine reconstruction by water-rock reaction and evaporation

The recomputed fluid at 50°C was then numerically reacted with the sandstone of the targeted interval using the multicomponent reaction-path simulation program CHILLER (Appendix A3) (Reed, 1982; 1998). This was accomplished by progressively "titrating" into the solution the sandstone composition

shown in Table 3.1. For each mineral, the titration stopped once the fluid reached saturation with respect to that mineral. The titration continued up to a water/rock mass ratio near 1, at which point the fluid was saturated with respect to all major relevant minerals.

The composition of reacting plagioclase was not determined. For this reason, several simulations were carried out with different plagioclase compositions: An20, An10, An5, and An2. It should be noted that because the simulations were started with a fluid that is already a basinal brine (albeit not very concentrated), the starting system is considered to have already undergone some degree of plagioclase albitization. The plagioclase composition was found to strongly affect the model results, however with results for An20 composition essentially the same as for An10, but changing significantly between An10 and An5 compositions. This is because above a composition of about An5, the formation of laumontite seems to limit the Ca concentration of the fluid and limits the precipitation of anhydrite, which then limits the SO_4 concentration, while Na is also limited because of a lesser amount of Na in the reacting plagioclase. As a result, the Na/SO4 ratio does not change significantly, whereas the Na/Ca ratio changes by one order of magnitude between the An10 and An5 cases. It should also be noted that the sodic phase typically present in the Newark basin sediments (in addition to albite) is analcite ($NaAlSi_2O_6{:}H_2O$), whereas in the simulations, laumontite $Ca(AlSi_2O_6)_2 \cdot 4H_2O$ is predicted to precipitate, likely because of the somewhat elevated initial Ca concentration and possibly a temperature not elevated enough to favor analcite over albite. As described below, the formed laumontite eventually re-dissolves once the brine is concentrated.

The fluids obtained in this fashion were then numerically evaporated using the same multicomponent reaction-path program (CHILLER). Each fluid was maintained in contact with solids at all times, and starting with the solid assemblage that resulted from rock titration. This, in effect, simulates evaporation of the brine *in situ* for a closed system under equilibrium conditions. Results are shown in Table 3.4 for the case of 2x evaporation for each fluid, and also a case of 10x evaporation for the An10 fluid. The evaporation increases the Na/Ca ratio because of preferential precipitation of anhydrite upon concentration of the solution. In the An10 case, the laumontite formed during the rock-titration simulation dissolves upon evaporation. The An10 case shows a much smaller SO_4/Cl ratio than the An5 or An2 cases.

Table 3.4. Compositions resulting from numerical evaporation of fluids in Table 3.2 reacted with the sandstone shown in Table 3.1.

Species	An10 2x molal	An10 10x molal	An5 2x molal	An2 2x molal	An10 2x Ppm	An10 10x ppm	An5 2x ppm	An2 2x Ppm
pH	8.48	7.83	7.88	7.73				
TDS					6155	21816	19335	27583
Cl-	3.47E-02	1.75E-01	3.47E-02	3.47E-02	1221	6074	1205	1195
SO_4--	2.47E-02	5.95E-02	1.19E-01	1.80E-01	2359	5599	11241	16807
HCO_3-	4.58E-05	2.43E-04	4.85E-04	8.81E-04	2.8	14.5	29	52
HS-	1.79E-07	3.54E-08	3.76E-08	2.55E-08	0.0059	0.0012	0.0012	0.0008
Si	3.11E-04	2.77E-04	2.78E-04	2.74E-04	19	16	16.4	16
Al+++	1.22E-07	3.06E-08	3.40E-08	2.48E-08	0.0033	0.0008	0.0009	0.0007
Ca++	1.69E-02	2.00E-02	9.61E-03	8.92E-03	671	784	378	348
Mg++	9.36E-07	2.83E-05	3.44E-05	8.35E-05	0.0226	0.676	0.82	1.97
Fe++	1.74E-08	3.05E-07	2.97E-07	6.20E-07	0.00097	0.0167	0.0163	0.0337
K+	1.68E-04	8.41E-04	8.17E-04	1.22E-03	6.5	32.2	31.3	46
Na+	5.51E-02	2.77E-01	2.58E-01	3.81E-01	1260	6239	5826	8514
Sr++	7.41E-05	2.75E-04	7.41E-05	7.41E-05	6	24	6.4	6.3
F-	2.00E-06	1.01E-05	2.00E-06	2.00E-06	0.038	0.188	0.037	0.037
B	3.73E-04	1.88E-03	3.73E-04	3.73E-04	23	114	22.6	22
Ba++	1.10E-07	1.37E-07	4.83E-08	4.27E-08	0.015	0.018	0.0065	0.0057
NH_4+	4.91E-03	2.48E-02	4.91E-03	4.91E-03	88	438	87	86
Mn++	2.38E-05	1.20E-04	2.38E-05	2.38E-05	1.30	6.47	1.28	1.27
Acetate	8.47E-03	4.28E-02	8.47E-03	8.47E-03	497	2474	491	487
F(CO_2)	-5.15	-3.73	-3.42	-0.92				
Na/Ca	3.3	13.9	27	43	1.9	8.0	15.4	24
SO_4/Cl	0.7	0.3	3.4	5.2	1.9	0.9	9	14
SO_4/Na	0.4	0.2	0.5	0.5	1.9	0.9	1.9	2.0

On the basis of these simulations, it was decided to adopt the 10x evaporated An10 case for experimental and modeling analyses. These fluids yield a TDS near 20,000 ppm, in agreement with expectations from salinity logs, and are equilibrated with typical rock primary and secondary (diagenetic) phases, as described in more detail later in Section 5. Selecting the case with the more Ca-rich plagioclase provides enough Ca to keep sulfate lower (relative to Cl) by precipitation of anhydrite, and seemed more appropriate than taking a brine with a much higher SO_4 content. Obviously, the Na-Cl-SO4 brine composition reconstructed in this manner has a very large uncertainty, which carries through the experimental and modeling results presented in this report.

4. LABORATORY EXPERIMENTS: GEOCHEMICAL INTERACTIONS BETWEEN CO_2-SATURATED BRINES AND SANDSTONE SAMPLE 2-41R, NEWARK BASIN

In this section, we report on laboratory experiments reacting supercritical CO_2 with various brine chemistries and sandstone samples collected in exploration well Tandem Lot Well #1. Results from geochemical modeling analyses of these experiments are also presented. The mineralogy of reacted sediments and assumed deep-formation brine composition used in the experiments were discussed previously in Section 3.

The objective of the experiments was to help guide the reactive transport modeling, and also provide some data to assess the confidence in the brine reconstruction analyses presented in Section 3. The pre-equilibration experiments involving rock-brine reaction without CO_2 provided pH and dissolved element concentration data that can be compared directly with the reconstructed brine composition. The results of experiments involving the reaction of CO_2 helped define the reservoir minerals most likely to be reactive upon CO_2 injection, and also helped assess secondary minerals likely to form as a result of this interaction. This iterative approach (modeling informed by experiment) allowed us to predict reservoir performance (Section 6) for time periods not amenable to experimental confirmation.

4.1 Brief Experimental Details

Three experiments pertaining specifically to the Newark Basin were performed to investigate the effects of CO_2 saturation on fluid-mineral reactions. These were carried out in flexible gold hydrothermal reaction cells (Seyfried et al., 1987). The advantage of this experimental methodology is that the reaction cell is largely inert, and samples may be periodically withdrawn (through a Ti sampling valve) without decreasing system pressure and degassing dissolved CO_2. Starting fluids were purged with methane (to the best of our ability) in order to remove as much dissolved oxygen as possible, while introducing a reduced species more applicable to natural systems. In all three experiments, the solid material was sandstone sample 2-41R (see Table 3.1, XRD analysis). The refractive index of fluid samples was measured during the experiments to assure that the system was leak-free (i.e., that the fluid in the gold cell was not contaminated by the confining fluid, i.e., deionized water). The operating conditions of these three experiments are described below. It should be noted that a pressure (100 bar) below that expected in the field (~150 bar) was specified because of experimental limitations. However, the CO_2 solubility increase between 100 and 150 bar at the temperature considered is small (<10% change), and not expected to change the outcome of these experiments.

Experiment NB2b: T = 150°C, P = 100 bars. The starting solution was 0.7 molal NaCl, which was saturated with CO_2 for the duration of the experiment. Initial fluid/rock mass ratio was ~200:1, and the sandstone grain size fraction was ~150-250 μm. The intent here was to both simplify the fluid-chemistry interpretation and to "accelerate" reaction progress, thus bring up more clearly the effects of rock-water interaction, (e.g., the potential formation of thermodynamically stable secondary minerals). This is because these trends are significantly muted at the low temperature (~50°C) representative of CO_2 sequestration in the Newark Basin.

Experiment NB3: T = 53°C, P = 100 bars. The starting solution is designated as An10(10x) and was created as a laboratory surrogate to the An10(10x) calculated fluid composition for the natural system (see Section 3.2.2, Table 3.2): Na = 286 mmolal, Ca = 3 mmolal, K* = 1.7 mmolal, Mg = 28 μmolal, SO_4 = 59 mmolal, Cl = 174 mmolal (*K target was 0.85 mmolal, but we suspect possible contamination from the NaCl and/or Na_2SO_4 starting salts). The initial fluid/rock mass ratio was ~235:1, and the sandstone grain-size fraction was ~150-250 μm. The intent here was to use a more appropriate fluid chemistry, although this is only possible for the alkali and alkaline earth components, given the difficulty in making stable solutions at room temperature containing the less soluble rock-forming elements (e.g., Al, Si, Fe). A "pre-reaction" period of about one month (at pressure 100 bar and temperature 53°C) of fluid-rock interaction was undertaken prior to the addition of CO_2 in order to (1) better differentiate the effects of the immediate acidification that occurred in NB2b, (2) generate a starting fluid chemistry more likely to resemble the field situation, and (3) provide pre-equilibrated fluid-composition data that could be used to assess the reconstructed brine composition discussed in Section 3.

Experiment NB6: T = 53°C then 150°C, P = 100 bars. This experiment was identical to NB3, except that a lower fluid/rock mass ratio was used (~26:1) in addition to a lower grain size fraction (45-150 μm). The intent here was to use a different approach (increase surface area/volume) to once again "accelerate" reaction progress and, thus, provide a potentially clearer trend in the thermodynamic evolution of the chemical system. The rock and synthetic brine were also pre-equilibrated before addition of CO_2. At 53°C, a near steady-state fluid composition was observed in this experiment after ~75 days. Fetr this time, to further accelerate reactions and provide comparison to Exp NB2b, fresh An10(10x) solution was injected (~1:1 dilution of remaining fluid in the cell), and the temperature was increased to 150°C. The reaction progress was then tracked via fluid-chemistry changes occurring over an additional 50-day time period.

4.2 Fluid Analyses

Following extraction from the reaction cell, fluid samples were immediately diluted and acidified (ultra-pure HNO_3) in order to preserve samples for later analysis. K, Ca, Mg, Fe, Al and Si (major elements) were analyzed by ICP-OES. Any changes in Na cannot be resolved analytically, due to the high initial concentration. Mn was also measured by ICP-OES for NB3. A suite of trace metals was analyzed for NB2b using ICP-MS. pH (25°C) was measured using a Thermo-Ross electrode, standardized prior to each measurement. Time series data from experiments NB2b, NB3, and NB6 are given in Tables 4.1 to 4.3, respectively. The bulk and trace chemistry of the 2-41R material was also characterized, and the results are given in Table 4.4.

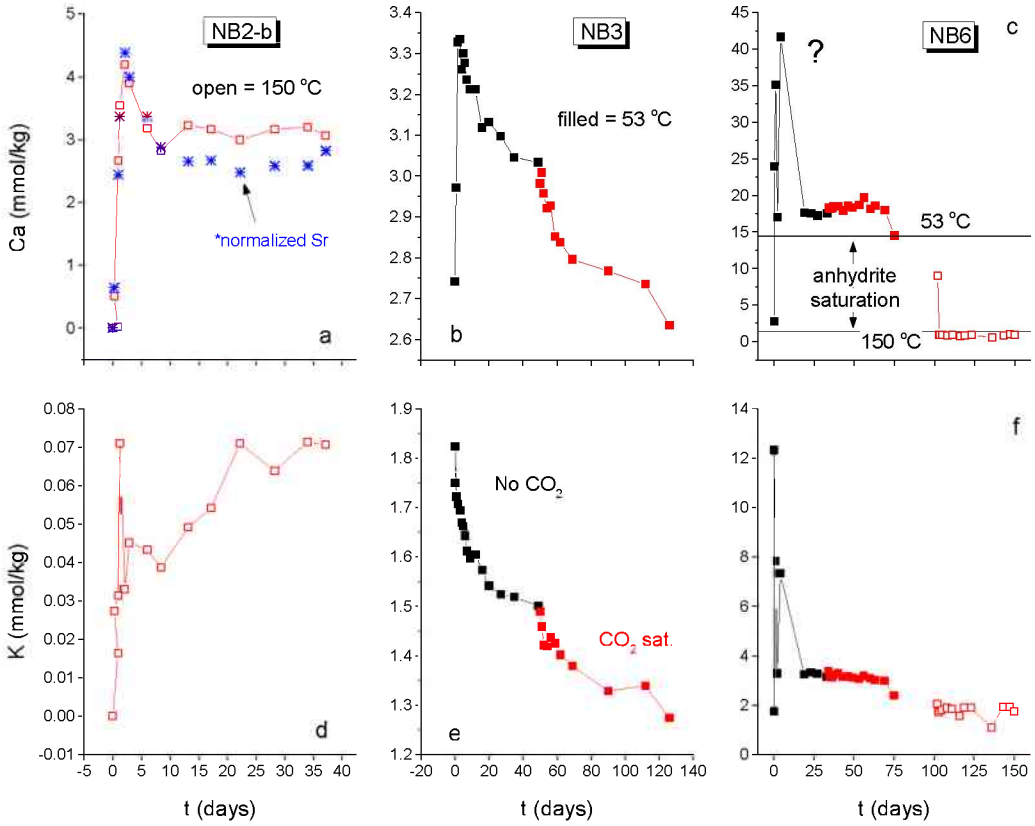

Figure 4.1. Time-series for dissolved Ca and K from laboratory experiments NB2b, NB3 and NB6. Normalized Sr data is also shown in panel (a). The black lines (with black symbols) represent the pre-equlibration period. The red lines (with red symbols) reflect the CO_2 saturated (100 bars) portions of the experiments. Filled and open symbols reflect T = 53 and 150°C, respectively. Anhydrite saturation is suggested in NB6 (b). See text for discussion.

4.3 Results and Discussion

We frame our observations around the results of Exp. NB3, due to best applicability to the modeling applications presented later in Sections 5 and 6 (T ~54°C, and sulfate-bearing initial fluid) and a clearer cause-and-effect regarding the presence of CO_2. Exp. NB6 was carried out in the hope that higher rock surface area should allow reactions to progress to a greater extent for reasonable laboratory timescales. However, meaningful temporal trends in the data are much less clear, and many elements were actually lower in concentration at the termination of the experiment, largely due to rock-water interactions at the higher temperature. Within the context of our discussion, the NB6 data are nonetheless consistent with our general observations regarding Exp. NB3.

In a broad sense, the most compelling observations are that K and Ca exhibit similar behavior (Figure 4.1) that is, in turn, significantly different from Mg, Fe, Al, and Si (Figures 4.2, 4.7), all of which also behave in a similar manner. Data in red denotes CO_2 saturated portions of the experiments in both Figures 4.1 and 4.2.

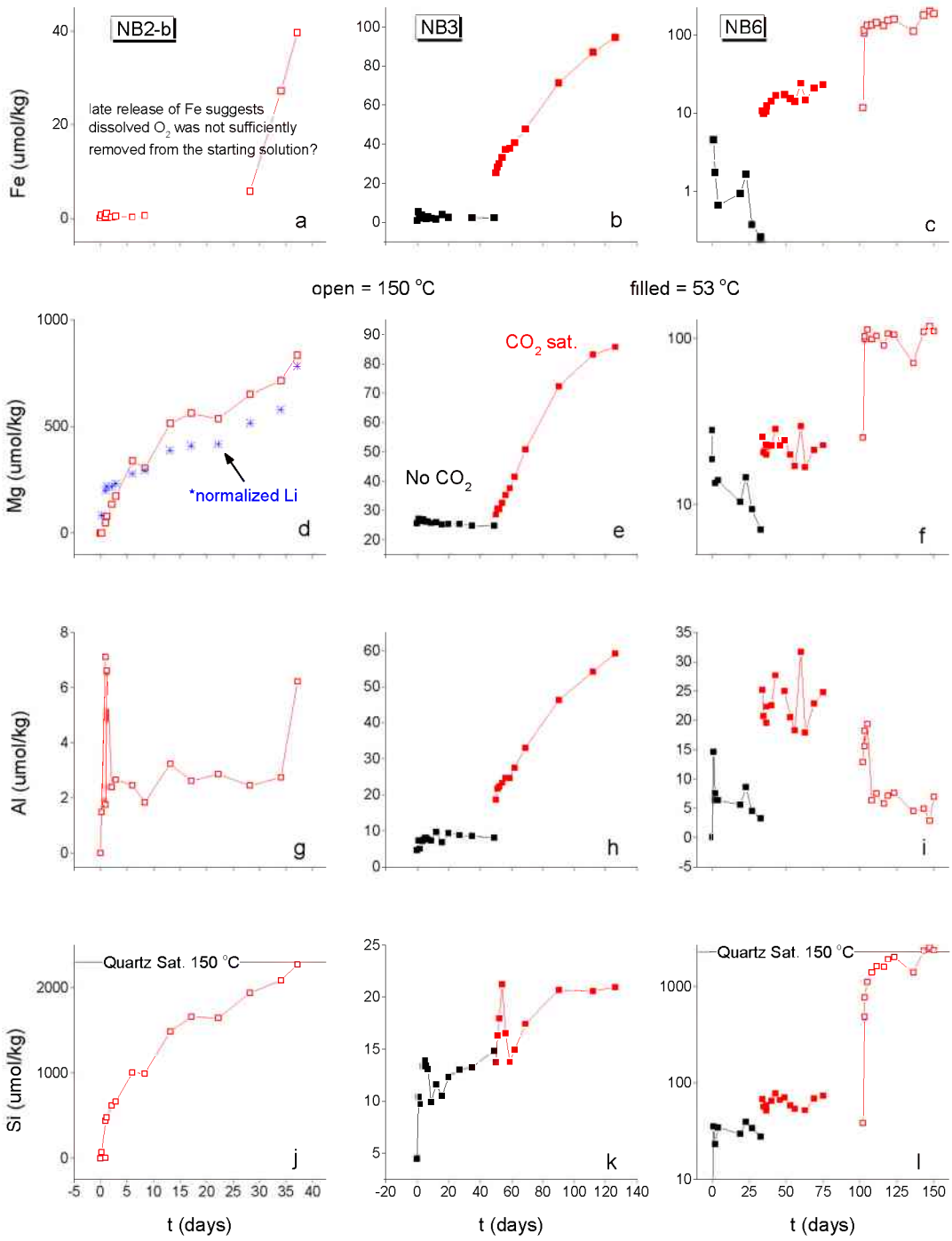

Figure 4.2. Time-series data for dissolved Fe, Mg, Al, and Si from laboratory experiments NB2b, NB3, and NB6. Normalized Li data (see text) is also shown in panel (d). The black lines (with black symbols) represent the pre-equlibration period. The red lines (with red symbols) reflect the CO_2-saturated (100 bars) portions of the experiments. Filled and open symbols reflect T = 53 and 150°C, respectively. Quartz saturation is suggested at 150°C in NB2b (j) and NB6 (l). See text for discussion.

In order to calculate mineral saturation states for NB3, four *in situ* pH values were derived via electrical balance model calculation using the measured pH (25°C) as a guide (Figure 4.3). All calculations were performed using GWB (Bethke, 2008) and a 100 bar, 0-300°C database generated from SUPCRT92, with appropriate updates (Johnson et al., 1992; Shock et al., 1997; Sverjensky et al., 1997), by the program DBCreate (Kong et al., 2013).

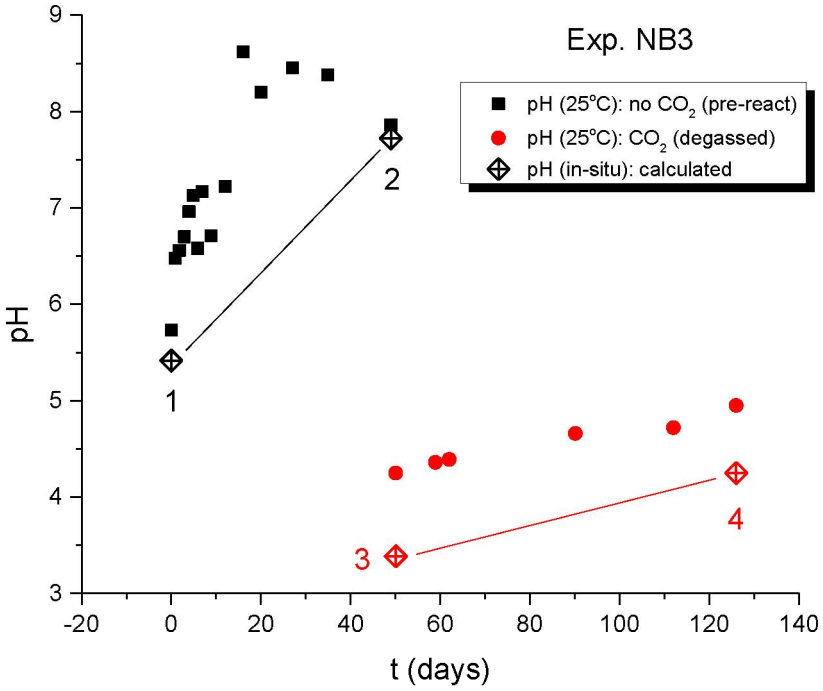

Figure 4.3. Time series pH (25°C) of experiment NB3 (T = 53°C) (squares and circles) and calculated in-situ pH values (diamonds) used in deriving solution saturation states depicted in Figure 4.4. See text for details. Numbers refer to pH value points discussed in the text.

In situ, pre-reaction pH values (point #1-2, Figure 4.3) are simply a re-speciation via electrical charge balance to T = 53°C, P = 100 bars. Once CO_2 was introduced into the experimental system, the measured pH was questionable due to the open-atmosphere degassing of the samples. Thus, the value of pH point #3 was derived by calculating the *in situ* pH of the measured fluid composition if saturated with CO_2, saturation being ~0.8 molal after Duan and Sun (2003). Though the measured (degassed) values were not explicitly used in these calculations, a consistent methodology of measurement yielded a well-defined temporal increase in pH with increasing time of reaction (reaction progress). Our estimation of in-situ pH point #4 was thus derived by increasing the value of pH point #3 by a similar order of magnitude (~0.85 units), accounting for the continued existence of the imposed CO_2 pressure. Mineral formation was suppressed in all in situ pH calculations. Saturation indices were calculated within the Na-K-Mg-Ca-Al-Si-SO_4-Cl-CO_2-H_2O-system.

While not apparent due to kinetic limitations in experiments where T = 53°C, dissolved silica should eventually reach quartz saturation, and this appears to have occurred in the NB2b experiment, as well as the 150°C leg of NB6 (Figures 4.2(j)-(l)). Saturation indices for NB3 (Figure 4.4) are consistent with the

idea that an albite (an/or plagioclase) - K-spar system should be destabilized by the drop in pH associated with CO_2 saturation, favoring the formation of kaolinite, muscovite, and paragonite.

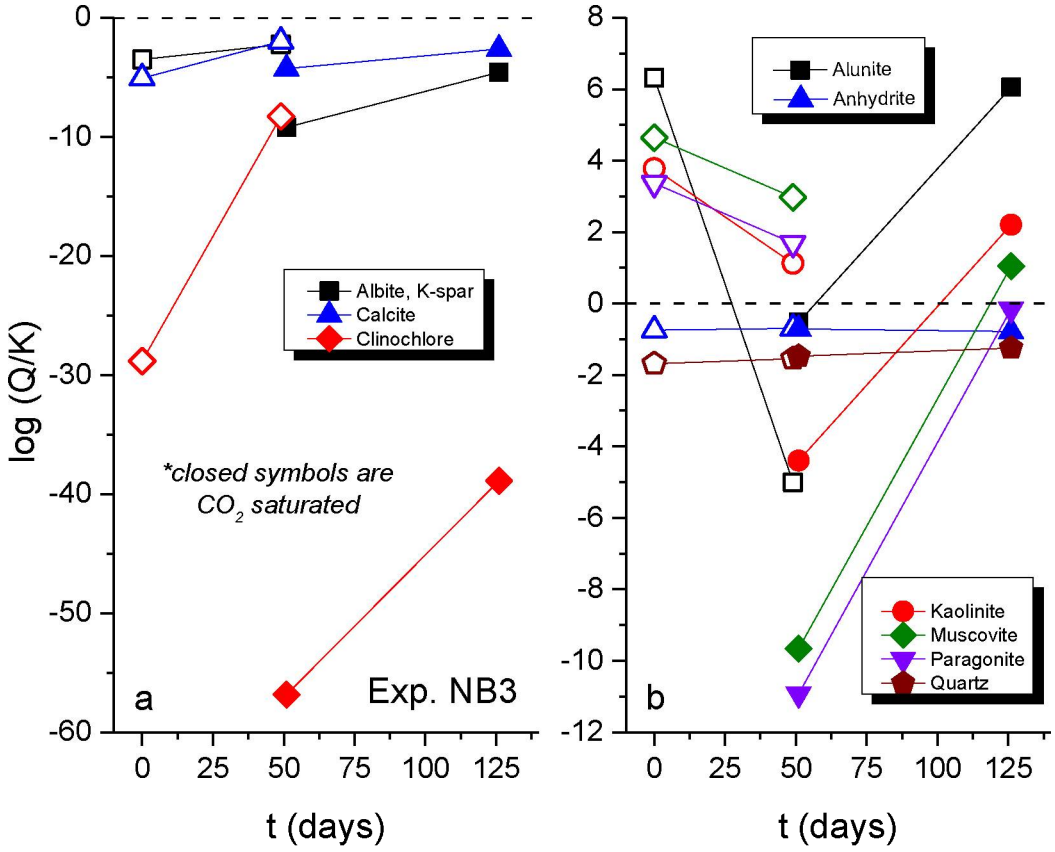

Figure 4.4. Saturation indices (time series) in experiment NB3 for select minerals calculated at T = 53°C and 100 bars. Open symbols reflect the pre-equilibratin period without CO_2; filled symbols reflect CO_2 saturation in the second half of the experiment. See text for discussion.

We note that trends in Figure 4.4 are largely due to changes in pH and/or dissolved Al; and saturation indices may be artificially high for some Al-bearing minerals (especially kaolinite) due to internal inconsistencies in the thermodynamic dataset (Tutolo et al., 2014). Regardless, the much lower Al concentrations in experiment NB2b (and NB6, 150°C) relative to NB3 (Figure 4.2) are consistent with a predicted temperature effect on solubility of nearly two orders of magnitude at relevant *in situ* pH, where fluid Al concentration is being controlled by kaolinite solubility.

Chlorite, a likely trace component (not quantitative via XRD) in 2-41R, is predicted to become highly unstable at low pH (Figure 4.4, as clinochlore), more so than most other Mg-bearing phases. High chlorite reactivity is also predicted in the reaction-transport models presented in Section 6 that additionally include kinetic parameters (e.g., Section 6.1.4). Such high affinity for chlorite dissolution is a possible explanation for the congruent behavior of Mg, Fe, Mn, and Al observed in the experiments. For example, if we normalize these data from the CO_2 saturated portion of the NB3 experiment (subtract out the respective pre-reaction values), the Al/(Mg+Fe+Mn) or Al/metal ratio is consistent with stoichiometric

chlorite dissolution, where the Al/metal ratio may decrease with time if the fluid is approaching saturation with another Al-bearing mineral (e.g., kaolinite) (Figure 4.5). This particular scenario would require the 2-41R sandstone to contain at least ~0.3 wt% chlorite, and the Fe/Mg ratio of the solid solution to be greater than unity. Furthermore, if the first sample of NB2b is normalized to unity, the release of Si/Mg achieves a steady-state ratio of ~3/1 (Figure 4.7), which is also consistent with a high Fe chlorite. However, in this case the behavior of Fe is inconsistent (see also trace element discussion, Section 4.3.1), possibly due to the abundance of other Fe-bearing phases; and the quartz-silicate-dominated nature of the mineral assemblage complicates interpretation of controls on Si dissolution.

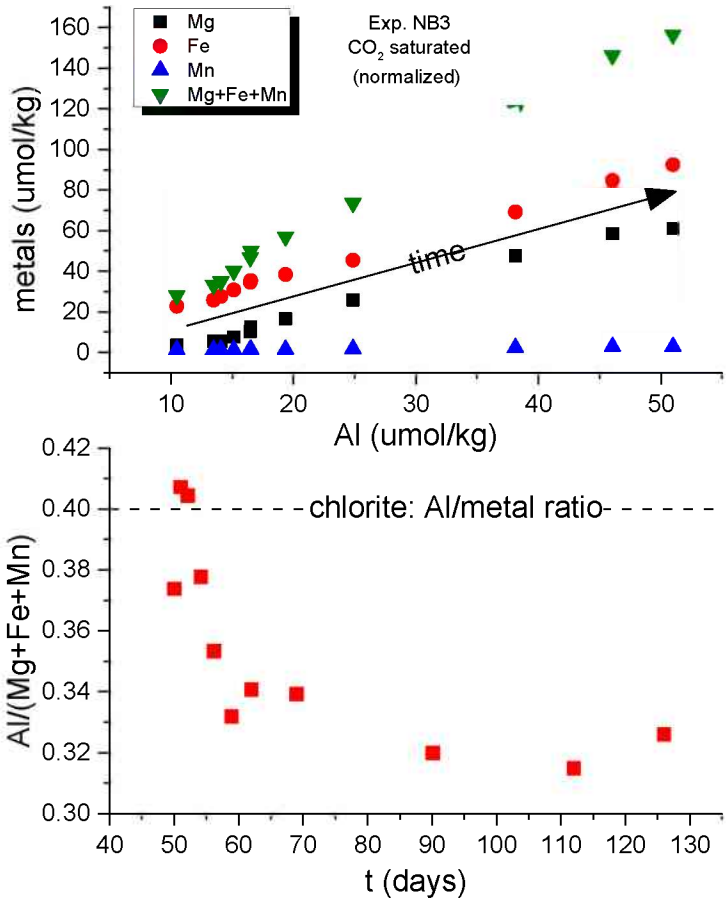

Figure 4.5. Relationship between dissolved Al and Fe-Mg-Mn in the CO_2 saturated portion of experiment NB3, suggesting a high Fe chlorite might be responsible for the release of these metals. See text for discussion.

The congruent behavior of K and Ca is more peculiar because they appear completely indifferent to pH (Figure 4.1, neglecting Exp. NB2b), an observation made possible by having performed the pre-reaction stage of the experiments. XRD analysis of 2-41R (see Table 3.1) suggests ~1 wt% of both calcite and anhydrite, minerals that would be more reactive than silicates and thus more likely to impact fluid Ca concentrations on the time scale of the experiments and in the basin-scale models presented later. Figure

4.6 presents results from more simple models, based on the experiments, that predict pH-Ca relationships for both NB3 and NB6, simulating both the pre-reaction stage and subsequent saturation with CO_2. These models consist of first simultaneously titrating an appropriate amount of calcite and anhydrite into an equivalent of the An10(10x) starting fluid, accounting for the initial fluid/rock mass ratios in the experiments. In both cases, little of the calcite actually dissolves because only a trace amount is required to increase pH to calcite saturation (see also Section 5.3). Anhydrite, however, continues to dissolve until it is completely exhausted. In order to be more consistent with the experiments, we then remove fluid from the calcite-bearing model systems to account for that removed throughout the pre-reaction period (but prior to the addition of CO_2) due to sampling. This "one step" adjustment inherently assumes these minerals react instantaneously when undersaturated, which isn't ideal, but is likely sufficiently quantitative. CO_2 is then titrated into the model systems to saturation; and, in both models, remaining calcite is completely dissolved, producing a secondary increase in the fluid Ca concentration.

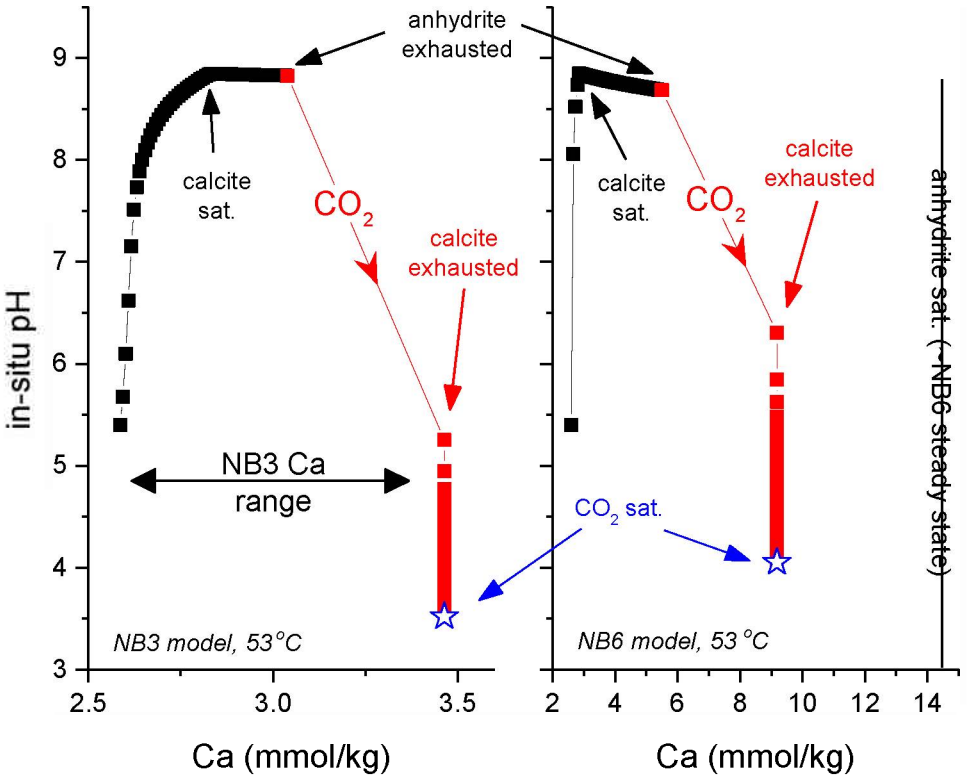

Figure 4.6. Models characterizing the expected behavior of Ca and pH in experiments NB3 and NB6 (T = 53°C). Such relationships are not consistent with the experimental data. See text for details.

These models are not consistent with the experimental data, suggesting that calcite is not an influential component of the 2-41R mineral assemblage with respect to dissolved Ca concentration. While the NB3 model (Figure 4.6) yields Ca concentrations similar to those measured in the experiment, this is mostly due to the relatively high fluid/rock ratio; and the experimental values trend in the opposite direction, decreasing throughout the course of the experiment (Figure 4.1(b)). The NB6 model fails to produce the

relatively high Ca concentrations observed in the experiment (Figure 4.6). The steady-state (later) portion of the NB6 data is consistent with anhydrite saturation (Figure 4.1(c)). However, calculations indicate this would require the anhydrite fraction of 2-41R to be on the order of ~4 wt%, and even this can't account for the great burst of Ca (and K) that occurred in the early stages of the experiment (Figure 4.1(c), (f)). In this case, we might invoke highly reactive surface areas, not only because of the lower fluid/rock ratio, but because of the smaller grain-size fraction utilized. Furthermore, the bulk chemical analysis (Table 4.4) shows a significant amount of S (4.4-6.1 wt%) with relatively little Fe; and assuming pyrite/anhydrite will account for total S, such high bulk S would suggest more than enough anhydrite (~18 wt% for 4.4% S) to fully account for the behavior of Ca in NB6. If we attribute the Ca in 2-41R to calcite-anhydrite-plagioclase, plagioclase would then comprise ~15% of the bulk Ca and would have a Ca/Na mol fraction of ~0.2. This is quite consistent with constraints imposed on the reservoir solution chemistry (i.e., coexistence of An10 plagioclase) in Section 3.2.2. Such a high anhydrite composition, however, should have also resulted in greater fluid Ca concentrations in NB3, despite the overall higher fluid/rock ratio. The discrepancies in both the mineralogy (anhydrite content) suggested by the results of the XRD and bulk analyses (Tables 3.1 and 4.4, respectively) and the results of NB3 relative to NB6 (Figures 4.1, 4.6) likely indicate heterogeneity in subsamples of the 2-41R material, which is common in sedimentary sandstones. In addition, at least part of the difference observed between the NB3 and NB6 experiments may be due to the difference in grain size used in each. Despite the low fluid/rock ratios in natural reservoirs, such heterogeneity may not be important for basin-scale modeling or actual field injections (i.e., it may only complicate experimental results), because reservoir fluids will already have been coexisting with the host lithology for much longer time scales. Regardless, given the high sulfate concentration of the An10(10x) fluid, and the indifference to pH of both Ca and K, it is difficult to suggest anything other than ion sorption/desorption and/or the dissolution/precipitation of sulfate-bearing phases in explanation of our observations. For example, it is clear that anhydrite precipitated in the second leg (150°C) of NB6 (Figure 4.1(c)) due to significantly decreased solubility with increasing T (retrograde solubility behavior). The only K-SO_4 phase currently in our database is alunite ($KAl_3(SO_4)_2(OH)_6$), and while predicted to be near saturation, its solubility should still have a rather strong pH dependence (Figure 4.4). Therefore, the broader geochemical control responsible for the changes in K and its apparent covariability with Ca is uncertain. Interestingly, Ca and K in the model calculations presented in Section 5 also exhibit a certain covariability despite largely independent mineralogical controls (~calcite and K-spar (microcline), see Figure 5.1). However, this still does not explain their indifference to the pH change associated with CO_2 injection, especially given the large difference in reaction kinetics between these two minerals (~10 log units, see Appendix C, Table C.1 associated with Section 6).

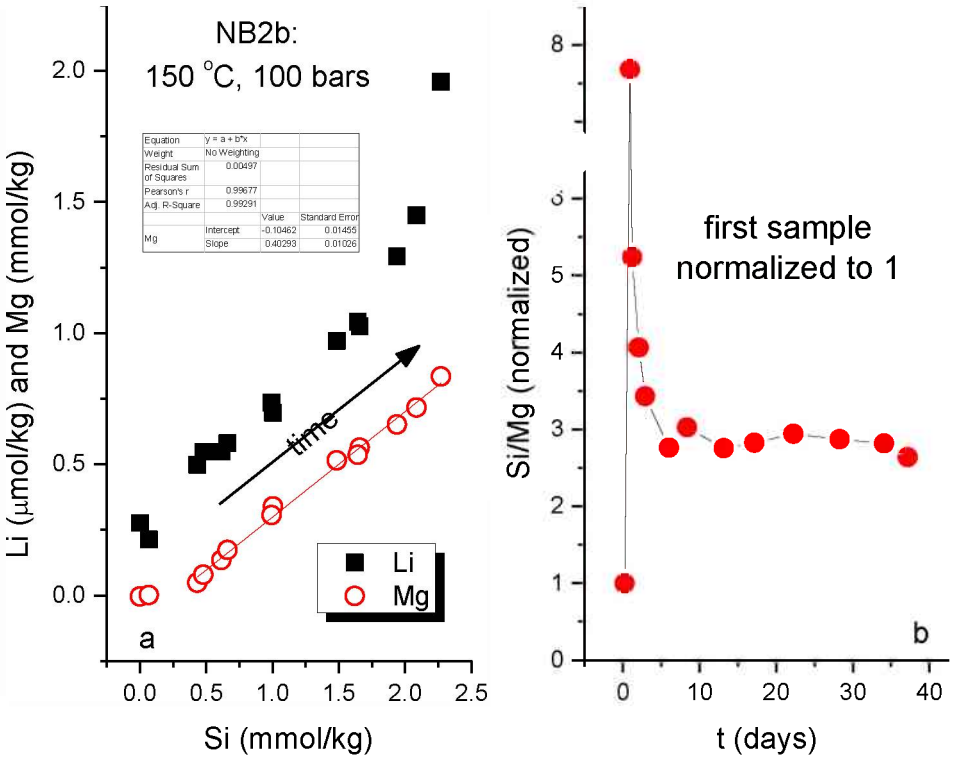

Figure 4.7. Systematics of dissolved Li, Mg and Si in experiment NB2b (CO_2 saturated, T = 150°C). See text for discussion.

Though the behavior of trace elements is largely beyond the scope of this study, we do note a few interesting correlations by graphically normalizing the data from Exp. NB2b (i.e., elemental data sets are multiplied by an arbitrary factor to bring the data within a similar linear range). As might be expected with suggested calcite or anhydrite control, the Sr time-series data closely mimic those of Ca (Figure 4.1(a)). The release of Li is similar to that of Mg (both of which correlate with Si, Figures 4.2(d), (j), 4.7), in agreement with a mutual affinity for similar sites in a crystalline lattice (similar ionic radii). A more robust linear correlation is exhibited between Li-Ba-Co (Figure 4.8(a)). In turn, Co may be used as a reference in comparing the time-series transition metal data, being normalized to Mn (most concentrated) in Figure 4.8(b). The transition metals exhibit broad commonality, but the trends are interestingly juxtaposed, suggesting the possibility of competitive sorption (e.g., on clays) throughout the experiment. After remaining near or below detection limits for the majority of the NB2b experiment (measured using less sensitive ICP-OES), the late release of Fe to solution is distinctly different than for any other metals (Figures 4.2, 4.8). This is furthermore inconsistent with the Fe solubility systematics in the NB3 and NB6 experiments. We note in Figure 4.2(a) the possibility that an excess of dissolved O_2 sufficient to suppress Fe solubility (i.e., sufficient O_2 to make Fe(+3) the dominant valence state for aqueous Fe species) may have persisted until the latest stage of the experiment.

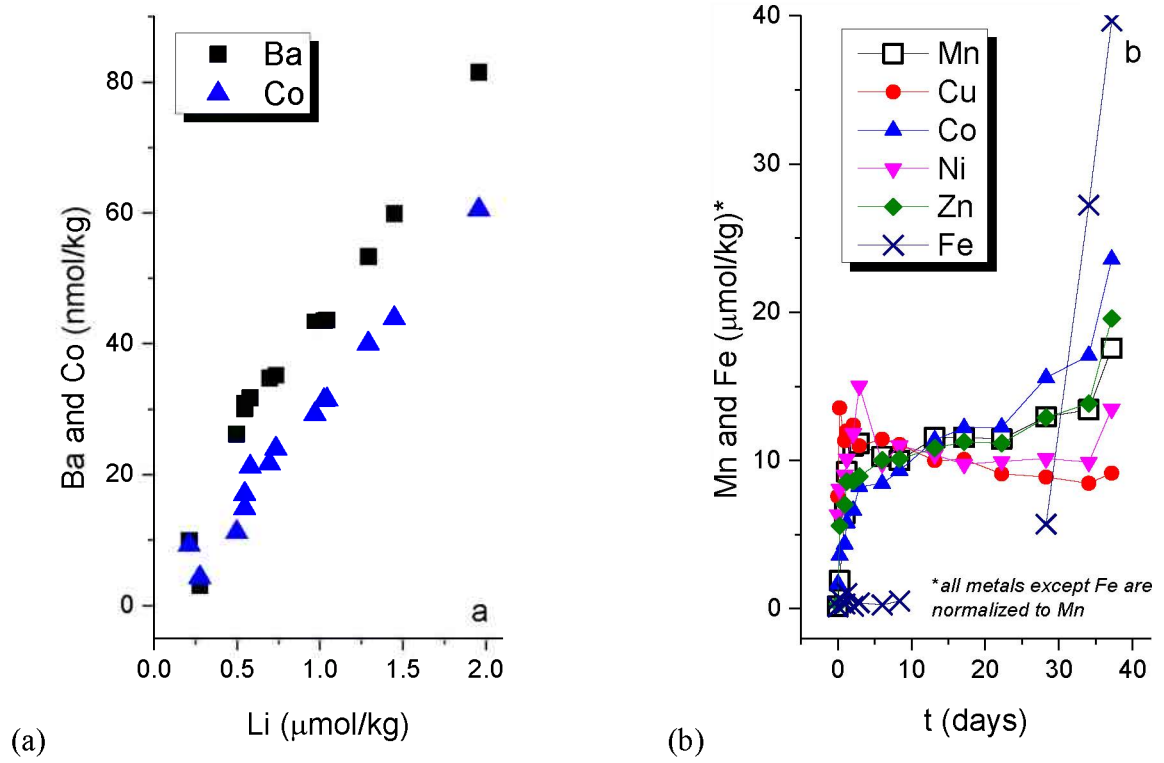

Figure 4.8. Behavior of dissolved trace metals in experiment NB2b (CO_2 saturated, T = 150°C). Panel (a) shows a good linear correlation between Li, Ba and Co. Panel (b) depicts the variable (time-series) behavior of the transition metals, where all metals other than Fe are normalized to Mn for ease of comparison. See text for discussion.

Table 4.1. Time-series data from experiment NB2b using a 0.7 M NaCl initial solution.

days	fluid/rock	pH	K	Ca	Mg	Si	Al	Fe
		(25 °C)	µmol/kg	µmol/kg	µmol/kg	µmol/kg	µmol/kg	µmol/kg
T = 150 °C, P = 100 bars, CO_2 saturated								
0.0	201	x	16.3	12	x	1.6	7.1	0.1
0.2	196	4.82	27.4	503	1	68	1.5	0.7
0.9	193	5.39	31.3	2662	48	434	1.8	0.3
1.2	189	5.45	71.1	3536	79	479	6.6	1.0
2.1	185	5.59	33.0	4189	135	614	2.4	0.2
2.9	182	5.64	45.1	3895	173	661	2.7	0.4
6.0	178	5.53	43.3	3178	339	1003	2.5	0.3
8.4	174	5.46	38.7	2818	306	993	1.8	0.5
13.2	169	5.56	49.1	3227	515	1484	3.2	x
17.1	164	5.56	54.1	3167	563	1657	2.6	x
22.2	159	5.54	71.0	2997	535	1642	2.9	x
28.3	153	5.62	63.8	3163	651	1938	2.5	5.7
34.1	147	5.68	71.4	3196	716	2085	2.7	27.2
37.2	142	5.68	70.7	3065	834	2270	6.2	39.6

days	Mn	Cu	Li	Co	Ni	Zn	Sr	Ba
	µmol/kg	µmol/kg	µmol/kg	nmol/kg	nmol/kg	nmol/kg	nmol/kg	nmol/kg
T = 150 °C, P = 100 bars, CO_2 saturated								
0.0	0.2	11.6	0.28	4.3	317	9	x	3.1
0.2	1.9	20.7	0.21	9.2	403	164	64	9.9
0.9	6.4	17.3	0.50	11.2	450	206	244	26.2
1.2	9.2	18.4	0.55	14.9	504	252	336	30.1
2.1	11.0	19.0	0.55	17.0	590	252	438	30.9
2.9	11.2	16.8	0.58	21.2	750	262	400	31.7
6.0	10.3	17.5	0.70	21.7	489	294	337	34.8
8.4	10.0	16.9	0.74	23.9	549	297	288	35.2
13.2	11.5	15.3	0.97	29.2	519	318	265	43.3
17.1	11.6	15.4	1.03	31.3	486	331	267	43.5
22.2	11.4	13.9	1.04	31.5	496	328	248	43.6
28.3	12.9	13.6	1.29	40.0	505	379	258	53.3
34.1	13.4	12.9	1.45	43.9	494	406	258	59.9
37.2	17.6	14.0	1.96	60.6	673	575	282	81.5

Table 4.2. Time-series data from experiment NB3 using the An10(10x) initial solution.

days	fluid/rock	pH	K	Ca	Mg	Si	Al	Fe	Mn
		(25 °C)	mmol/kg	mmol/kg	µmol/kg	µmol/kg	µmol/kg	µmol/kg	µmol/kg
T = 53 °C, P = 100 bars, No CO_2									
0	236	5.73	1.82	2.74	25.5	4.5	4.6	0.89	0.62
1	230	6.48	1.72	2.97	27.2	10.4	7.3	5.40	1.31
2	224	6.56	1.71	3.33	27.0	9.7	5.0	3.43	1.03
3	219	6.7	1.69	3.33	26.4	29.7	7.2	3.69	1.19
4	214	6.96	1.67	3.26	27.0	13.4	7.4	2.18	1.50
5	209	7.13	1.66	3.30	26.4	13.9	8.0	1.94	1.29
6	204	6.58	1.64	3.28	26.2	13.4	8.1	1.88	1.39
7	198	7.17	1.61	3.24	26.2	13.1	7.7	2.72	1.54
9	193	6.71	1.60	3.21	25.7	9.9	7.3	1.98	1.45
12	188	7.22	1.60	3.21	26.0	11.6	9.7	1.50	1.59
16	182	8.62	1.57	3.12	25.3	10.5	6.9	3.94	1.60
20	177	8.2	1.54	3.13	25.4	12.3	9.4	2.34	1.77
27	172	8.45	1.52	3.10	25.4	13.0	8.8	x	1.94
35	167	8.38	1.52	3.05	24.7	13.3	8.5	2.31	2.07
49	163	7.86	1.50	3.03	24.8	14.8	8.1	2.25	2.08
T = 53 °C, P = 100 bars, CO_2 saturated									
50	157	4.25	1.49	2.98	28.6	13.8	18.7	25.2	3.64
51	152	x	1.46	3.01	30.6	16.3	21.6	28.2	3.68
52	148	x	1.42	2.96	30.5	18.0	22.2	30.0	3.73
54	145	x	1.42	2.92	32.6	21.2	23.3	33.2	3.69
56	140	x	1.44	2.93	35.2	16.5	24.6	37.0	3.81
59	136	4.36	1.43	2.85	37.6	13.8	24.7	37.7	3.84
62	132	4.39	1.40	2.84	41.5	14.9	27.5	40.7	3.88
69	127	x	1.38	2.80	50.7	17.4	33.0	47.7	4.17
90	121	4.66	1.33	2.77	72.3	20.7	46.2	71.4	4.68
112	114	4.72	1.34	2.73	83.3	20.6	54.1	87.1	5.05
126	105	4.95	1.27	2.63	85.8	21.0	59.1	94.8	5.04
quench			1.28	2.59	92.9	21.1	66.1	199	5.47

Table 4.3. Time-series data from experiment NB6 using the An10(10x) initial solution.

days	fluid/rock	pH	K	Ca	Mg	Si	Al	Fe
		(25 °C)	mmol/kg	mmol/kg	µmol/kg	µmol/kg	µmol/kg	µmol/kg
T = 53 °C, P = 100 bars, No CO_2								
0	25.2	5.92	12.33	24.0	18.8	0.2	0.03	x
1	24.3	7.12	7.83	35.1	x	35.4	14.7	4.5
2	23.7	7.98	3.28	17.0	13.5	23.1	7.5	1.7
4	23.1	8.51	7.35	41.7	14.0	34.6	6.4	0.7
19	22.5	8.45	3.24	17.6	10.4	29.8	5.6	0.9
23	20.0	8.5	3.33	17.6	14.6	39.3	8.6	1.6
27	19.4	8.15	3.27	17.2	9.4	34.1	4.5	0.4
33	20.0	8.15	3.15	17.5	7.0	27.7	3.3	0.3
T = 53 °C, P = 100 bars, CO_2 saturated								
34	19.1	4.85-5.0	3.38	18.3	25.6	67.8	25.2	10.7
35	18.1	4.85-5.0	3.14	18.2	20.6	56.4	20.7	9.8
36	17.2	5.06	3.11	18.2	20.0	51.6	19.6	10.5
37	16.6	5.07	3.23	18.5	22.9	58.3	22.3	12.3
40	15.9	4.99	3.30	18.5	22.7	65.5	22.6	14.2
43	15.3	5.06	3.13	17.9	28.6	77.4	27.7	16.7
46	14.7	5.04	3.17	18.5	22.7	66.6		
49	14.3	5.02	3.12	18.3	24.3	70.7	25.0	17.2
53	13.6	4.98	3.07	18.6	20.1	58.6	20.6	15.3
56	13.1	4.97	3.18	19.7	17.1	54.0	18.3	14.0
60	12.2	5.02	3.09	18.1	29.8		31.7	23.9
63	11.8	5.1	3.01	18.6	16.9	52.1	18.0	14.7
69	11.3	5.02	2.99	18.0	21.3	68.8	22.9	20.6
75	10.8	5.02	2.40	14.5	22.8	73.6	24.8	22.7
T = 150 °C, P = 100 bars, CO_2 saturated, 2x dilution of residual fluid with fresh AN10(10x) solution								
102	20.2	4.95	2.06	8.98	25.3	38.2	12.9	11.8
103	19.8	5.05	1.72	0.90	100.4	485	18.1	107
103	19.3	5.00	1.71	0.94	104.0	769	15.6	116
105	18.8	4.96	1.79	0.89	113.7	1120	19.3	132
108	18.4	4.95	1.88	0.85	99.3	1401	6.3	134
111	18.0	4.98	1.85	0.89	104.8	1629	7.5	145
116	17.5	5.04	1.56	0.78	91.2	1602	5.7	132
119	17.1	5.04	1.91	0.86	107.6	1928	7.1	154
123	16.6	5.12	1.89	0.88	106.0	2024	7.6	160
136	16.2	5.17	1.08	0.58	71.5	1407	4.5	112
143	15.8	5.1	1.93	0.86	110.6	2334	4.9	179
147	15.3	5.11	1.93	0.96	119.5	2557	2.9	204
150	14.8	x	1.75	0.92	111.1	2378	6.9	188

Table 4.4. Bulk chemical analysis of sample (solids) 2-41R.

Table 4-4: Bulk Chemical Analysis* of Sample (Solids) 2-41R

Analyte	Conc.	Units	Method
SiO2	66.17	%	*FUS-ICP*
Al2O3	7.22	%	*FUS-ICP*
Fe2O3	0.23	%	*FUS-ICP*
FeO	0.2	%	*TITR*
MnO	0.02	%	*FUS-ICP*
MgO	0.36	%	*FUS-ICP*
CaO	9.12	%	*FUS-ICP*
Na2O	2.95	%	*FUS-ICP*
K2O	1.38	%	*FUS-ICP*
TiO2	0.233	%	*FUS-ICP*
P2O5	0.1	%	*FUS-ICP*
CO2	0.15	%	*IR*
C-Total	0.09	%	*IR*
Total S	4.41	%	*IR*
LOI	8.81	%	*FUS-ICP*
Bulk Tot	~101	%	

Analyte	Conc.	Units	Method	Analyte	Conc.	Units	Method
Au	17	ppb	*INAA*	Sc	3	ppm	*INAA*
Ag	< 0.5	ppm	*MULT INAA / TD-ICP*	Se	< 3	ppm	*INAA*
As	< 2	ppm	*INAA*	Ta	< 1	ppm	*INAA*
Ba	1510	ppm	*MULT INAA/FUSICP*	Th	12.2	ppm	*INAA*
Bi	< 2	ppm	*TD-ICP*	U	1.4	ppm	*INAA*
Br	< 1	ppm	*INAA*	W	40	ppm	*INAA*
Cd	< 0.5	ppm	*TD-ICP*	Zn	16	ppm	*TD-ICP*
Co	6	ppm	*INAA*	La	26.5	ppm	*INAA*
Cr	8	ppm	*INAA*	Ce	50	ppm	*INAA*
Cs	1.3	ppm	*INAA*	Nd	25	ppm	*INAA*
Cu	24	ppm	*TD-ICP*	Sm	4.6	ppm	*INAA*
Hf	3.6	ppm	*INAA*	Eu	0.9	ppm	*INAA*
Hg	< 1	ppm	*INAA*	Tb	< 0.5	ppm	*INAA*
Ir	< 5	ppb	*INAA*	Yb	2.3	ppm	*INAA*
Mo	3	ppm	*TD-ICP*	Lu	0.35	ppm	*INAA*
Ni	4	ppm	*TD-ICP*	Be	< 1	ppm	*FUS-ICP*
Pb	23	ppm	*TD-ICP*	Sr	1106	ppm	*FUS-ICP*
Rb	30	ppm	*INAA*	V	22	ppm	*FUS-ICP*
S	6.08	%	*TD-ICP*	Y	24	ppm	*FUS-ICP*
Sb	< 0.2	ppm	*INAA*	Zr	153	ppm	*FUS-ICP*

**all analyses performed by Actlabs*

5. PRELIMINARY MODELING OF FIELD-SCALE CO_2-BRINE-ROCK INTERACTION

We present in this section the setup and results of reaction-path geochemical simulations that consider the chemical reaction between formation water, sediments, and CO_2, without considering transport. These simulations, together with the experimental results presented earlier, serve as a basis for the development of more complex reactive transport simulations at field scales and over a typical injection period of 30 years, presented later in Section 6.

5.1 Input Mineralogical and Brine Composition Data

The initial mineralogy of the reservoir formation considered in all simulations was the same as that discussed in Section 3 and shown in Table 3.1. Because no fluid samples were recovered from this formation, the composition of the deep brine had to be estimated, as discussed previously in Section 3.2.2. The same brine composition as shown for the An10(10x) evaporation case in Table 3.3 was used, with some adjustments, as follows. First, the equilibration temperature was raised from 50°C (Table 3.3) to 54°C for better consistency with the temperature at which experiments (53°C) and multiphase flow simulations (~54°C) were conducted. Also, because as the experimental results suggested a significant amount of Fe residing in chlorite, a chlorite containing 30 mol% Fe/(Fe+Mg) was used in the simulations, instead of the pure chlorite that was used to estimate the brine composition. Doing so essentially did not change the initial brine composition shown on Table 3.4 for the An10(10x) case, except for the trace concentration of Al, which decreased by a factor of 4.

The computed mineral saturation indices as a function of temperature for the brine reconstructed as described in Section 3, with above-mentioned adjustments, are shown on Figure 5.1. The brine displays close equilibration at 54°C, with many formation minerals and other phases typical for such a system.

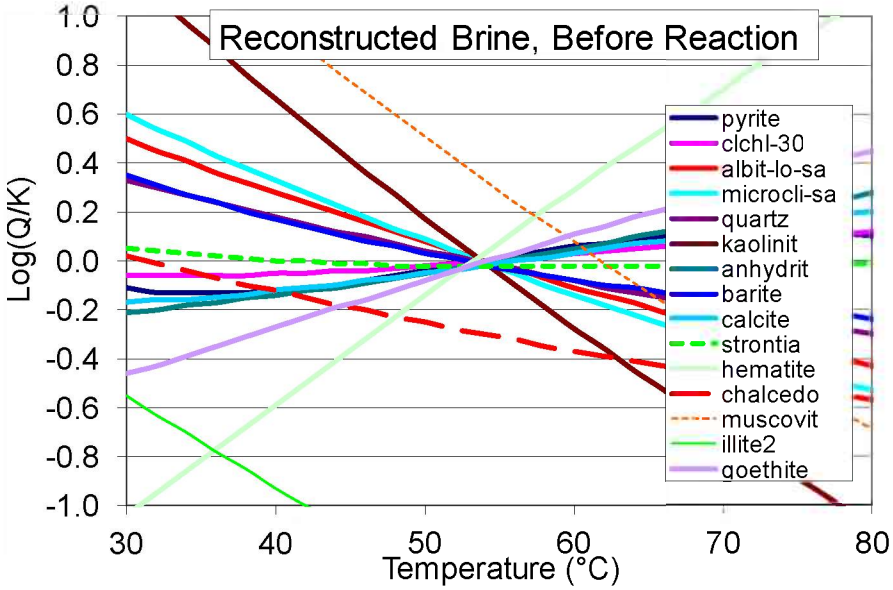

Figure 5.1. Mineral saturation indices computed as a function of temperature for the reconstructed brine composition. Curves for the main formation minerals cluster near equilibrium at the assumed formation

temperature of 54°C.

5.2 Modeling Approach

The chemical interactions between brine, CO_2, and the targeted sandstone formation were modeled under thermodynamic equilibrium constraints, for a closed system and without effects from flow and transport. This type of analysis was conducted to determine thermodynamic limits of reactions, type and stability of reaction products (secondary minerals), as well as initial rough estimates of porosity change and CO_2 mineral-sequestration potential under limits of thermodynamic equilibrium constraints. These simulations were carried out using program CHILLER (Appendix A3) (Reed, 1982; 1998) and thermodynamic data described in Appendix C.

The simulations involved first saturating the brine-rock system with free phase CO_2 at 54°C and 150 bar, up to a brine/CO_2 volume ratio in the range of typical CO_2 residual gas saturation (around 30%), then reacting the low-pH brine/CO_2 system with the rock mineral assemblage in incremental steps, up to a large rock to brine ratio of about 10:1. At each reaction step, all thermodynamically possible reaction products (secondary minerals) were evaluated. Minerals that formed but did not belong to the geochemical system on the grounds of slow reaction kinetics at the considered temperature (such as high-temperature metamorphic minerals) were not allowed to form. This applied to quartz, which was not allowed to precipitate to favor the formation of chalcedony, a typical silica polymorph controlling the solubility of silica in low-temperature formation waters (e.g., Kharaka and Mariner, 1989). Also, when the primary minerals "titrated" into the brine/CO_2 system reached saturation levels, their titration was stopped as long as their saturation indices remained above saturation limits (to mimic dissolution rates dropping to zero at equilibrium).

Two simulations were conducted, one allowing the secondary carbonate mineral dawsonite ($NaAlCO_3(OH)_2$) to form (Figure 5.2, (a)–(c)) and the other excluding this mineral (Figure 5.2, (d)–(f)) on the basis that it has almost never been observed in experiments nor in the field under conditions similar to those expected during a CO_2 sequestration process. Alunite ($KAl_3(SO_4)_2(OH)_6$) was not included in these initial simulations. However, similar simulations carried out with fluids from the laboratory experiments (Section 4.3) suggested that this sulfate mineral may form at low pH. For this reason, alunite was included in reactive transport simulations discussed later in Section 6.

5.3 Simulation Results

The reaction path simulations show that under thermodynamic equilibrium, and without considering transport, the brine pH upon reaction with CO_2 drops to a value near 4, but then increases to about 5.5 in the case with dawsonite, and near 6 in the case without dawsonite, as the formation minerals react with the brine acidified with carbonic acid from CO_2 dissolution (Figure 5.2, (a) and (d)). Calcite dissolves but reaches equilibrium relatively quickly at a rock/water mass ratio of about 0.1 in both simulated cases, because the dissolution of this carbonate mineral by CO_2 is self-limiting. The reacted brine comes close to equilibration with anhydrite only at the end of the simulation, despite rising SO_4 concentrations (Figure 5.2, (b) and (e)), because Ca (from dissolving plagioclase) is consumed by ankerite and later calcite precipitation. Chalcedony, kaolinite, and siderite (then replaced by ankerite early on) form by the dissolution of primarily plagioclase and Fe-chlorite. At a rock-to-water ratio mass of about 1, dawsonite

becomes thermodynamically stable. If this mineral is not allowed to form, albite and later dolomite are predicted to form, and CO_2 is consumed (mineralized) to a lesser extent (compare Figure 5.2, (a) with (d)). Additional tests excluding dolomite were run; they show that magnesite then becomes the thermodynamically stable phase instead of dolomite; if removing magnesite, then Mg-clays become the next favored Mg phases, becoming very close to saturation at the end of the simulations. Therefore, the generalized (not stoichiometric) reactions for this system can be summarized as follows:

Fe-Chlorite + Plagioclase + CO_2 ➔

Siderite/Ankerite/Calcite + Kaolinite + Dawsonite + Chalcedony + (Mg, CO_3)

and/or

Fe-Chlorite + Plagioclase + K-feldspar + CO_2 ➔

Siderite/Ankerite/Calcite + Kaolinite + Albite + Chalcedony + Dolomite/Magnesite/Mg clays

It should be noted that until the point when dawsonite is predicted to become thermodynamically stable and is allowed to form, or if this mineral is not allowed to form, the computed porosity change for this system is negligible (Figure 5.2(a) and (d)). If dawsonite is allowed to precipitate, the net volume change of the reaction is significantly increased by the destabilization of albite and precipitation of significantly more silica (as chalcedony in this case) than when dawsonite is not allowed to form (e.g., $NaAlSi_3O_{8(albite)} + H_2O + CO_2 = NaAlCO_3(OH)_{2(dawsonite)} + 3\ SiO_{2(chalcedony)}$). This results in an absolute porosity decrease of about 0.01 – 0.02 towards the end of the simulation at a rock/water mass ratio near 10 (Figure 5.2(a)).

Obviously these simulations do not involve flow/transport or kinetic constrains other than allowing (or not) the formation of some phases. For this reason, more complex simulations of actual CO_2 injection at field scales and under kinetic constraints are presented in the next section.

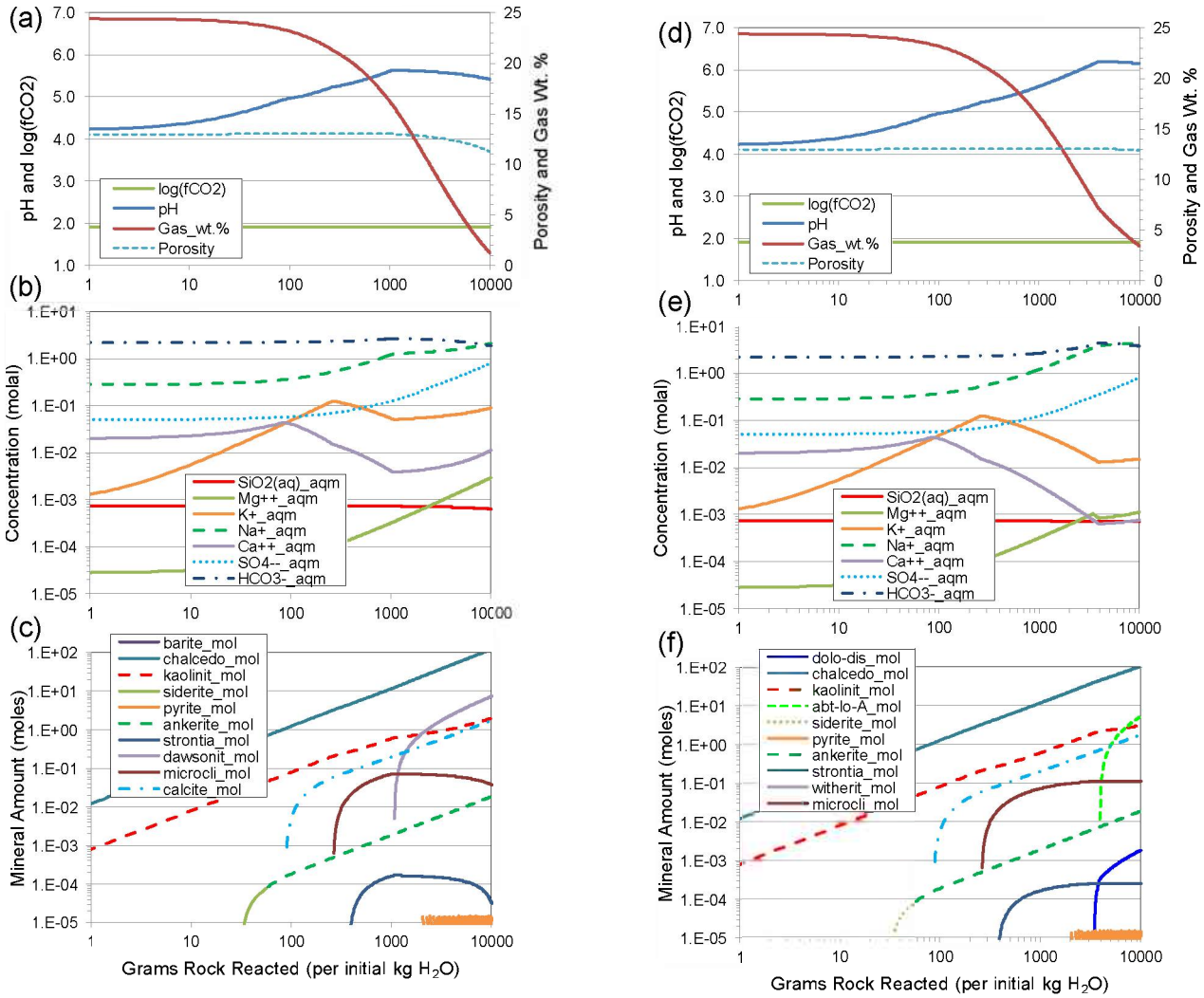

Figure 5.2. Simulated reaction of sediments ("rock"), brine and CO_2 at 54°C and 150 bar, for cases allowing dawsonite to form (a–c) and excluding this mineral (d–e).

6. REACTIVE TRANSPORT MODELING

As a follow up to the reaction path simulations presented in Section 5, which did not involve transport, the injection of CO_2 into the targeted sandstone formation was simulated using a full reactive transport model. These simulations considered multiphase fluid flow at field scales with hydrological inputs consistent with the model presented in Section 2, coupled to multicomponent reactive transport. Kinetic constraints were applied to mineral precipitation and dissolution, and simulated changes in porosity were coupled to flow. For simplicity, thermal effects of injection were not taken into account, as these effects are small and not expected to change the outcome of the reactive transport simulations.

Two-dimensional (2D) vertical *X-Z* reactive transport models were set up using the same hydrological parameters as the base-case multiphase fluid-flow model presented in Section 2. The first reactive

transport simulations were performed using a radial-symmetric 2D mesh, as will be discussed in Section6.1. The advantage of such an approach is the numerical accuracy of flow computations near the well head when simulating injection. However, such radial symmetric models cannot account for any tilt in the modeled geologic layers. Therefore, to investigate reactive effects away from the injection well in the case of a tilted formation, a second set of injection simulations were carried out on an inclined 2D cross section, which is discussed in Section 6.2. This second model was taken as a slice of the 3D multiphase flow model presented in Section 2. The advantage of such an inclined 2D model is that it can account for buoyancy flow of supercritical CO_2 along tilted geologic strata. However, flow near the injection well cannot be captured as well as with a radial 2D model or a full 3D model. It should be noted that reactive transport simulations in full 3D were not attempted, because the large number of model grid blocks required for such simulations (without decreasing resolution) is computationally prohibitive.

All reactive transport simulations were carried out using program TOUGHREACT V2.0 (Xu et al., 2011) and V3 (Sonnenthal et al., in prep.) (Appendix A) with thermodynamic and kinetic data presented in Appendix C.

6.1 2D Radial Symmetric model

6.1.1 Hydrological Setup and Parameters

The model was set up as a two-dimensional (2D) vertical *X-Z* radial numerical mesh, as shown in Figures 6.1 and 6.2. CO_2 injection takes place within the bottom 60 m of a well (radius 0.08 m) penetrating a 150 m thick sandstone formation assumed impermeable at its top and bottom. The numerical mesh comprises 7500 grid blocks, including 100 horizontal layers, each of a constant 2 m thickness, with increasing grid spacing in the horizontal direction starting at a well radius of 0.08 m, then increasing progressively away from the well (Figure 6.2). The ambient conditions (150 bar at the top of the formation and constant 54^{o}C temperature), formation thickness, porosity, permeability, and capillary characteristics, as well as the CO_2 injection conditions (1 MMt/y for 30 years) were taken the same as assumed for the base-case 3D multiphase flow model (see Sections 2.5, 2.6, and 2.7). Initial hydrostatic pressure conditions, averaging a pressure of ~158 bar within the modeled domain, were set throughout the model domain prior to running injection simulations.

A maximum time step of 6 hours was adopted, below the Courant limit computed for aqueous-phase flow. For simplicity, hydrological properties were assumed homogenous throughout (see Section 2.5). The lateral model boundary was located far away from the injection well (10 km) and assumed open, whereas the top and bottom boundaries were assumed closed. Hydrodynamic dispersion was not explicitly modeled. Numerical dispersivity values can be roughly approximated by the model grid-block sizes ($\Delta x/2$ in the *X* direction and $\Delta z/2$ in the *Z* direction).

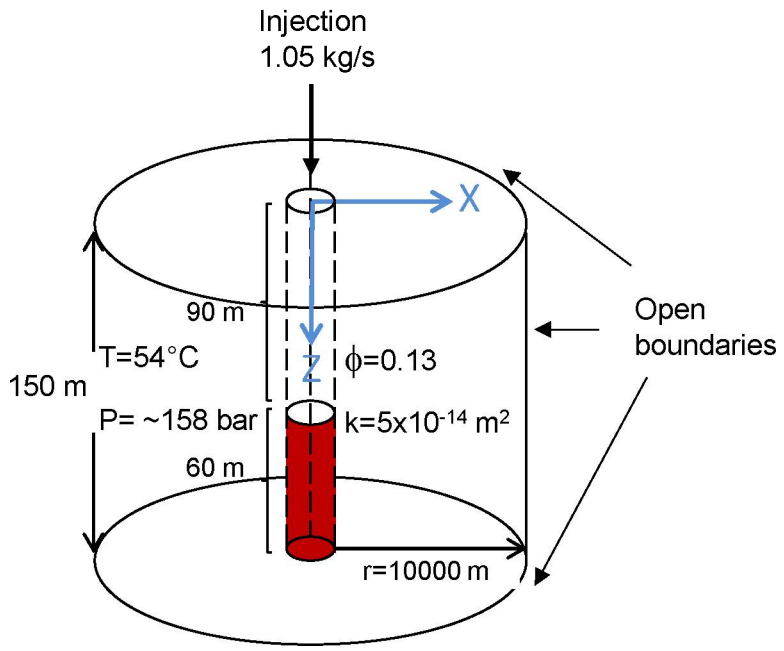

Figure 6.1. Illustration of the radial 2D reactive transport model setup (not to scale). The injection interval (60 m) is shown in red.

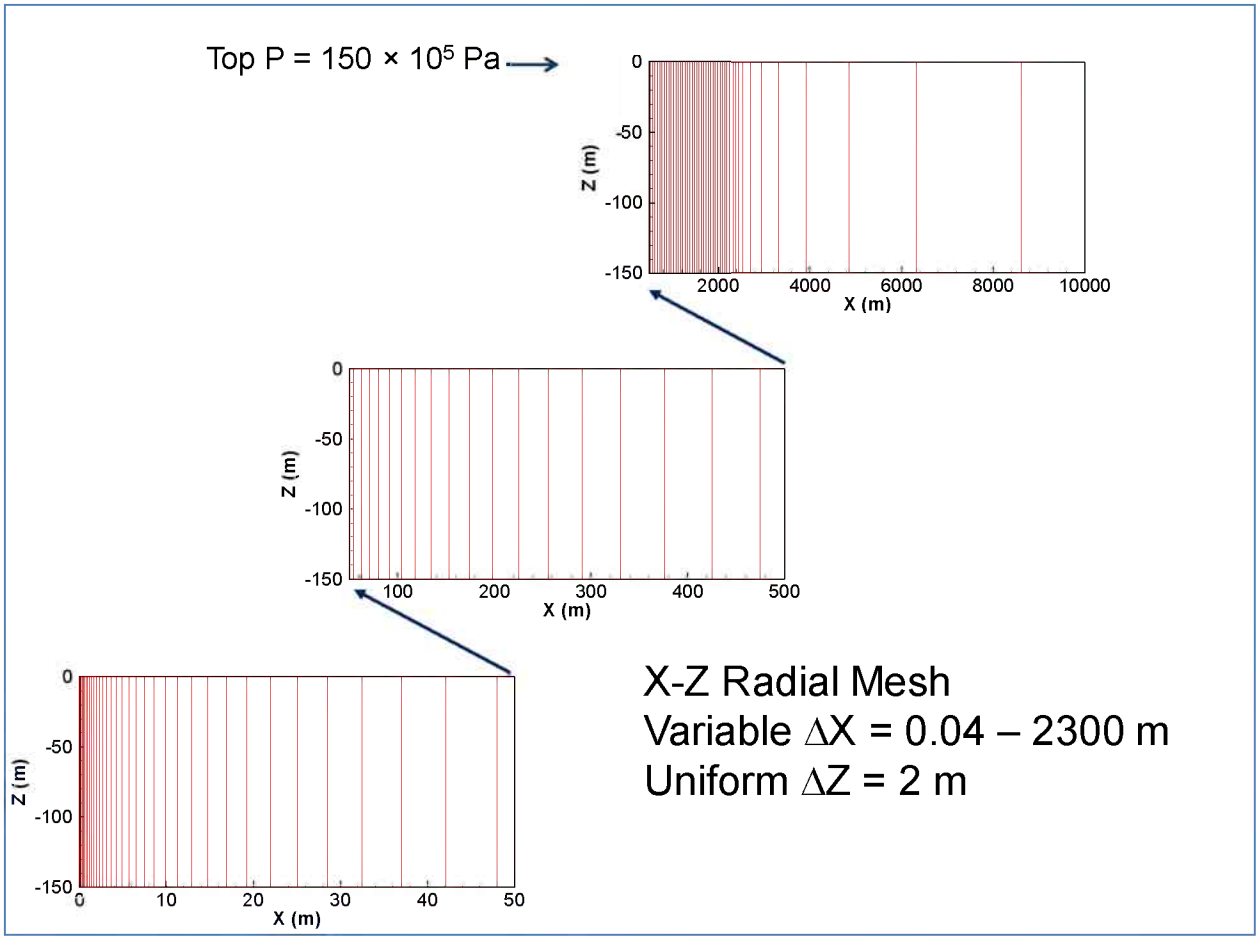

Figure 6.2. Variable discretization of the radial model in the horizontal direction. The vertical discretization is constant comprising 100 uniformlayers (not shown). The center of the injection well is located at X = 0.

6.1.2 Input Water Chemistry, Mineralogy, and Modeled Geochemical Processes

Initial conditions of brine chemistry and formation mineralogy were determined as described in Section 3. However, because the Mg concentration of the brine (~0.7 ppm, Table 3.4) seemed low in comparison to data reported for other typical brines (e.g., Drever, 1997, Kharaka and Mariner, 1989), the initial Mg concentration of the brine was raised to 50 ppm. Most reactive transport simulations were run with this higher Mg concentration. However, experimental results (pre-equilibrating the targeted sandstone with brine without CO_2 added, Section 4.1) obtained after conducting most of the modeling work indicated that the Mg concentration could indeed be in the range of ~0.1–1 ppm. Because these pre-equilibration experiments lasted only up to about 50 days, the possibility of higher Mg concentrations still cannot be ruled out. In any case, a few additional simulations were subsequently run using the original, low, Mg concentration, and showed no significant differences in results and did not affect the conclusions of this modeling effort.

The reactive transport simulations considered reactions between supercritical CO_2, the same aqueous species as considered in the reaction-path simulations (Table 3.3), and primary and potential secondary minerals shown in Table 6.1. The abundance of primary minerals (also shown in Table 6.1) was taken as the same for previous reaction-path simulations (Table 3.1), except that the reported trace amount of illite was replaced by the same trace amount of muscovite, with illite then specified as a potential secondary mineral. This change was made to improve the steadiness of the ambient geochemical system, as described in Section 6.1.3.

Reactive processes modeled included aqueous complexation and CO_2 dissolution/exsolution under equilibrium constraints, and mineral dissolution and precipitation under kinetic constraints (Appendix C), except for anhydrite, which was assumed to react at equilibrium (fast reaction). The specific surface area of minerals (Table 6.1), which are required for the computation of effective reaction rates (Appendix C), were derived assuming spherical grains of 100-micron diameter. For some minerals, these surface areas were decreased by two orders of magnitude to yield a steady ambient geochemical system, as described in Section 6.1.3.

For all simulations, the precipitation or dissolution of minerals was coupled to porosity (by directly relating reacted moles of minerals to solid volume through the molar volume of each mineral). The resulting change in porosity was coupled to permeability using the Kozeny-Carman relationship, and to capillary pressure through Leverett scaling.

Table 6.1. Initial primary minerals (and amounts) considered in reactive transport simulations, and secondary phases allowed to form. Initial specific surface areas assumed for all minerals reacting under kinetic constraints (Appendix C) are also listed.

Primary Phases	Initial Volume Fraction	Specific Surface Area m2/m3	Potential Secondary Phases	Surface Area m2/m3
Anhydrite	0.0089	*	Jarosite[2]	6.00E+04
Calcite	0.0097	6.00E+04	Alunite	6.00E+04
Quartz[1]	0.5768	6.00E+04	Dolomite	6.00E+04
Pyrite	0.0002	6.00E+04	Ankerite	6.00E+04
K-feldspar	0.1341	6.00E+04	Strontianite	6.00E+04
Muscovite	0.0001	6.00E+02	Chalcedony	6.00E+04
Fe-Chlorite	0.0001	6.00E+02	Siderite	6.00E+04
Plagioclase[1] (An10)	0.2700	6.00E+04	Magnesite[2]	6.00E+04
Kaolinite	0.0001	6.00E+04	Dawsonite	6.00E+04
Hematite	0.0002	6.00E+04	Albite	6.00E+02
			Illite	6.00E+04

* Reacting at equilibrium, not needed
[1] Allowed to dissolve only
[2] Never forms

6.1.3 Initial Ambient Geochemical System

When simulating the perturbation of a natural geochemical system, a prerequisite for a sound model is that the geochemical state of the modeled system under ambient (unperturbed) conditions should remain as steady as possible for an extended period of time (typically at least centuries or more) and keep

predicting solid-phase and water compositions that are consistent with field observations. Not being able to achieve such steady or pseudo-steady conditions often reflects a problem with the geochemical system conceptualization and/or input thermodynamic and kinetic data.

To test the modeled initial geochemical system, reactive transport simulations using TOUGHREACT were run without CO_2 injection for a period of 1000 years at 54°C, 150 bar, and the initial geochemical system described in Section 3. In doing so, it was found that when illite was specified as a primary mineral, it would dissolve to form muscovite, with resulting pH shifts very sensitive to the initial amounts of these two minerals. Because illite would be expected to form (from feldspar alteration) rather than dissolve, it was replaced by muscovite as an initial mineral, which is quite plausible given that this mineral is typically present in deep sandstone formations and often difficult to distinguish from illitic phases. Doing so resulted in a more stable pH, however still rising significantly with time. Lowering the effective reaction rate of muscovite, albite, K-feldspar and chlorite by two orders of magnitude (by correspondingly decreasing the surface area of these minerals) yielded a nearly steady pH for at least 1000 years and consistent ambient reaction trends (e.g., plagioclase altering to albite and calcite). In doing so, after 1000 years, all the modeled aqueous components remained essentially steady, except for K, which decreased by a factor of about 4 (from muscovite precipitation), and Si, which rose to the solubility of chalcedony, which was deemed perfectly acceptable, especially considering that CO_2 injection would be simulated for a comparatively short 30-year period.

6.1.4 2D Radial Reactive Transport Model Results

CO_2 injection simulations were run for a total injection period of 30 years. The injected CO_2 plume is predicted to extend to about 1000 m from the injection well after 4 years, and 2000 m after 30 years of injection (Figure 6.3). Results of these simulations are generally consistent with the previous reaction-path modeling results (Section 5) in terms of main reactions. The pH quickly drops to values near 5, and remains near this value within the bulk of the 2-phase plume, as little buffering occurs from reaction of CO_2 with the sandstone. The predicted most reactive primary minerals are plagioclase and Fe-chlorite. Plagioclase dissolves to form mostly chalcedony and dawsonite, with calcite precipitating only in a small spot where plagioclase dissolution is at maximum, at the bottom edge of the 2-phase plume (Figure 6.4). Otherwise, calcite is predicted to dissolve throughout the 2-phase plume. Anhydrite precipitates mostly from calcite dissolution, and to a lesser extent from the dissolution of plagioclase. Fe-chlorite dissolves, resulting in the precipitation of ankerite and kaolinite (Figure 6.5). Other minerals react in much lesser (insignificant) amounts. Very small amounts of dolomite are predicted to form only at the edge of the single-phase CO_2 (Figure 6.6). During the first two years of injection, similarly small amounts of alunite precipitate at the edge of the single-phase zone up to ~200 m from the well head, but then mostly redissolve, remaining only up to ~25 m from the well head after 30 years (Figure 6.6). Overall, these reactions result in a very small volume increase, resulting in a maximum absolute porosity drop of only about 0.3% (Figure 6.4, upper left).

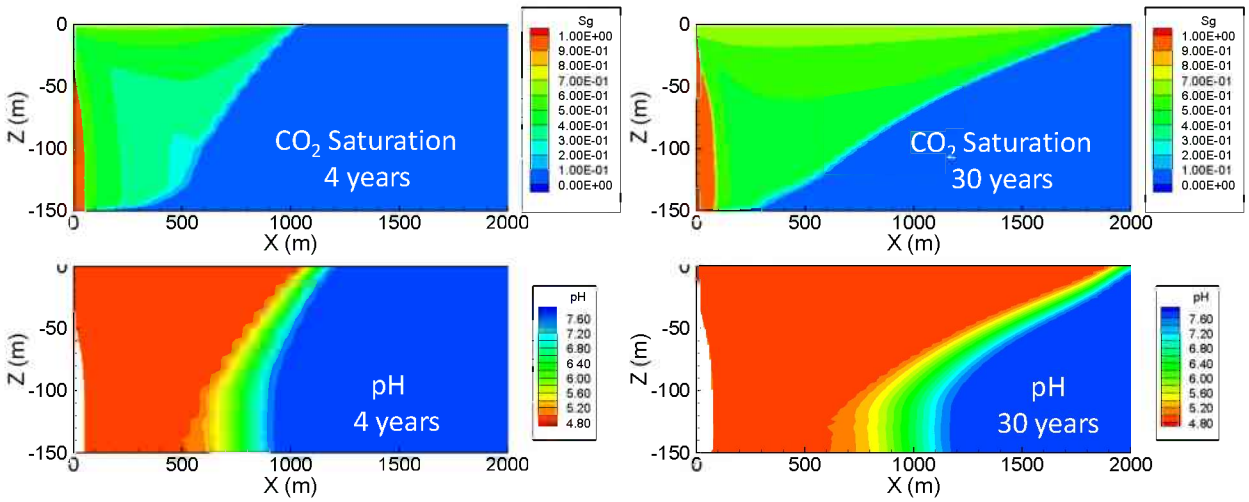

Figure 6.3. Predicted CO_2 (physical) saturation and plume pH after 4 and 30 years of injection.

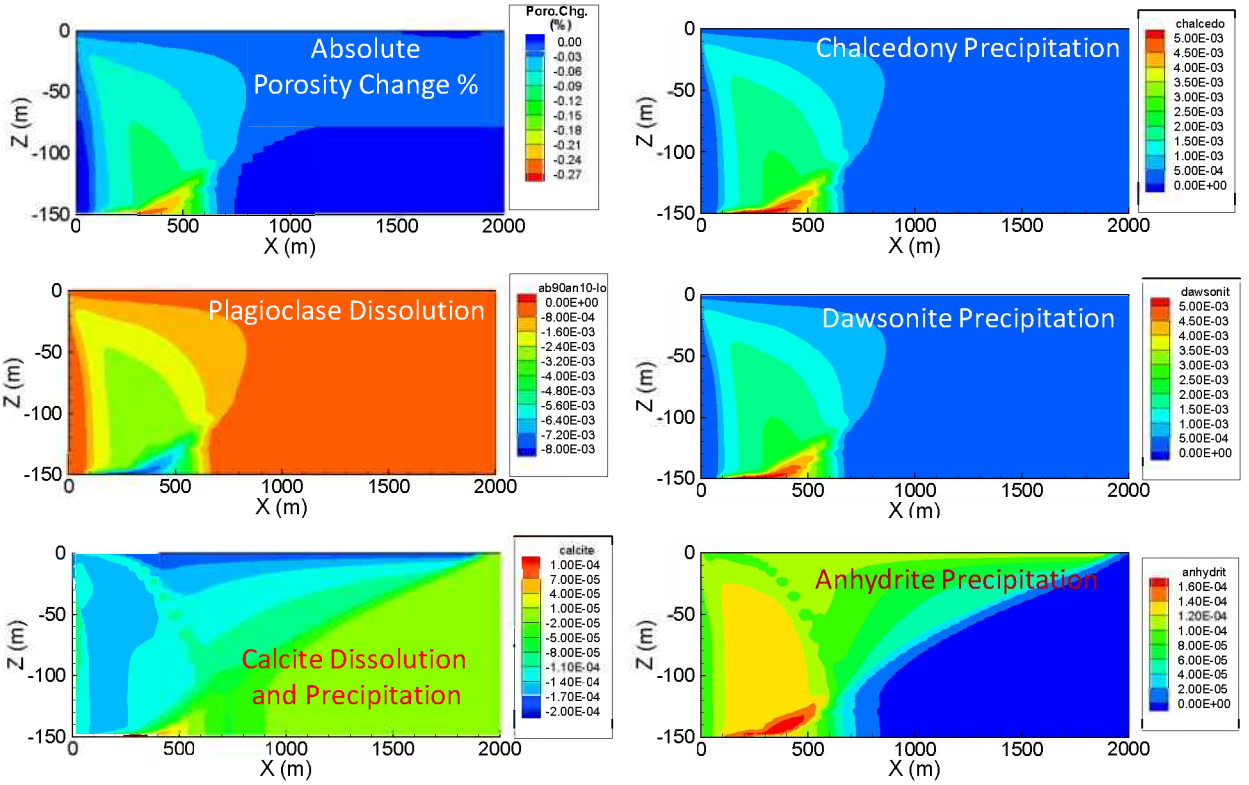

Figure 6.4. Predicted absolute porosity change (as the computed porosity minus the initial porosity, in percent; upper left figure) and computed volume fraction change of main dissolving and precipitating minerals after 30 years.

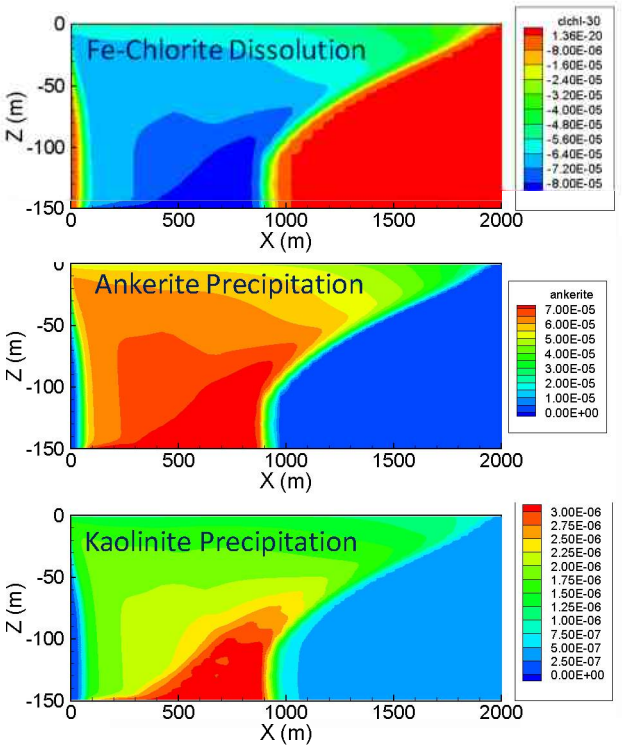

Figure 6.5. Predicted computed volume fraction change of other key dissolving and precipitating minerals after 30 years.

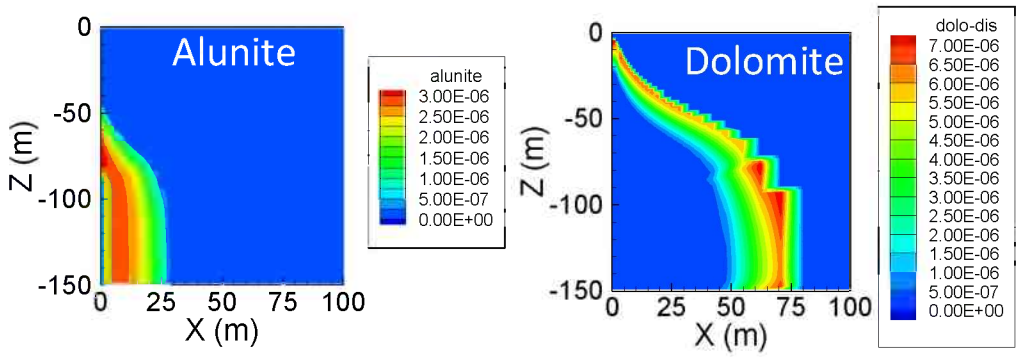

Figure 6.6. Predicted insignificant precipitation of Alunite near the well head and dolomite at the fringe of the single-phase CO_2 plume after 30 years.

When dawsonite is not allowed to form, plagioclase dissolves to a lesser extent than when dawsonite is allowed to precipitate (Figure 6.7). About 10 times more kaolinite precipitates, and the porosity change is insignificant (not shown). This is consistent with the previous reaction-path simulations which show a noticeable porosity decrease only when dawsonite is allowed to precipitate (Figure 6.2). The calcite dissolution/precipitation behavior essentially does not change, but because less plagioclase dissolves, somewhat less anhydrite is predicted to precipitate (Figure 6.7).

A simulation was also run increasing the residual saturation of CO_2 from originally 5% (Section 2.5, see also Table 2.7) to 25%, to investigate the effect of longer fluid residence time on chemical reactions. Obviously, increasing the residual saturation of CO_2 affects the CO_2 migration extent and plume shape (Figure 6.8). However, because the geochemical system appears to reach a near-equilibrium state relatively quickly, increasing the residual saturation does not affect either the pH trend and magnitude (Figure 6.8), nor the mineral precipitation/dissolution behavior (and accompanying porosity change) compared to the original case at 5% residual gas saturation.

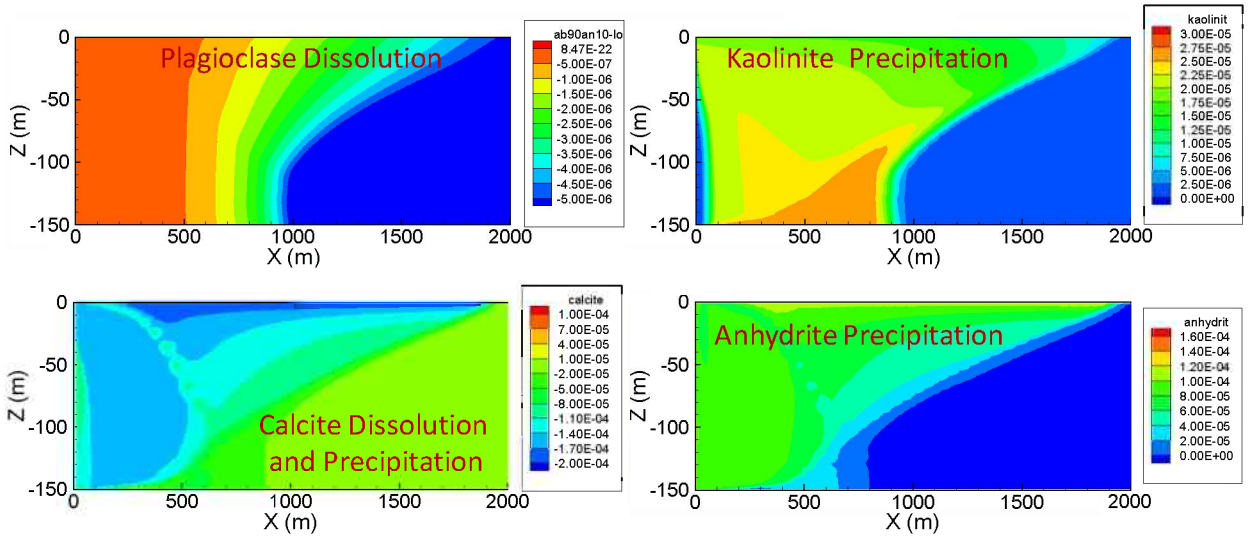

Figure 6.7. Computed volume fraction change of main dissolving and precipitating minerals for the case when dawsonite is not allowed to precipitate, after 30 years (compare to Figures 6.4 and 6.5; the total porosity change is negligible).

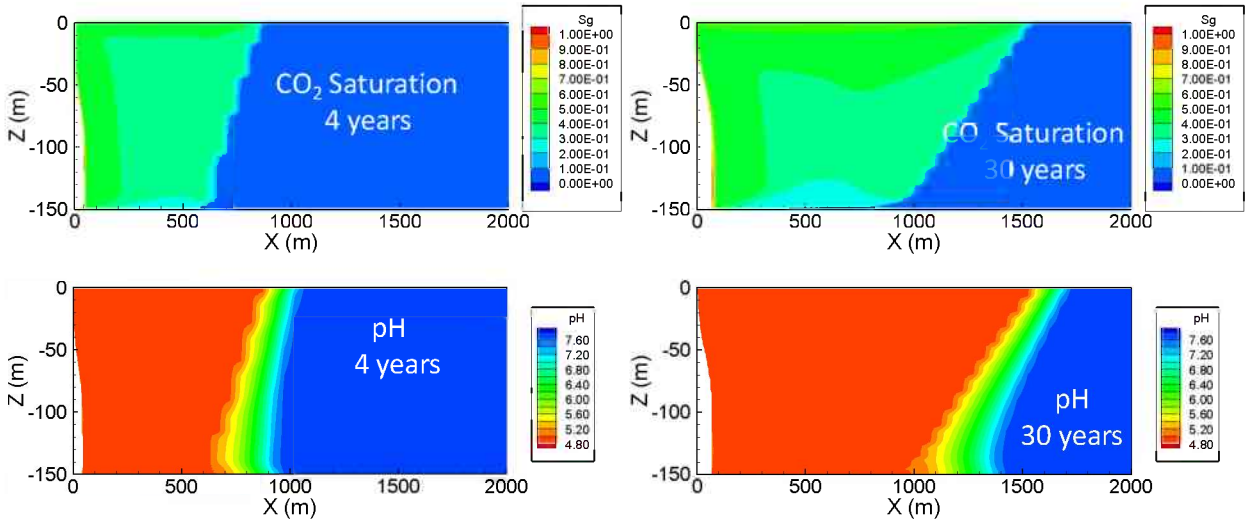

Figure 6.8. Predicted CO_2 (physical) saturation and plume pH after 4 and 30 years of injection, for a case when the residual saturation of CO_2 is increased from the original 5% to 25% (the single-phase CO_2 zone is blanked out).

6.2 Vertical 2D Inclined Reactive Transport Model

6.2.1 Model Setup and Input Parameters

The model was set up as a two-dimensional (2D) inclined *X-Z* numerical mesh, as shown in Figure 6.9, with a constant total depth (*Y*) of 1 km (i.e., thickness of vertical slice). Injection characteristics were specified to mimic as well as possible the behavior of the radial 2D model for a 1 MMt/y injection rate. This model is essentially a 2D "slice" of the 3D multiphase fluid flow model presented in Section 2. CO_2 injection is taking place within the bottom 56 m of an injector (represented with gridblock size 2×2 m) penetrating the 152 m thick targeted sandstone formation, assumed impermeable at its top and bottom. The formation itself is inclined at 8°. The numerical mesh comprises 16,630 grid blocks and 32,904 connections between them. The smallest gridblock size is 2×2 m at the injection location, with increasing grid spacing in the horizontal (away from the well) and vertical (bottom up) directions (Figure 6.9). The ambient conditions (150 bar at the top of the formation and constant 54°C temperature), formation thickness, porosity, permeability, and capillary characteristics, as well as the CO_2 injection conditions (1 MMt/y for 30 years) were taken the same as assumed for the base-case 3D multiphase flow model (Section 2). Initial hydrostatic pressure conditions were set throughout the model domain prior to running injection simulations.

As for the radial 2D model, a maximum time step of 6 hours was adopted, below the Courant limit computed for aqueous-phase flow. For simplicity, hydrological properties were assumed homogenous throughout (Section 2.5). The lateral model boundary was located far away from the injection well (20 km) and assumed open, whereas the top and bottom boundaries were assumed closed. Hydrodynamic dispersion was not explicitly modeled. Numerical dispersivity values can be roughly approximated by the model grid-block sizes ($\Delta x/2$ in the *X* direction and $\Delta z/2$ in the *Z* direction).

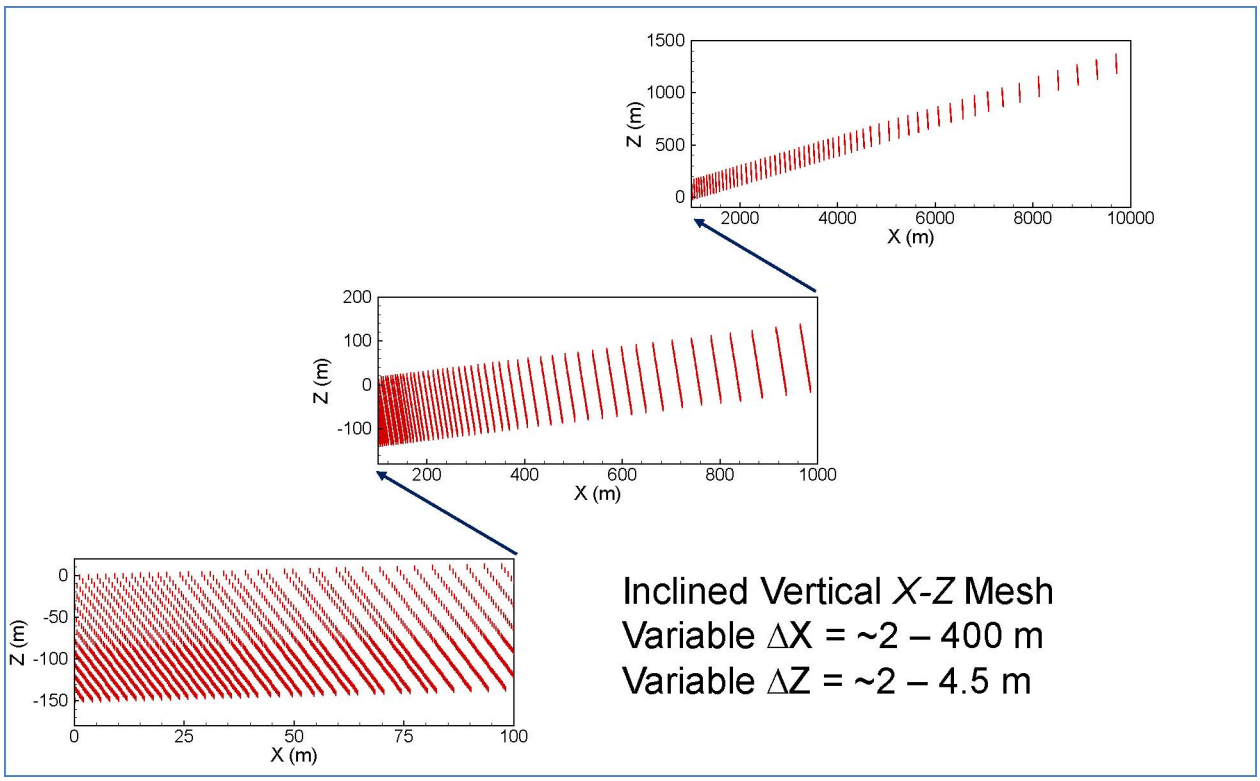

Figure 6.9. Variable discretization of the inclined 2D model in both the horizontal and vertical direction. The injection well is located at $X = 0$.

Geochemical inputs for this model were the same as for the previous 2D radial symmetric model (Section 6.1), including dawsonite as a potential secondary mineral. Unlike in the previous model, an additional clay mineral (Na-montmorillonite) was added as a potential secondary mineral (because a review of the fluid chemistries computed with the previous model suggested that this phase could form). However, only very small amounts of this mineral were predicted to precipitate (volume fraction < 10^{-6}).

6.2.2 Vertical 2D Inclined Reactive Transport Model Results

Because of buoyant flow, the CO_2 plume migrates up-dip further than it does down-dip (Figure 6.9, top), a process which cannot be captured with the 2D symmetric radial model presented earlier (Section 6.1). The simulated trends of pH, mineral dissolution and precipitation, and their resulting effects on porosity and permeability (flow) (Figures 6.1 to 6.4), for this case of an inclined geologic formation, are essentially the same as predicted earlier using the horizontal radial symmetric 2D model. Geochemical results are also qualitatively similar to those obtained computed using the simple reaction path model discussed in Section 5. After 30 years, minor dissolution of mostly plagioclase and chlorite take place primarily within about 800 m from the well (Figures 6.10 through 6.12). Minor calcite dissolution extends further away from the well, to about 2500 m up-dip and 2000 m down-dip, with more dissolution occurring within the upper part of the formation (Figure 6.10). Some calcite precipitation takes place at the very bottom of the formation where single-phase CO_2 has both migrated away (by buoyancy) then

redissoved. Predicted volume fraction change at 30 years of other key dissolving (e.g., Fe-chlorite) and precipitating minerals (e.g., ankerite and kaolinite) can be seen in Figures 6.11 and 6.12.

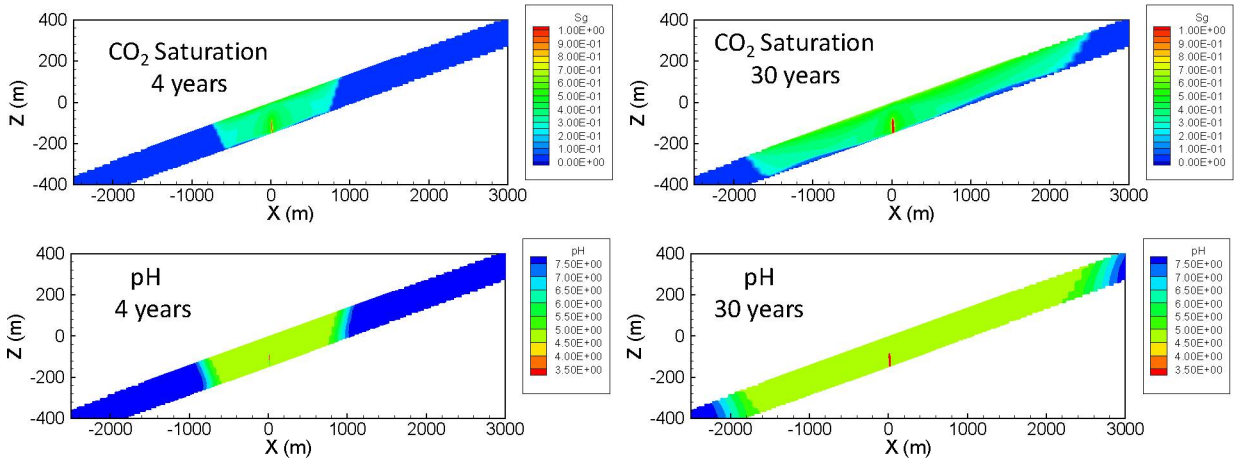

Figure 6.10. Predicted CO_2 (physical) saturation and plume pH after 4 and 30 years of injection (inclined model).

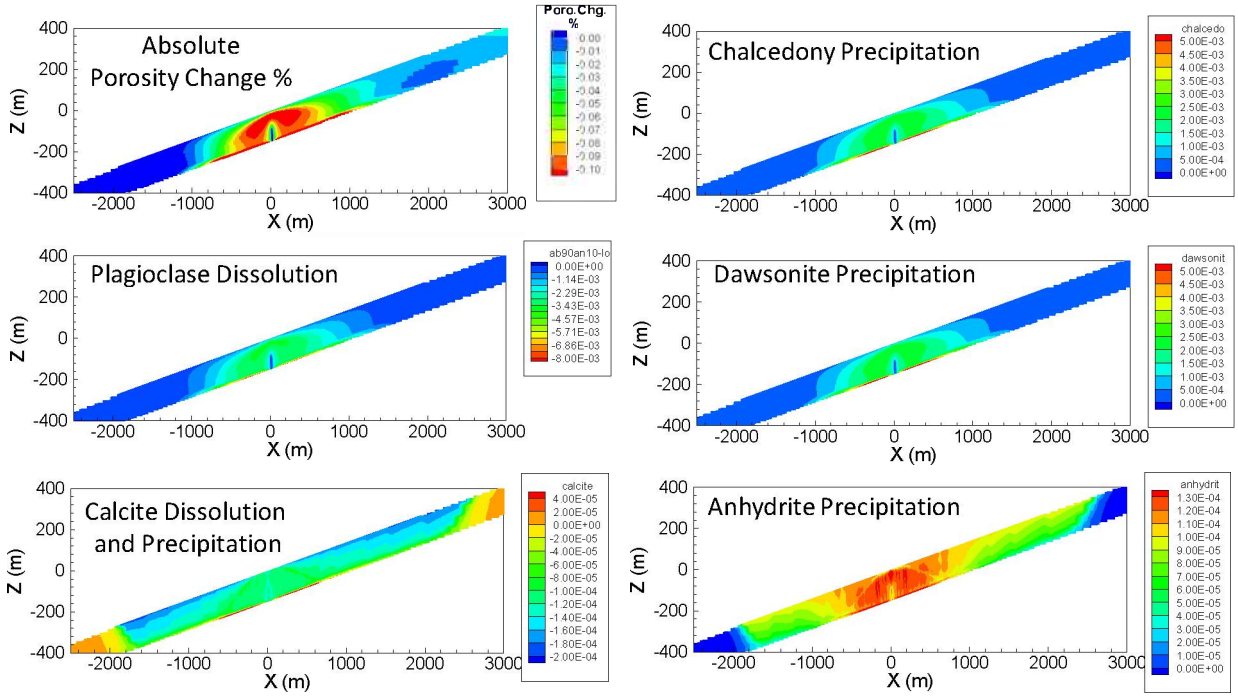

Figure 6.11. Predicted absolute porosity change (as the computed porosity minus the initial porosity, in percent; upper left figure) and computed volume fraction change of main dissolving and precipitating minerals after 30 years (inclined model).

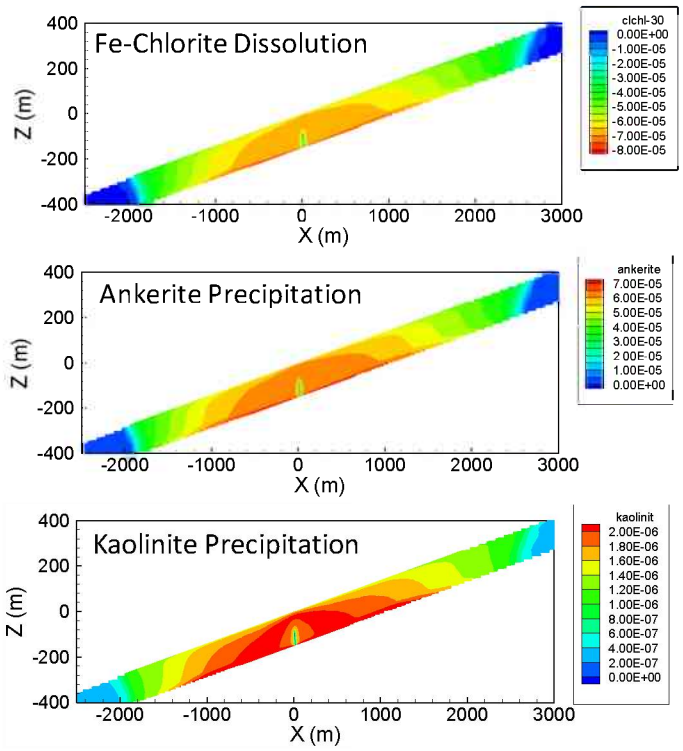

Figure 6.12. Predicted computed volume fraction change of other key dissolving and precipitating minerals after 30 years (inclined model).

7. SUMMARY AND CONCLUSIONS

In this report, we present results from experimental investigations of CO_2-water-rock interactions, and numerical simulations of reactive transport processes associated with the potential injection of CO_2 in deep permeable sandstone formations of the Newark Basin, in Southern New Jersey. The broad objective of the experimental and numerical simulation analyses presented in this report is to help assess the suitability of the Newark Basin as an option for long-term CO_2 geologic storage. More specific objectives include assessing the evolution of the injected CO_2 plume, both in terms of its shape and transient location, estimating the evolution of pressure near the injection well, determining the rate of dissolution of CO_2 and its subsequent mineralization, and investigating their impact on injection rate and storage potential.

The behavior of CO_2 injection in the sandstone formation considered in this study was modeled first using a hydrological multiphase flow model that excludes reactive geochemistry but includes phase-behavior effects of the CO_2-water-salt system. Building on this first model, a reactive transport model was developed that accounts for flow, phase behavior, and aqueous and mineral chemical reactions. Both models are based on the characterization of a sandstone formation encountered in a deep exploration borehole (Tandem Lot Well #1) into the Newark Basin. The properties of this sandstone, tentatively identified as belonging to the Passaic Formation, are expected to be similar to those of the Stockton Formation, which is a target formation for long-term storage in this basin. The Stockton Formation, however, was either not encountered in the Tandem Lot Well #1, or was present at the bottom of the

borehole within an interval too metamorphosed by a nearby intrusion (the Palissade sill) to be considered a good candidate for CO_2 storage at the location of the borehole.

Hydrological parameters were developed based on laboratory measurements on core from the Tandem Lot Well #1 collected at a depth of about 1,277 m in a permeable sandstone horizon. An analytical model was developed to approximate CO_2 and brine-flow processes in this formation to help define the numerical model domain and grid resolution required for the more detailed hydrological and reactive transport numerical models. Both the hydrological and reactive transport modeling analyses were conducted using the TOUGHREACT numerical simulator. TOUGHREACT is a general-purpose thermal-hydrological-chemical process modeling simulator that incorporates both the TOUGH2 multiphase flow simulator and the ECO2N equation of state module for CO_2-water-salt systems. Both hydrological and reactive transport simulations used the ECO2N module assuming isothermal conditions. Isothermal conditions were assumed because of the small natural geothermal temperature variations in the storage reservoir and small temperature perturbations expected from CO_2 injections.

All numerical simulations in this report simulated an injection scenario where 1 MMt/yr of CO_2 was injected for 30 years into the considered sandstone formation, assuming an initial formation pressure near 15 MPa (150 bar) and formation temperature near 54°C. The hydrological models also included a 70-year observation period after the injection period, resulting in a total simulation period of 100 years. A base-case hydrological property set was developed based on various core sample analyses. For evaluating the pressure response to CO_2 injection, a radially symmetric 2D vertical (X-Z) model was used in which the interface between the caprock and the top of the storage formation was assumed horizontal and impermeable. This geometrical simplification was taken to reduce the three-dimensional problem to two dimensions. As a simpler two-dimensional problem, it was possible to use fine gridding near the well to capture the injection pressure effects, which peak in the first few hours of injection. A general three-dimensional model was then used to estimate the extent of plume migration, and for this model two configurations, a horizontal formation and a tilted formation, were investigated. The tilted interface formation represents conditions in the Stockton and other overlying deep formations in the Southeastern part of the Newark Basin. Comparisons of the horizontal and tilted cases helped understand how buoyant fluid motion up the formation dip impacts plume development.

Pressure buildup near the well peaked at about 8 MPa very early in the injection process for the base case. Sensitivity cases with lower permeability were analyzed and found to result in higher injection pressures. However, geomechanical effects may need to be included in the model for much higher injection pressures. For the case of a horizontal formation, free-phase CO_2 was predicted to migrate horizontally about 2,000 m from the well after 30 years of injection, and 3,000 m after another 70 years without injection (100 years total), . Most of the CO_2 (> 80%) was predicted to remain as free-phase CO_2 after 100 years, with the remainder dissolved in the aqueous phase. Strong buoyancy forces were predicted to cause the plume to move predominantly upward toward the top of the formation, and then migrate horizontally along the top (impermeable) boundary. The tilted case considered a formation dip of 8°. In this case The plume migration was found to extend 3,000 m up dip and 1,600 m down dip after 30 years of CO_2 injection. Significantly more CO_2 dissolved into the aqueous phase than for the horizontal case. After 70 more years without injection (at 100 years), about 64% of the injected CO_2 had dissolved into the aqueous phase, with the rest remaining as free-phase CO_2. Sensitivity studies concerning migration

distance using the tilted model domain were conducted for formation permeability, permeability anisotropy, residual gas saturation, irreducible water saturation, and capillary entry pressure.

The reactive transport model was developed by introducing multicomponent heterogenous (i.e., aqueous-solid-gas) geochemical reactions into the hydrologic model. The initial rock mineralogy and brine chemistry were developed based on the characterization of core samples, shallow fluid samples, and geochemical modeling. The laboratory experiments provided measurements of brine compositions reacted with a sandstone representative of deep formations in the Newark Basin, both in the absence and presence of CO_2 for a variety of temperature and pressure conditions. These experiments suggested the destabilization of feldspars (plagioclase, albite, K-spar) by the drop in pH associated with CO_2 dissolution, which is expected to favor the formation of minerals such as kaolinite, muscovite, and paragonite. Likely dominant mineral sources for dissolved constituents, based on geochemical modeling of the experiments, were identified, suggesting the importance of chlorite and anhydrite in controlling Mg and Ca solubility, respectively.

Reactive-transport-modeling analyses including CO_2, aqueous, and mineralogical reactions were also conducted to evaluate changes in formation water chemistry and mineral precipitation and dissolution reactions. The primary rock minerals considered were quartz, plagioclase, and potassium feldspar, but several other minor minerals including Fe-chlorite and anhydrite were also included in the model. These simulations were conducted using the same two-dimensional radially symmetric model discussed for the hydrological model, and a two-dimensional cross-sectional model oriented along the dip of the formation to investigate the effects of a tilted storage formation. The pH within the CO_2-brine plume was predicted to drop near 5 and remain near this level within a zone extending up to about 1800 from the injection well after 30 years of injection. Major reactions involving formation minerals were found to consist of the dissolution of plagioclase, leading to the precipitation of chalcedony and dawsonite, and the dissolution of Fe-chlorite, resulting in ankerite and kaolinite precipitation. The overall computed porosity change from mineral dissolution and precipitation was found to be relatively small, consisting of a decrease in porosity of ~0.3%.

Given their importance in controlling the plume characteristics and fate of the injected CO_2, it is strongly recommended that more reliable site-specific data with regards to formation permeability (including its heterogeneity), relative permeability, and capillary characteristics be collected and incorporated in future model revisions. The model results also indicate that the effects of formation dip on plume migration and interactions with the aquifer brine are important and must be included in any long-term evaluations of CO_2 sequestration. Further model improvements that could be considered for future analyses are: (1) inclusion of the thermal effects; (2) accounting for capillary hysteresis; (3) characterizing and incorporating permeability heterogeneity, including fractures; and (4) accounting for the effects of salt precipitation on permeability.

A large uncertainty in this study is the lack of measured deep brine compositions. Should any further drilling be considered, the acquisition of deep brine samples within the Newark Basin would provide important additional constraints on the reactive transport simulations. Mineral reaction rates are also quite uncertain, relying on rate constants from the literature but also on typically unknown and/or poorly constrained reactive surface areas. The latter were estimated using typical assumed grain sizes, and

adjusted as necessary to yield near-steady brine-composition trends under "ambient" conditions of temperature and pressure within the formation, without CO_2 injection. It should also be noted that mechanisms and rate laws for the precipitation of secondary phases are particularly uncertain. In this study, the precipitation of secondary phases was predicted using rate laws and parameters that apply best to dissolution and may not apply to precipitation, particularly when far from equilibrium. Therefore, laboratory experiments tailored to better understand the precipitation mechanisms and rates of secondary phases would significantly constrain modeling results (such experiments were outside the scope of this study). Given these uncertainties, confidence in model results would be gained by further developing reactive transport modeling simulations to include (at least): (1) analyses of model results sensitivity to initial brine compositions and mineral reaction rates, focusing on short-term (~30 year) near-well processes affecting injection, (2) assessing interactions with cap-rock material, both experimentally and numerically, and (3) assessing CO_2 migration and mineralization rates over longer time periods (centuries and longer) than modeled here.

ACKNOWLEDGEMENT

This ARRA work was funded by the Fossil Energy program, Coal subprogram, Carbon Capture and Geologic Storage Assessment activity of the U.S. Department of Energy under Contract No. DE-AC02-05CH11231 with the U.S. Department of Energy.

COPYRIGHT NOTICE

DISCLAIMER

REFERENCES

Altunin, V.V. (1975), Thermophysical Properties of Carbon Dioxide. Publishing House of Standards, 551 pp., Moscow, Russia (in Russian).

Azizi, E., and Cinar, Y. (2013), Approximate analytical solutions for CO_2 injectivity into saline formations, SPE Reservoir Evaluation and Engineering, 16, 122-133.

Bachu, S. (2008), CO_2 storage in geological media: Role, means, status and barriers to deployment, Progress In Energy And Combustion Science, 34:254-273, doi: 10.1016/j.pecs.2007.10.001

Bachu, S. (2013), Drainage and imbibition CO_2/brine relative permeability curves at in situ conditions for sandstone formations in western Canada, Energy Procedia, 37, 4428-4436. 2012.

Bachu, S., and D. B. Bennion (2009), Interfacial tension between CO_2, freshwater, and brine in the range of pressure from (2 to 27) MPa, temperature from (20 to 125) °C, and water salinity from (0 to 334000) mg L^{-1}, J. Chem. Eng. Data, 54(3), 765–775.

Bénézeth, P., D. A. Palmer, L. M. Anovitz, and J. Horita (2007), Dawsonite synthesis and reevaluation of its thermodynamic properties from solubilitymeasurements: Implications for mineral trapping of CO_2, Geochim. Cosmochim.Acta, 71, 4438–4455

Bennion, D.B. and Bachu, S. (2008), Drainage and imbibition relative permeability relationships for supercritical CO_2 /brine and H2S/brine systems in intergranular sandstone, carbonate, shale and anhydrite rocks. SPE. Reservoir Evaluation & Engineering,11, 487-96.

Bennion, D.B. and Bachu, S. (2010), Drainage and imbibition relative permeability curves at reservoir conditions for carbonate formations. SPE Paper 134028. 2010; SPE Annual Technical Conference and Exhibition, 19-22 September 2010, Florence, Italy.

Benson, S., Pini, R., Reynolds, C., and Krevor, S.C.M. (2013), Relative permeability analyses to describe multiphase flow in CO_2 storage reservoirs, prepared for the Global CCS Institute http://www.globalccsinstitute.com/publications/relative-permeability-analysis-describe-multi-phase-flow-co2-storage-reservoirs

Bethke, C., 2008. Geochemical and Biogeochemical Reaction Modeling, 2nd ed. Cambridge University Press, New York.

Bikkina, P. K. (2011), Contact angle measurements of CO_2-water-quartz/ calcite systems in the perspective of carbon sequestration, Int. J. Greenhouse Gas Control, 5, 1259–1271.

Burton, M., Kumar, N., and Bryant, S.L. (2008), Time-dependent injectivity during CO_2 storage in aquifers, SPE-113937, presented at SPE/DOE Symposium on Improved Oil Recovery, Society of Petroleum Engineers, April 20-23, Tulsa, OK.

Carroll, S.; Mroczek, E.; Alai, M.; and Ebert, M. 1998. "Amorphous Silica Precipitation (60 to 120°C): Comparison of Laboratory and Field Rates." *Geochimica et Cosmochimica Acta, 62*, (8), 1379-1396.

Chadwick, R.A., Arts, R., Bentham, M., Eiken, O., Holloway, S., Kirby, G.A., Pearce, J.M., Williamson, J.P., and Zweigel, P. (2009), Review of monitoring issues and technologies associated with the long-term underground storage of carbon dioxide, In: Underground Gas Storage: Worldwide Experiences

and future development in the UK and Europe, Geological Society, London, Special Publications, 313, 257–75, London, UK.

Chalbaud, C., M. Robin, J.-M. Lombard, H. Bertin, and P. Egermann (2010), Brine/ CO_2 interfacial properties and effects on CO_2 storage in deep saline aquifers, Oil Gas Sci. Technol., 65(4), 541–555.

Chiquet, P., Broseta, D., and Thibeau, S. (2005), Capillary alteration of shaly caprocks by carbon dioxide, SPE-94183, SPE Europe/EAGE Annual Conforence, June 13-16, Madrid, Spain.

Chiquet, P., J. L. Daridon, D. Broseta, and S. Thibeau (2007a), CO_2/water interfacial tensions under pressure and temperature conditions of CO_2 geological storage, Energy Convers. Manage., 48(3), 736–744.

Chiquet, P., Broseta, D., and Thibeau, S. (2007b), Wettability alteration of caprock minerals by carbon dioxide, Geofluids, 7(2), 112–122.

Corey, A.T. (1954), The interrelation between gas and oil relative permeabilities, Producers Monthly, 38-41.

Cornet, B. (1977), The palynostratigraphy and age of the Newark Supergroup, Ph.D. Thesis, University Park, Pennsylvania, Pennsylvania State University, 504 p.

Dentz, M. and Tartakovsky, D.M. (2009), Abrupt-interface solution for carbon dioxide injection into porous media, Transport in Porous Media, 79, 15-27, doi:10.1007/s11242-008-9268-y.

Dickson, J. L., G. Gupta, T. S. Horozov, B. P. Binks, and K. P. Johnston (2006), Wetting phenomena at the CO_2/water/glass interface, Langmuir, 22(5), 2161–2170.

Doughty, C. (2007), Modeling geologic storage of carbon dioxide: comparison of non-hysteretic and hysteretic characteristic curves, Energy Conversion and Management 48, 1768-1781.

Drever J.I. (1997) The Geochemistry of Natural Waters. 3rd edition. Prentice Hall, 436 pp.

Duan, Z., Sun, R., 2003. An improved model calculating CO_2 solubility in pure water and aqueous NaCl solutions from 273 to 533 K and 0 to 2000 bar. Chem. Geol. 193, 257-271.

Duckworth, O.W., Martin, S.T. (2004) Role of molecular oxygen in the dissolution of siderite and rhodochrosite, *Geochimica et Cosmochimica Acta*, 68(3), 607–621.

Gaus, I. (2010), Role and impact of CO_2–rock interactions during CO_2 storage in sedimentary rocks, International Journal of Greenhouse Gas Control, 4, 73-89, doi: 10.1016/j.ijggc.2009.09.015.

Golubev, S.V. Bénézeth, P., Schott, J., Dandurand, J.L., Castillo, A. (2009) Siderite dissolution kinetics in acidic aqueous solutions from 25 to 100°C and 0 to 50 atm PCO_2. *Chemical Geology*, 265, 13–19.

Hellevang, H., J. Declercq, B. Kvamme, and P. Aagaard (2010), The dissolution rates of dawsonite at pH 0.9 to 5 and temperatures of 22, 60 and 77°C, Appl. Geochem., 25, 1575–1586.

Hesse, M. A., Orr, Jr, F. M., and Tchelepi, H. A. (2008), Gravity currents with residual trapping. Journal of Fluid Mechanics, 611, 35–60

Holland, T.J.B., Powell, R., 1998. An internally consistent thermodynamic dataset for phases of petrological interest. J. Met. Geol. (16) 309–343.

IPCC (Intergovernmental Panel on Climate Change) (2005), IPCC Special Report on Carbon Dioxide Capture and Storage, Cambridge University Press, New York, NY.

Jiang, X. (2011), A review of physical modeling and numerical simulation of long-term geological storage of CO_2, Applied Energy, 88, 3557-3566, doi:10.1016/j.apenergy.2011.05.004.

Johnson, J.W., Oelkers, E.H., Helgeson, H.C., 1992. SUPCRT92: A software package for calculating the standard molal thermodynamic properties of minerals, gases, aqueous species, and reactions from 1 to 5000 bar and 0 to 1000°C. Comp. Geosci. 18, 899-947.

Juanes, R., MacMinn, C., Szulczewski, M. (2010), The footprint of the CO_2 plume during carbon dioxide storage in saline aquifers: storage efficiency for capillary trapping at the basin scale. Transport in Porous Media 82 (1), 19–30.

Jung, J.-W., and J. Wan (2012), Supercritical CO_2 and ionic strength effects on wettability of silica surfaces: Equilibrium contact angle measurements,Energy Fuels, 26, 6053–6059.

Kang, Q., Lichtner, P.C., Viswanathan, H.S., and Abdel-Fattah, A.L. (2010), Pore scale modeling of reactive transport involved in geologic CO_2 sequestration, Transport in Porous Media, 82:197-213, doi: 10.1007/s11242-009-9443-9.

Kaszuba, J. P., D. R. Janecky, and M. G. Snow (2003), Carbon dioxide reaction processes in a model brine aquifer at 200°C and 200 bars: Implications for geologic sequestration of carbon, Applied Geochemistry, 18(7), 1065–1080.

Kharaka Y.K and R. H. Mariner (1989) Chemical Geothermometers and Their Application to Formation Waters from Sedimentary Basins. Chapter 6 in N. D. Naeser et al. (eds.), *Thermal History of Sedimentary Basins*, Springer-Verlag New York Inc.

Kharaka, Y. K., D. R. Cole, S. D. Hovorka, W. D. Gunter, K. G. Knauss, and B. M. Freifeld (2006), Gas-water-rock interactions in Frio formation following CO_2 injection: Implications for the storage of greenhouse gases in sedimentary basins, Geology, 34(7), 577–580.

Kim, Y., J. Wan, T. J. Kneafsey, and T. K. Tokunaga (2012), Dewetting of silica surfaces upon reactions with supercritical CO_2 and brine: Porescale studies in micromodels, Environ. Sci. Technol., 46, 4228–4235.

Kong, X.-Z., Tutolo, B.M., Saar, M.O., 2013. DBCreate: A SUPCRT92-based program for producing EQ3/6, TOUGHREACT, and GWB thermodynamic databases at user-defined T and P. Comp. Geosci. 51, 415-417.

Lasaga, A.C., Soler, J.M., Ganor, J., Burch, T.E., Nagy, K.L., 1994. Chemical weathering rate laws and global geochemical cycles. Geochimica et Cosmochimica Acta 58, 2361–2386.

Lemmon, E.W., McLinden, M.O., and Friend, D.G. (2005), Thermophysical properties of fluid systems, In NIST Chemistry WebBook; Mallard, W.G. and Linstrom, P.J. (eds.), NIST Standard Reference Database Number 69; National Institute of Standards and Technology: Gaithersburg, MD (http://webbook.nist.gov).

Li, X., E. Boek, G. C. Maitland, and J. P. M. Trusler (2012), Interfacial tension of (brines+CO_2) : (0.864 NaCl+0.136 KCl) at temperatures between (298 and 448) K, pressures between (2 and 50) MPa, and total molalities of (1 to 5) mol kg^{-1}, J. Chem. Eng. Data, 57(4), 1078–1088.

Liu, W., Yao, J., and wang, Y. (2012), Exact analytical solutions of moving boundary problems of one-dimensional flow in semi-infinite long porous media with threshold pressure gradient, International Journal of Heat and Mass Transfer, 55, 6017-6022, doi: 10.1016/j.ijheatmasstransfer.2012.06.012.

Lu, C., Lee, S., Han, W., McPherson, B., Lichtner, P. (2009), Comments on "Abrupt-Interface Solution for Carbon dioxide Injection into Porous Media" by M. Dentz and D. Tartakovsky, Transport in Porous Media, 79, 29–37.

Madden, M.E., Madden, A.S, Rimstidt, J.D., Zahrai, S., Kendall, M.R., Miller, M.A. (2012), Jarosite dissolution rates and nanoscale mineralogy, Geochimica et Cosmochimica Acta 91, 306–321.

Mathias S, Gluyas J, Gonzalez G, Bryant S, Wilson D. (2013), On relative permeability data uncertainty and CO_2 injectivity estimation for brine aquifers. Int. J. Greenhouse Gas Control, 12,200-212, http://dx.doi.org/10.1016/j.ijggc.2012.09.017.

McLaughlin, D. B. (1945), Type sections of the Stockton and Lockatong Formations: Proceedings of the Pennsylvania Academy of Science, 19, 102–103.

Mijic, A., LaForce, T.C., and Muggeridge, A.H., (2014), CO_2 injectivity in saline aquifers: The impact of non-Darcy flow, phase miscibility, and gas compressibility, Water Resources Research, 50, 4163–4185, doi:10.1002/2013WR014893.

Monea, M., Knudsen, R., Worth, K., Chalaturnyk, R., White, D., Wilson, M., Plasynski, S., Mcilvried, H. G. and Srivastava, R. D. (2013), Considerations for monitoring, verification, and accounting for geologic storage of CO_2, In: Carbon Sequestration and Its Role in the Global Carbon Cycle, Mcpherson, B.J., and Sundquist, E.T. (eds.), American Geophysical Union, Washington, DC, doi: 10.1029/2006GM000484.

Mualem, Y. A. (1976), New model for predicting the hydraulic conductivity of unsaturated porous media, Water Resources Research, 12, pp. 513 - 522.

NJGS (New Jersey Geological Survey) (2011), Preliminary characterization of CO_2 sequestration potential in New Jersey and the offshore coastal region, Trenton, NJ.

Nordbotten, J.A., Celia, M.A., Bachu, S., and Dahle, H. (2005), Semianalytical solution for CO_2 leakage through an abandoned well, Environmental Science and Technology, 39:602–11, doi:10.1021/es035338i.

Nordbotten, J.M., and Celia, M.A. (2006), Similarity solutions for fluid injection into confined aquifers, Journal of Fluid Mechanics, 561, 307–327.

Nordbotten, J.M., and Celia, M.A. (2011), Geological Storage of CO_2: Modeling Approaches for Large-Scale Simulations, John Wiley & Sons, Inc., Hoboken, NJ.

Olsen, P.E., Kent, D.V., Cornet, B., Witte, W.K., and Sclishche, R.W. (1996), High resolution stratigraphy of the Newark Rift Basin (early Mesozoic, eastern North America), Geological Society of America Bulletin, 108, 40-77.

Palandri, J., Kharaka, Y.K. (2004), A compilation of rate parameters of water–mineral interaction kinetics for application to geochemical modeling. US Geological Survey Open File Report 2004-1068, 64pp.

Plasynski, S.I., Litynski, J.T., McIlvried, H.G., Vikara, D.M., and Srivastava, R.D. (2011), The critical role of monitoring, verification, and accounting for geologic carbon dioxide storage projects, Environmental Geosciences, 18, 19-34, doi:10.1306/eg.06231010008.

Pruess, K. and Müller, N. (2009), Formation dry-out from CO_2 injection into saline aquifers: 1. Effects of solids precipitation and their mitigation, Water Resources Research, 45, W03402, doi:10.1029/2008WR007101.

Pruess, K., and Spycher, N. (2007), ECO2N – A fluid property module for the TOUGH2 code for studies of CO_2 storage in deep saline aquifers, Energy Conversion and Management, 48, 1761-1767, doi: 10.1016/j.enconman.2007.01.016.

Pruess, K., C.M. Oldenburg and G.J. Moridis (2012). TOUGH2 User's Guide Version 2.1 E. O. Lawrence Berkeley National Laboratory Report LBNL-43134, 1999; and LBNL-43134 (revised), 2012.

Reed M.H., 1998. Calculation of simultaneous chemical equilibria in aqueous-mineral-gas systems and its application to modeling hydrothermal processes. In: Techniques in Hydrothermal Ore Deposits Geology, Reviews in Economic Geology, Volume 10. Richards J, Larson P (eds), 109–124.

Reed M.H., Palandri J., 2006. SOLTHERM.H06, a database of equilibrium constants for minerals and aqueous species. Available from the authors, University of Oregon, Eugene, Oregon.

Reed, M. H., Spycher, N.F., 1984. Calculation of pH and Mineral Equilibria in Hydrothermal Waters With Application to Geothermometry and Studies of Boiling and Dilution. Geochimica et Cosmochimica Acta, vol. 48, 1479–1492.

Reed, M.H., 1982. Calculation of multicomponent chemical equilibria and reaction processes in systems involving minerals, gases and an aqueous phase. Geochimimica et Cosmochimica Acta (46) 513–528.

Rutqvist, J. (2012), The geomechanics of CO_2 storage in deep sedimentary formations, Geotechnical and Geological Engineering, 30, 525-551, doi: 10.1007/s10706-011-9491-0.

Schlumberger (2012) Water Analysis on Bottomhole Samples, Field: Wildcat, Well: NYSTA TANDEM LOT 1, for Sandia Technologies. Water Study Report Report #: 201100158 (William Dale Logan), Schlumberger Carbon Services, February 8. Seyfried, W.E., Jr., Janecky, D.R., Berndt, M.E., 1987. Rocking autoclaves for hydrothermal experiments II: The flexible reaction-cell system, in: Ulmer, G.C., Barnes, H.L. (Eds.), Hydrothermal Experimental Techniques. Wiley Interscience, pp. 216-239.

Seyfried, W. E., Gordon, P.C. and Dickson, F.W. (1979) "A new reaction cell for hydrothermal solution equipment." Am. Mineral. 64: 646-649.

Shao, H., J. R. Ray, and Y. S. Jun (2011), Effects of salinity and the extent of water on supercritical CO_2-induced phlogopite dissolution and secondary mineral formation, Environ. Sci. Technol., 45(4), 1737–1743.

Shock, E.L., Sassani, D.C., Willis, M., Sverjensky, D.A., 1997. Inorganic species in geologic fluids: Correlations among standard molal thermodynamic properties of aqueous ions and hydroxide complexes. Geochim. Cosmochim. Acta 61, 907-950.

Slider, H. C., Practical petroleum reservoir engineering methods, An Energy Conservation *Science*. Tulsa, Oklahoma, Petroleum Publishing Company, 1976.

Spycher, N., and Pruess, K. (2005), CO_2-H_2O mixtures in the geological sequestration of CO_2: II Partitioning in chloride brines at 12 − 100°C and up to 600 bars, Geochimica and Cosmochimica Acta, 69, 13, 3309–3320.

Spycher, N., Peiffer, L., Sonnenthal, E., (2013). GeoT User's Guide A Computer Program for Multicomponent Geothermometry and Geochemical Speciation Version 1.4. Lawrence Berkeley National Laboratory, Report No. LBNL-6172E. http://esd.lbl.gov/research/projects/geot/

Spycher, N., Peiffer, L., Saldi, G., Sonnenthal, E., Reed, M.H., Kennedy, B.M., 2014. Integrated multicomponent solute geothermometry. Geothermics 51, 113–123.Sverjensky, D.A., Shock, E.L., Helgeson, H.C., 1997. Prediction of the thermodynamic properties of aqueous metal complexes to 1000°C and 5 kb. Geochim. Cosmochim. Acta 61, 1359-1412.

Teatini P., Gambolati, G., Ferronata, M., Settari A, Walters, D. (2011), Land uplift due to subsurface fluid injection, Journal of Geodynamics, 51, 1–16.

Teatini, P., Castelleto, N., and Gambolati, G. (2014), 3D geomechanical modeling for CO_2 geological storage in faulted formations: A case study in an offshore northern Adriaticreservoir, Italy, International Journal of Greenhouse Gas Control, 22, 63-76, doi: 10.1016/j.ijggc.2013.12.021.

Tokunaga, T. K., J. Wan, J.-W. Jung, T. W. Kim, Y. Kim, and W. Dong (2013), Capillary pressure and saturation relations for supercritical CO_2 and brine in sand: High-pressure Pc(Sw) controller/meter measurements and capillary scaling predictions, Water Resour. Res., 49, 4566–4579, doi:10.1002/wrcr.20316.

Tutolo, B.M., Kong, X.-Z., Seyfried, W.E., Jr., Saar, M.O., 2014. Internal consistency in aqueous geochemical data revisited: Applications to the aluminum system. Geochim. Cosmochim. Acta 133, 216-234.

van de Kamp, P.C., and Leake, B.E. (1996), Petrology, geochemistry, and Na metasomatism of Triassic-Jurassic non-marine clastic sediments in the Newark, Hartfield, and Deerfield rift basins, northeastern USA, Chemical Geology, 133, 89-124.

van Genuchten, M.Th. (1980), A closed-form equation for predicting the hydraulic conductivity of unsaturated soils, Soil Sci. Soc. America Journal., 44, 5, 892–898.

Weatherford Laboratories (2012). X-ray diffraction results for Sandia Technologies, Well NYSTA Tandem Lot No.1, Rotary sidewall core. File no. HH-54004, analysis by T. Bujnowski and R. Schulze, 11/29/12.

Wang, S., I. M. Edwards, and A. F. Clarens (2013), Wettability phenomena at the CO_2-brine-mineral interface: Implications for geologic carbon sequestration, Environ. Sci. Technol., 47(1), 234–241.

Wolela, A.M., and Gierlowski-Kordesch, E. (2007), Diagenetic history of fluvial and lacustrine sandstones of the Hartford Basin (Triassic–Jurassic), Newark Supergroup, USA, Sedimentary Geology, 197, 99–126

Xu, T., Spycher, N., Sonnenthal, E., Zhang, G., Zheng, L., Pruess, K. (2011) TOUGHREACT Version 2.0: A simulator for subsurface reactive transport under non-isothermal multiphase flow conditions. *Computers & Geosciences,* 37, 763–774.

Yang, L., Steefel, C.I., 2008. Kaolinite dissolution and precipitation kinetics at 22°C and pH 4. Geochimica et Cosmochimica Acta 72, 99–116.

Yang, D., and Gu, Y. (2004), Interfacial interactions of crude oil-brine- CO_2 systems under reservoir conditions, SPE-90198, SPE Annual Technical Conference and Exhibition, September 26-29, Houston, TX.

Yortsos, Y. C. (1995), A theoretical analysis of vertical flow equilibrium. Transport in Porous Media, 18, 107–129, doi: 10.1007/BF01064674.

Zhang, D., and Song, J. (2014), Mechanisms for geological carbon sequestration, Procedia IUTAM, 10, 319-327, doi: 10.1016/j.piutam.2014.01.027.

Appendix A – Numerical Simulators

A1: TOUGH2 and TOUGHREACT

TOUGH2 is an integral-finite-difference numerical code (Pruess et al., 2012) for simulating coupled flow and transport of water, water vapor, air, and heat in heterogeneous porous and fractured media. TOUGH2 accounts for the movement of gaseous and liquid phases (under pressure, viscous, and gravity forces according to Darcy's law, with interference between the phases represented by relative permeability functions); transport of latent and sensible heat; and phase transition between liquid and vapor, wherever applicable. Mass- and energy-balance equations are written in integral form for an irregular flow domain in one, two, or three dimensions. Fluid flow is described with a multiphase extension of Darcy's law. Heat occurs by conduction and convection. The description of thermodynamic conditions is based on a local equilibrium model of the three phases (liquid, gas, and solid rock). A brief description of the numerical simulation framework implemented in TOUGH2 is provided further below.

The ECO2N fluid property module (Spycher and Pruess, 2005; Pruess and Spycher, 2007), which has been designed specifically for CO_2-brine systems, of the TOUGH2 simulator has been used in this report for reactive transport modeling. The ECO2N module includes a comprehensive description of the thermodynamics and thermophysical properties of H_2O–NaCl–CO_2 mixtures, that reproduces fluid properties largely within experimental error for the temperature, pressure, and salinity conditions of interest (10°C $\leqslant T \leqslant$ 110°C; $P \leqslant$ 600 bar; salinity up to full halite saturation). Flow processes can be modeled isothermally or nonisothermally, and phase conditions represented may include a single (aqueous or CO_2-rich) phase, as well as two-phase mixtures. Fluid phases may appear or disappear in the course of a simulation, and solid salt may precipitate or dissolve. ECO2N can model super- as well as subcritical conditions, but it does not make a distinction between liquid and gaseous CO_2, and hence is not applicable for processes that involve two CO_2-rich phases.

The basic mass- and energy-balance equations solved by TOUGH2 (Pruess et al., 2012) can be written in the general form

$$\frac{d}{dt}\int_{V_n} M^{\kappa} dV_n = \int_{\Gamma_n} \mathrm{F}^{\kappa} \cdot \mathbf{n} d\Gamma_n + \int_{V_n} q^{\kappa} dV_n \qquad \text{(Eq. A1.1)}$$

The integration is over an arbitrary subdomain V_n of the flow and transport domain under study, which is bounded by the closed surface Γ_n. The quantity M appearing in the accumulation (left hand side) represents mass or energy per volume, with κ = 1, 2 labeling the mass components water and carbon dioxide, and κ = 3 the "heat component." F denotes mass or heat flux (see below), q denotes sinks and sources, and $\mathbf{n}$ is a normal vector on surface element $d\Gamma_n$, pointing inward into V_n.

The general form of the mass accumulation term is

$$M^{\kappa} = \phi \sum_{\beta} S_{\beta} \rho_{\beta} X_{\beta}^{\kappa} \qquad \text{(Eq. A1.2)}$$

The total mass of component κ is obtained by summing over the phases β (= liquid, gas), with ϕ the porosity, S_β the saturation of phase β (i.e., the fraction of pore volume occupied by phase β), ρ_β the density of phase β, and X_β^κ the mass fraction of component κ in phase β. Similarly, the heat accumulation term in a multiphase system is

$$\boldsymbol{M}^{3} = (1-\phi)\rho_R \boldsymbol{C}_R \boldsymbol{T} + \phi \sum_{\beta} \boldsymbol{S}_{\beta} \rho_{\beta} \boldsymbol{u}_{\beta} \qquad \text{(Eq. A1.3)}$$

where ρ_R and C_R are, respectively, rock-grain density and specific heat capacity of the rock, T is temperature, and u_β is specific internal energy in phase β.

Advective mass flux is a sum over phases,

$$\boldsymbol{F}^{\kappa}\big|_{adv} = \sum_{\beta} X_{\beta}^{\kappa} \boldsymbol{F}_{\beta}, \qquad \text{(Eq. A1.4)}$$

and individual phase fluxes are given by a multiphase version of Darcy's law (continuum representation),

$$\mathbf{F}_{\beta} = \rho_{\beta} \mathbf{u}_{\beta} = -\boldsymbol{k} \frac{\boldsymbol{k}_{r\beta} \rho_{\beta}}{\mu_{\beta}} \left(\nabla \boldsymbol{P}_{\beta} - \rho_{\beta} \mathbf{g} \right) \qquad \text{(Eq. A1.5)}$$

Here, $\mathbf{u}_\beta$ is the Darcy velocity in phase β, k is absolute permeability, $k_{r\beta}$ is the relative permeability to phase β, μ_β is viscosity, and

$$P_{\beta} = P + P_{c\beta} \qquad \text{(Eq. A1.6)}$$

is the fluid pressure in phase β, which is the sum of the pressure P of a reference phase (gas pressure) and the capillary pressure $P_{c\beta}$ (≤ 0); and g is the vector of gravitational acceleration.

Heat flux includes conductive and convective components

$$\boldsymbol{F}^{3} = -\lambda \nabla T + \sum_{\beta} h_{\beta} F_{\beta} \qquad \text{(Eq. A1.7)}$$

where λ is the thermal conductivity of the rock-fluid mixture, and h_β is the specific enthalpy in phase β.

Capillary pressures and relative permeabilities depend on phase saturation. Unless stated otherwise, capillary pressure and relative permeability of the water phase have the van Genuchten functional forms (van Genuchten 1980; Mualem 1976):

$$P_{cl} = -\frac{1}{\alpha}\left[\left(S_{l,eff}\right)^{-1/m} - 1\right]^{1-m}$$

$$k_{rl} = \left(S_{l,eff}\right)^{1/2}\left[1 - \left(1 - \left(S_{l,eff}\right)^{1/m}\right)^{m}\right]^{2}$$

$$S_{l,eff} = \frac{\left(S_l - S_{lr}\right)}{\left(S_{ls} - S_{lr}\right)} \qquad \text{(Eq. A1.8)}$$

where $S_{l,eff}$ is liquid effective saturation, S_l is liquid saturation, S_{lr} is liquid residual saturation, and m and $1/\alpha$ are fitting parameters, the latter related to the capillary strength of the medium.

Relative permeability for gas flow is described by the Corey (1954) formulation as follows:

$$k_{rg} = \left(1 - \hat{S}\right)^{2}\left(1 - \hat{S}^{2}\right), \qquad \text{(Eq. A1.9)}$$

where $\hat{S} = \dfrac{S_l - S_{lr}}{1 - S_{lr} - S_{gr}}$, where S_{gr} is the residual gas saturation. Note that, if $S_{gr} = 0$, the code automatically assumes $k_{rg} = 1 - k_{rl}$. The selected formulations for the dependence of the capillary pressure and the relative permeability on liquid-phase saturation are widely employed in the literature. Note also that hysteresis in capillary pressure function for CO_2-water system has not been considered in this report.

The TOUGHREACT simulator (Xu et al., 2011) has been developed by introducing reactive chemistry into the existing framework of the TOUGH2 nonisothermal multiphase, multicomponent fluid and heat transport simulator. A number of subsurface thermo-physical-chemical processes are considered under various conditions of temperature, pressure, and system chemical composition. The transport of aqueous and gaseous species by advection and molecular diffusion are considered in both the liquid and gas phases. Geochemical processes considered include aqueous and surface complexation, redox reactions, gas dissolution/exsolution, and multisite cation exchange and mineral dissolution and precipitation. Reactions involving aqueous species and/or minerals can proceed under either equilibrium or kinetic constraints. Other reactions are assumed to take place under thermodynamic equilibrium, relying on an external thermodynamic database (Appendix C). Linear adsorption and decay can be also included in simulations.

TOUGHREACT uses a sequential iteration approach (SIA). That is, after the heat and fluid flow equations have been solved by the TOUGH2 modules, the fluid velocities and phase saturations are used to simulate the transport of chemical species, followed by their reaction. Chemical transport is solved on a

component-by-component basis, using total concentrations for each component. The resulting total concentrations obtained from solving the transport equations are then used for speciation/reaction computations on a grid block by grid block basis, by Newton-Raphson iterations, using a mass-balance/mass-action formulation similar to that described by Reed (1982), with added kinetics of mineral precipitation/dissolution as described in Appendix C. Optionally, as an alternative to the sequential iterative approach, a sequential noniterative approach (SNIA) may be used (but is not used in the present study).

Temporal changes in porosity, permeability, and capillary pressure caused by mineral dissolution and precipitation are computed by TOUGHREACT. The change in porosity is calculated from the computed increase and decrease in the volume fraction of each mineral considered in the simulations. Various porosity-permeability correlations have been implemented into the code, such as that of Verma and Pruess, (1988), and the Carman-Kozeny relationship. The latter is implemented in this study. The capillary pressure is modified via permeability and porosity changes using Leverett scaling (based on Slider, 1976).

A2: GeoT

GeoT (Spycher et al., 2013 and 2014) was developed drawing on existing routines and methods implemented into programs TOUGHREACT (Xu et al., 2011), SOLVEQ/CHILLER (Reed, 1982, 1998) and GEOCAL (Spycher and Reed, unpublished, U. Oregon, 1985). The core of the software is essentially a homogenous geochemical speciation algorithm solving mass-balance/mass-action equations by Newton-Raphson iterations (e.g., Reed, 1982). Using complete fluid analyses, the saturation indices of minerals (log(Q/K)) are obtained from the computed ion activity product (Q) and thermodynamic equilibrium constant (K) of each considered mineral. Data for the computation of activity coefficients, together with equilibrium constants for aqueous complexes and minerals at various temperatures, are read from an external thermodynamic database (Appendix C). The pH at high temperatures is calculated from the total numerical H+ concentration computed from the input (known) low-temperature pH, following the method of Reed and Spycher (1984). The program allows for simultaneous regression of multiple waters, automatic reconstitution of deep fluid compositions, and estimation of reservoir temperature from statistical evaluation of computed mineral saturation indices.

A3: CHILLER

CHILLER is a geochemical simulator for computing multicomponent heterogenous chemical equilibria among solids, gases, and an aqueous phase (Reed, 1982 and 1998). CHILLER was developed to simulate mineral precipitation during the cooling of hydrothermal solutions, reaction of solutions with various types of rocks and gases, fluid-fluid mixing, boiling, condensation, and evaporation. The equilibria between the different phases are computed with respect to the aqueous phase, using a system of mass-balance/mass-action equations solved by Newton-Raphson iterations. A heat balance equation can also be solved simultaneously with the other equations to simulate boiling and other non-isothermal gas phase

exsolution processes. Simulations with CHILLER involve incrementally changing temperature, pressure, composition and/or enthalpy; at each step, the compositions of the aqueous, solid, and gas phases at thermodynamic equilibrium is computed. The thermodynamically stable mineral phases are automatically selected from a separate database (Appendix C) including a large number of minerals. This type of simulation, which do not involve transport, are often referred to as "batch" or "reaction path" simulations

Appendix B – Derivation for Transient Front Locations

Pressure within the gas phase can be written as

$$p(x,y,z,t) = p_0(x,y,t) + \rho_g g z \cos\theta \qquad \text{(Eq. B.1)}$$

where $p_0(x,y,t)$ is the pressure at a reference plane, e.g., at the top of the confined aquifer. Pressure in the water phase can be similarly expressed as

$$p(x,y,z,t) = p_0(x,y,t) + \rho_g g h \cos\theta + \rho_w g \cos\theta (z-h) \qquad \text{(Eq. B.2)}$$

Or, in other words

$$p(x,y,z,t) = p_0(x,y,t) - \Delta\rho g h \cos\theta + \rho_w g z \cos\theta \qquad \text{(Eq. B.3)}$$

where $\Delta\rho = \rho_w - \rho_g$. Assuming Darcy's law to be valid, velocity of the water phase can be written as

$$\mathbf{u_w} = -\frac{\mathbf{k}}{\mu_w}(\nabla p + \rho_w \mathbf{g}) \qquad \text{(Eq. B.4)}$$

Combining Equations B.3 and B.4, we obtain

$$\mathbf{u_w} = -\frac{\mathbf{k}}{\mu_w}(\nabla p_0 - \Delta\rho g \cos\theta \nabla h + \rho_w \mathbf{g}) \qquad \text{(Eq. B.5)}$$

From Equation B.5, it is easy to see that

$$\nabla p_0 + \rho_w \mathbf{g} = -\frac{\mu_w}{\mathbf{k}}\mathbf{u_w} + \Delta\rho g \cos\theta \nabla h \qquad \text{(Eq. B.6)}$$

If we further assume that Darcy's law is applicable for flow in the gas phase as well, we can express gas-phase velocity as

$$\begin{aligned}\mathbf{u_g} &= -\frac{\mathbf{k}}{\mu_g}\left(\nabla p_0 + \rho_g \mathbf{g}\right) \\ &= -\frac{\mathbf{k}}{\mu_g}\left(\nabla p_0 + \rho_w \mathbf{g} - \Delta\rho \mathbf{g}\right)\end{aligned} \qquad \text{(Eq. B.7)}$$

Inserting Equation B.6 into Equation B.7, we obtain

$$\mathbf{u_g} = \frac{\mu_w}{\mu_g}\mathbf{u_w} - \frac{\mathbf{k}}{\mu_g}\left[\Delta\rho g \cos\theta \nabla h - \Delta\rho \mathbf{g}\right] \qquad \text{(Eq. B.8)}$$

Invoking Dupuits approximation, in the absence of natural background flow, we can write

$$\mathbf{u_g} h + \mathbf{u_w}\left(H - h\right) = 0 \qquad \text{(Eq. B.9)}$$

In other words,

$$\begin{aligned}\mathbf{u_w} &= -\mathbf{u_g}\frac{h}{H-h} \\ &= -\mathbf{u_g}\frac{\hat{h}}{1-\hat{h}}\end{aligned} \qquad \text{(Eq. B.10)}$$

where we have introduced the dimensionless plume height as $\hat{h} = h/H$. Inserting the expression for $\mathbf{u_w}$ from Equation B.10 into Equation B.8, we obtain after some algebraic manipulation

$$\mathbf{u_g} = -\frac{\lambda \mathbf{k}}{\mu_g}\left(1-\hat{h}\right)\left[\frac{\Delta\rho g \cos\theta \nabla h - \Delta\rho \mathbf{g}}{\lambda\left(1-\hat{h}\right)+\hat{h}}\right] \qquad \text{(Eq. B.11)}$$

In Equation B.11, $\lambda = \mu_g/\mu_w$, which is the ratio of CO_2 and brine viscosity. Because $\lambda <<< 1$ in CO_2-brine systems, we can simplify Equation B.11 to obtain

$$\mathbf{u_g} = -\frac{\mathbf{k}}{\mu_w}\frac{\left(1-\hat{h}\right)}{\hat{h}}\left[\Delta\rho g H \cos\theta \nabla \hat{h} - \Delta\rho \mathbf{g}\right] \qquad \text{(Eq. B.12)}$$

Assuming both the fluid phases to be incompressible and the rock to have negligible compressibility, we can write the equation of continuity for the water phase as

$$\phi\frac{\partial \hat{h}}{\partial t} = -\nabla.\left(\mathbf{u_w}\hat{h}\right) \qquad \text{(Eq. B.13)}$$

where ϕ is the porosity of the storage aquifer. Similarly, the equation of continuity for the gas phase is

$$\phi\frac{\partial\hat{h}}{\partial t}=-\nabla.\left(\mathbf{u}_g\hat{h}\right) \qquad \text{(Eq. B.14)}$$

Introducing Equation B.12 into Equation B.14, we can finally write

$$\phi\frac{\partial\hat{h}}{\partial t}=\nabla.\frac{\mathbf{k}\left(1-\hat{h}\right)}{\mu_w}\left[\Delta\rho gH\cos\theta\nabla\hat{h}-\Delta\rho\mathbf{g}\right] \qquad \text{(Eq. B.15)}$$

At this point, it is more convenient to expand the gradient operators and rewrite Equation B.15 in its full form, i.e.,

$$\begin{aligned}\phi\frac{\partial\hat{h}}{\partial t}&=\frac{k_x}{\mu_w}\Delta\rho g\cos\theta\frac{\partial}{\partial x}\left(1-\hat{h}\right)g\left[H\frac{\partial\hat{h}}{\partial x}-\tan\theta\right]+\frac{k_y}{\mu_w}\Delta\rho g\cos\theta\frac{\partial}{\partial y}\left(1-\hat{h}\right)\left[H\frac{\partial\hat{h}}{\partial y}-\tan\theta\right]\\&=\frac{\Delta\rho g\sin\theta}{\mu_w}\left[k_x\frac{\partial\hat{h}}{\partial x}+k_y\frac{\partial\hat{h}}{\partial y}\right]+\frac{\Delta\rho gH\cos\theta}{\mu_w}\left[k_x\frac{\partial}{\partial x}\left(1-\hat{h}\right)\frac{\partial\hat{h}}{\partial x}+k_y\frac{\partial}{\partial y}\left(1-\hat{h}\right)\frac{\partial\hat{h}}{\partial y}\right]\\&=\frac{k_x\Delta\rho g\sin\theta}{\mu_w}\left[\frac{\partial\hat{h}}{\partial x}+a\frac{\partial\hat{h}}{\partial y}\right]+\frac{k_x\Delta\rho gH\cos\theta}{\mu_w}\left[\frac{\partial}{\partial x}\left(1-\hat{h}\right)\frac{\partial\hat{h}}{\partial x}+a\frac{\partial}{\partial y}\left(1-\hat{h}\right)\frac{\partial\hat{h}}{\partial y}\right]\end{aligned} \qquad \text{(Eq. B.16)}$$

In Equation B.16, k_x and k_y are the permeabilities in the x and y directions, respectively, and $a=k_x/k_y$ can be called the permeability anisotropy ratio. Introducing dimensionless variables $\xi_1=x/H$, $\xi_2=y/H$, and $\tau=tk_x\Delta\rho g\cos\theta\Big/\phi\mu_wH\left(\bar{\hat{h}}-\bar{\hat{h}}^2/2\right)$, where $\bar{\hat{h}}$ is the average of $\hat{h}$ (yet to be determined), we can write Equation B.16 as

$$\frac{1}{\bar{\hat{h}}-\dfrac{\bar{\hat{h}}^2}{2}}\frac{\partial\hat{h}}{\partial\tau}=\tan\theta\left[\frac{\partial\hat{h}}{\partial\xi_1}+a\frac{\partial\hat{h}}{\partial\xi_2}\right]+\left[\frac{\partial^2}{\partial\xi_1^2}\left(\hat{h}-\frac{\hat{h}^2}{2}\right)+a\frac{\partial^2}{\partial\xi_2^2}\left(\hat{h}-\frac{\hat{h}^2}{2}\right)\right] \qquad \text{(Eq. B.17)}$$

The derivative in the left hand side of Equation B.17 can be approximated as $\partial/\partial\tau\left[h-h^2/2\right]$, which is commonly applied in gas flow modeling on the basis of pseudo gass pressure, leading us to

$$\frac{\partial R}{\partial\tau}=Pe\left[\frac{\partial R}{\partial\xi_1}+a\frac{\partial R}{\partial\xi_2}\right]+\left[\frac{\partial^2R}{\partial\xi_1^2}+a\frac{\partial^2R}{\partial\xi_2^2}\right] \qquad \text{(Eq. B.18)}$$

In Equation B.18, we have defined $R=\hat{h}-\hat{h}^2/2$ and $Pe=\dfrac{\tan\theta}{\bar{\hat{h}}-\bar{\hat{h}}^2/2}$. Equation B.18 is recognizable as a convective diffusion equation, where the convective contribution arises from the sloping nature of the aquifer, and Pe can be termed the Peclet number for buoyancy driven flow in a sloping aquifer. The

diffusive terms in Equation B.18 do not arise from physical diffusion but buoyancy diffusion caused by the difference in density of the two fluid phases.

To solve Equation B.18, we will first assume that the aquifer is horizontal, i.e., $\theta = 0$, such that the first term on the right hand side disappears yielding

$$\frac{\partial R}{\partial \tau} = \left[\frac{\partial^2 R}{\partial \xi_1^2} + a \frac{\partial^2 R}{\partial \xi_2^2} \right] \qquad \text{(Eq. B.19)}$$

Equation B.19 needs to be solved with the initial and boundary conditions of

$$R(\xi_1, \xi_2, 0) = 0 \qquad \text{(Eq. B.20a)}$$

$$R[\delta_{D1}(\tau), \xi_2, \tau] = 0 \qquad \text{(Eq. B.20b)}$$

$$R[\xi_1, \delta_{D2}(\tau), \tau] = 0 \qquad \text{(Eq. B. 20c)}$$

$$R(0,0,\tau) = \frac{1}{2} \qquad \text{(Eq. B.20d)}$$

In Equations B.20b and B.20c, δ_{D1} and δ_{D2} are the dimensionless outer locations of the moving CO_2 front, both of which are functions of their respective locations in the (x, y) plane and time. Note that, in addition to the above boundary conditions, we will need other conditions to explicitly solve Equation B.19. It is possible to derive these additional conditions from the overall mass balance of the fluid phases. We will discuss and derive these conditions later.

Observe that a product solution of the form $R = \psi_1(\xi_1, \tau)\psi_2(\xi_2, \tau)$ satisfies Equation B.19, if it is imposed that

$$\frac{\partial \psi_1}{\partial \tau} - \frac{\partial^2 \psi_1}{\partial \xi_1^2} = 0 \qquad \text{(Eq. B.21a)}$$

$$\frac{\partial \psi_2}{\partial \tau} - a \frac{\partial^2 \psi_2}{\partial \xi_2^2} = 0 \qquad \text{(Eq. B.21b)}$$

We can obtain similarity solutions to both Equations B.21a and B.21b, if we define similarity variables $\zeta_1 = \xi_1 / 2\sqrt{\tau}$, $\zeta_2 = \xi_2 / 2\sqrt{\tau}$, $\sigma_1 = \psi_1 / 2\sqrt{\tau}$, and $\sigma_2 = \psi_2 / 2\sqrt{\tau}$. With these similarity transformations, the second-order partial differential equation for *R* (Equation B.19) is converted into two second-order ordinary differential equations for σ_1 and σ_2, i.e.,

$$\frac{1}{2}\frac{d^2\sigma_1}{d\zeta_1^2}+\zeta_1\frac{d\sigma_1}{d\zeta_1}-\sigma_1=0 \qquad \text{(Eq. B.22a)}$$

$$\frac{a}{2}\frac{d^2\sigma_2}{d\zeta_2^2}+\zeta_2\frac{d\sigma_2}{d\zeta_2}-\sigma_2=0 \qquad \text{(Eq. B.22b)}$$

It is possible to write a solution for Equation B.22a in the following form (Liu et al., 2012)

$$\sigma_1(\zeta_1)=\frac{A_1\left[\zeta_1\left\{e^{-\eta_1^2}+\sqrt{\pi}\eta_1 erf(\eta_1)\right\}-\eta_1\left\{e^{-\zeta_1^2}+\sqrt{\pi}\zeta_1 erf(\zeta_1)\right\}\right]}{e^{-\eta_1^2}+\sqrt{\pi}\eta_1 erf(\eta_1)} \qquad \text{(Eq. B.23)}$$

where A_1 is a constant of integration, and $\eta_1=\delta_{D1}/2\sqrt{\tau}$ is the similarity-transformed front location in the *x* direction. Note that, in writing Equation B.23, we have used the boundary condition $\sigma_1(\zeta_1=\eta_1)=0$. If we now define $G(\zeta_1)=e^{-\zeta_1^2}+\sqrt{\pi}\zeta_1 erf(\zeta_1)$, Equation B.23 can be expressed as

$$\sigma_1(\zeta_1)=\frac{A_1}{G(\eta_1)}\left[\zeta_1 G(\eta_1)-\eta_1 G(\zeta_1)\right] \qquad \text{(Eq. B.24a)}$$

The solution to Equation B.22b can be similarly written as

$$\sigma_2(\zeta_2)=\frac{A_2}{F(\eta_2)}\left[\zeta_2 F(\eta_2)-\eta_2 F(\zeta_2)\right] \qquad \text{(Eq. B.24b)}$$

where we have defined $F(\zeta_2)=\left[e^{-\zeta_2^2/a}+\sqrt{\pi/a}\zeta_2 erf\left(\zeta_2/\sqrt{a}\right)\right]$. In Equation B.24b, we have defined $\eta_2=\delta_{D2}/2\sqrt{\tau}$ is the similarity-transformed front location in the *y* direction. Note that, in writing Equation B.24b, we have used the boundary condition $\sigma_2(\zeta_2=\eta_2)=0$. In the above, $erf(\varsigma)$ is the error function given by

$$erf(\varsigma)=\frac{2}{\sqrt{\pi}}\int_0^{\varsigma}e^{-\omega^2}d\omega \qquad \text{(Eq. B.25)}$$

Introducing the expressions for σ_1 and σ_2 into the definition for *R*, i.e., $R=4\tau\sigma_1\sigma_2$, we get

$$R(\zeta_1,\zeta_2,\tau)=\frac{4A\tau}{G(\eta_1)F(\eta_2)}\left[\zeta_1 G(\eta_1)-\eta_1 G(\zeta_1)\right]\left[\zeta_2 F(\eta_2)-\eta_2 F(\zeta_2)\right] \qquad \text{(Eq. B.26)}$$

where $A=A_1A_2$ is an arbitrary constant, which is yet to be determined.

To determine A, we use the boundary condition in Equation B.20d, which states that injection happens along a vertical line at the center of the model domain, where $h = H$ or $\hat{h} = 1$ or $R = \hat{h} - \hat{h}^2/2 = \frac{1}{2}$. Application of this boundary condition on Equation B.26 results in the following relationship

$$\frac{4A\tau}{G(\eta_1)F(\eta_2)} = \frac{1}{2\eta_1\eta_2} \qquad \text{(Eq. B.27)}$$

Inserting this expression into Equation B.26, we finally obtain

$$R(\zeta_1,\zeta_2,\tau) = \frac{1}{2\eta_1\eta_2}\left[\zeta_1 G(\eta_1) - \eta_1 G(\zeta_1)\right]\left[\zeta_2 F(\eta_2) - \eta_2 F(\zeta_2)\right] \qquad \text{(Eq. B.28)}$$

Equation B.28 expresses the evolution of the CO_2 plume satisfying Equation B.19 and the initial and boundary conditions in Equation B.20. However, it is not complete yet because η_1 and η_2 are still unknown, and we need to generate expressions for them.

For this purpose, we first use the require that

$$\frac{\partial h}{\partial x}\Big|_{x=0} = \frac{\partial h}{\partial y}\Big|_{y=0} \qquad \text{(Eq. B.29)}$$

Equation B.29 can be written in dimensionless form as

$$\frac{\partial R}{\partial \xi_1}\Big|_{\xi_1=0} = \frac{\partial R}{\partial \xi_2}\Big|_{\xi_2=0} \qquad \text{(Eq. B.30)}$$

which leads us to the following result

$$\left[e^{-\eta_1^2} + \sqrt{\pi}\eta_1 erf(\eta_1)\right] = \left[e^{-\eta_2^2/a} + \sqrt{\frac{\pi}{a}}\eta_2 erf\left(\frac{\eta_2}{\sqrt{a}}\right)\right] \qquad \text{(Eq. B.31)}$$

Note that, if the system is isotropic $(a = 1)$, the only way Equation B.31 can be satisfied is when $\eta_1 = \eta_2$. In other words, at any specified time, the front will move an equal distance in *x* and *y* directions, which is expected for an isotropic system. For anisotropic systems, we can derive an equivalent correlation as an asymptotic limit. Note that when $\chi \to \infty$, $erf(\chi) \approx 1 - \frac{e^{-\chi^2}}{\sqrt{\pi}\chi}$. Using this asymptotic limit of the error function, we see that when η_1 is sufficiently large, the left hand side of Equation B.31 approaches the limiting value of $\sqrt{\pi}\eta_1$. Similarly, the right hand side asymptotically reaches the value of $\sqrt{\pi/a}\eta_2$. It is then easy to see that, at large times, a simple relationship exists between η_1 and η_2, which is

$$\eta_1 \approx \frac{\eta_2}{\sqrt{a}} \tag{B.32}$$

Equation B.32 states that the ratio of the front location at any large time τ in the *x* direction to that in the *y* direction is inversely proportional to $\sqrt{a}$. In other words, if $a < 1$ (i.e., permeability in the *x* direction is larger than that in the y-direction), the front will move longer (by a factor $1/\sqrt{a}$) in the *x* direction compared to the y direction.

While Equations B.31 and B.32 give the ratio of the two locations, we need another condition to determine them uniquely. This condition can be generated from the overall mass balance of the injected phase. Denoting *M* as the total mass of CO_2 injected during the time period 0–*t*, we can write

$$\int_0^{\delta_y}\int_0^{\delta_x} \phi\rho_g h dx dy = \frac{M}{4} \tag{B.33}$$

The factor of $\frac{1}{4}$ in Equation B.33 is necessary because we are considering only the first quadrant of the entire model domain for symmetry reasons. If an uniform injection rate is specified (which is not a necessary condition but we will apply it to make the mathematical derivation simpler), we can write Equation B.33 as

$$\int_0^{\delta_2}\int_0^{\delta_1} \phi\rho_g h dx dy = \frac{\dot{m}t}{4} \tag{B.34}$$

where $\dot{m}$ is the injection rate. In terms of dimensionless variables, Equation B.34 becomes

$$\int_0^{\delta_{D2}}\int_0^{\delta_{D1}} R d\xi_1 d\xi_2 = \frac{\dot{m}_D \tau}{4} \tag{B.35}$$

where $\dot{m}_D = \dfrac{\dot{m}}{H^2\rho_g\left[\dfrac{k_x}{\mu_w}\Delta\rho g\right]}$ is the dimensionless injection rate. After some algebraic manipulations, we obtain

$$\int_0^{\delta_{D2}}\left[\frac{\partial R}{\partial\xi_1}\Big|_{\xi_1=\delta_{D1}} - \frac{\partial R}{\partial\xi_1}\Big|_{\xi_1=0}\right]d\xi_2 + \int_0^{\delta_{D1}}\left[\frac{\partial R}{\partial\xi_2}\Big|_{\xi_2=\delta_{D2}} - \frac{\partial R}{\partial\xi_2}\Big|_{\xi_2=0}\right]d\xi_1 = \frac{\dot{m}_D}{4} \tag{B.36}$$

After evaluating the specified derivatives (using Equation B.28), and then performing the required integrations, Equation B.36 finally produces the following relationship between the dimensionless injection rate, and the transient front locations in the *x* and *y* directions:

$$erf(\eta_1)erf(\eta_2/\sqrt{a}) = \left[\frac{2\sqrt{a}}{a+1}\right]\left(\frac{\dot{m}_D}{\pi}\right) \tag{B.37}$$

Note that, if the system is isotropic with $a = 1$, the term within the [] on the right hand side of Equation B.37 becomes unity, and η_1 becomes equal to η_2 (from Equation B.31), which then leads us to a simple expression for η_1, i.e.,

$$erf(\eta_1) = \sqrt{\frac{\dot{m}_D}{\pi}} \tag{B.38}$$

From Equation B.38, it is easy to calculate the transient front location by using an inverse error function routine such as *erfinv* in MATLAB. For anisotropic systems, the two nonlinear algebraic equations given in Equations B.31 and B.37 need to be solved simultaneously, in which also we can use the *erfinv* routine from MATLAB.

Appendix C – Thermodynamic and Kinetic Data

Thermodynamic Data

The thermodynamic database compiled by Reed and Palandri (2006) (soltherm.h06) was used in this study. This database relies on Gibbs free energy data primarily from Holland and Powell (1998) for minerals, and from SUPCRT92 (Johnson et al., 1992) for aqueous species. For this study, these data were updated using the data of Bénézeth et al. (2007) for dawsonite.

Kinetic Data

A general rate law derived from transistion state theory (Lasaga et al., 1994) is used for mineral dissolution and precipitation:

$$R_m = \pm A_m k_m (\Omega_m^n - 1)^p \tag{C.1}$$

where R_m is the effective reaction rate, k_m is the rate constant (moles per unit mineral surface area and unit time), A_m is the specific reactive surface area per kg H_2O, Ω_m is the kinetic mineral saturation ratio (Q/K), and exponents n and p are either determined from experiments or taken equal to one. The value of the kinetic rate constant (k_m) can vary with the activity of other species, such as with pH (Lasaga et al., 1994; Palandri and Kharaka, 2004) as follows:

$$k = k_{25}^{nu} \exp\left[\frac{-E_a^{nu}}{R}\left(\frac{1}{T} - \frac{1}{298.15}\right)\right] + k_{25}^{H} \exp\left[\frac{-E_a^{H}}{R}\left(\frac{1}{T} - \frac{1}{298.15}\right)\right] a_{H^+}^{n_H} + k_{25}^{OH} \exp\left[\frac{-E_a^{OH}}{R}\left(\frac{1}{T} - \frac{1}{298.15}\right)\right] a_{H^+}^{n_{OH}} \tag{C.2}$$

where superscripts or subscripts *nu*, *H*, and *OH* indicate neutral, acid and base mechanisms, respectively; a is the activity of the species (in this case H+); n_H and n_{OH} are power terms (constant); and E_a is the activation energy for each mechanism.

These kinetic rate parameters were taken primarily from the compilation of Palandri and Kharaka (2004) and updated with data from Yang and Steefel (2008) for kaolinite, Hellevang et al. (2010) for dawsonite, and Golubev et al. (2009) and Duckworth and Martin (2004) for siderite (and applying the same data to ankerite), as shown in Table C.1. Rates were assumed reversible, except for quartz which was only allowed to dissolve because of its well-known slow precipitation kinetics at temperatures below about 200°C. Chalcedony was included as a potential silica precipitation phase, using the rate law and data of Carroll et al. (1998) for amorphous silica. Kinetic data for jarosite were taken from Madden et al. (2012), and the same data were assumed for alunite. Anhydrite was assumed to react at equilibrium because of its known fast dissolution and precipitation.

Table C.1. Kinetic parameters for Equation C.2, for k values in mol m^{-2} s^{-1} and Ea values in kJ mol^{-1}. See text for data sources.

Mineral	$\log(k_H)$ (acid)	Ea_H (acid)	n_H	$\log k_{nu}$ (neut.)	Ea_{nu} (neut.)	$\log(k_{OH})$ (base)	Ea_{OH} (base)	n_{OH} (base)	$\log(k_{CO3})$ (carb.)	Ea_{CO3} (carb)	n_{CO3}
Quartz				-13.34	90.1						
K-feldspar	-10.06	51.7	0.5	-12.41	38	-21.2	94.1	-0.823			
Plagioclase	-9.67	65	0.457	-11.84					(Data for oligoclase)		
Calcite	-0.3	14.4	1	-5.81	23.5				-3.48	35.4	1
Dolomite	-3.19	36.1	0.5	-7.53	52.2				-5.11	34.8	0.5
Strontianite	Use calcite										
Pyrite	-7.52	56.9	-0.5	-4.55	56.9						
			n_{Fe+3} 0.5		n_{O2} 0.5						
Hematite	-9.39	66.2	1	-14.6	66.2						
Kaolinite*	-11.10	65.9	0.777		-12.97	-16.84	17.9	-0.472			
Anhydrite				-3.19	14.3						
Ankerite	Use siderite										
Jarosite	-6.487	79	0.899	0.0		-10.964	79	-0.392			
Alunite	Use jarosite										
Illite	-10.98	23.6	0.34	-12.78	35	-16.52	58.9	-0.4	(Data for smectite)		
Muscovite	-11.85	22	0.37	-13.55	22	-14.55	22	-0.22			
Magnesite	-6.38	14.4	1	-9.34	23.5	-5.22	62.8	1			
Siderite	-3.75	48	0.75	-8.65	48						
Dawsonite	-4.48	49.43	0.982	-8.66	63.82						

* Re-fitted data; use with n = 0.333 in Equation C.2